Design of an Optical Interferometer Spacecraft

by

Andrew Marc Nisbet

S.B., Massachusetts Institute of Technology (1990)

SUBMITTED TO THE DEPARTMENT OF
AERONAUTICS AND ASTRONAUTICS IN PARTIAL
FULFILLMENT OF THE REQUIREMENTS
FOR THE DEGREE OF

MASTER OF SCIENCE
in Aeronautics and Astronautics

at the

MASSACHUSETTS INSTITUTE OF TECHNOLOGY

June 1992

Signature of Author _____
Department of Aeronautics and Astronautics
May 8, 1992

Certified by _____
Professor Joseph F Shea
Thesis Supervisor, Department of Aeronautics and Astronautics

Accepted by _____
Professor Harold Y. Wachman
Chairman, Department Graduate Committee

Design of an Optical Interferometer Spacecraft

by

Andrew Marc Nisbet

Submitted to the Department of Aeronautics and Astronautics
on May 8, 1992 in partial fulfillment of the requirements for the
degree of Master of Science in Aeronautics and Astronautics

ABSTRACT

The impact of extremely stringent structural control requirements on the overall design of a spacecraft system is investigated. A space-based optical interferometer presents a design case that necessitates the application of controlled structures technology. In order for interferometry to succeed, differential pathlengths between optical components need to be identical within a fraction of the wavelength of the light (~25 nm for visible light). This high level of precision must be maintained on a large, flexible structure in the face of common spacecraft vibrational disturbances. The typical aspects of spacecraft design are examined in an effort to determine what impact structural control has on subsystem sizing and how component selection decisions can minimize the disturbance environment. Topics addressed include orbital design, deployment analysis, and payload configuration as well as the attitude control, command and data handling, communications, power, propulsion, thermal control, and structural control subsystems. The results are that structural control objectives place significant demands on attitude control, thermal control, and computer processing requirements, and that numerous component choices can be made which completely eliminate some disturbance sources at a moderate cost, usually in terms of mass.

Thesis Supervisor: Dr. Joseph F. Shea
Title: Adjunct Professor of Aeronautics and Astronautics

Acknowledgments

First, I would like to thank my family who have been supportive throughout this long process. Though they may not understand the details and work involved in spacecraft design, Mom, Dad, and Mike have frequently lent sympathetic ears to the plight of a graduate student in "thesis mode."

To Meg, who has always been there to listen and to restore my sanity. Too many times, she had to put up with just the telephone when more was really needed. She probably never wants to hear the word "thesis" again in her life.

To Mike, who knows what it is like, and though he may not realize it, has frequently forced me to banish my laziness and motivated me by his example to finish off my work.

Finally, to SERC and those associated with it; especially my thesis supervisor, Professor Joe Shea, who focused me on what was really important and forced me to "say what I mean" rather than what I had written. I am grateful to have learned systems engineering from one of the pioneers in the field. Also to Professor Edward Crawley, who supported my research and gave me the opportunity to learn design in the academic environment. To the Interferometer Group, I wish lots of luck in subduing the "intermonster." Finally, I would like to thank my office mates, Larry, Jim, and Valeri, who repeatedly provided diversions with great discussions of US and Russian politics, philosophy, and the greater realities of life.

Contents

List of Figures

List of Tables

Chapter 1
Introduction

Systems engineering is a subject which seeks the successful integration of a large, complex set of components to accomplish an intended task. Space systems engineering and design is thus an inherently complex and interdisciplinary field. It requires the systems engineer to have an understanding of the fundamentals of each of the basic disciplines related to spacecraft construction: orbital mechanics, propulsion, thermal, power, structures, guidance and control, communications, data systems, and payload systems. The technical goal of the systems engineer in spacecraft design is to examine the mission objectives and translate them into a set of requirements or constraints at the subsystem level. Trade-offs must then be conducted to establish the interrelationships of the various subsystems and to determine the best design choices for each. The systems engineer must have a firm grasp of the different disciplines involved in order to communicate effectively with the subsystem engineers and to make rational design decisions.

Several good texts have recently been published that deal with space vehicle system design [1,13,39]. Each of these is fairly thorough in treating the subject, particularly from the standpoint of covering the fundamentals of each subsystem. They provide a valuable guide to the scope of the system design task and the tools used in the systems analysis. Typically, the systems engineer gathers and interprets information from the subsystem engineers rather than generating it himself, but he still needs to understand the disciplines in order to draw the correct conclusions. Systems engineering has generally been introduced only as a senior level course in general aerospace engineering curriculums. Real systems engineering and design education has typically occurred only with experience in industry or at NASA centers. The primary intent of this thesis is to provide an exercise in conceptual spacecraft design in order to gain experience in system trades and subsystem definition. The thesis is also intended to shed light on the system design issues inherent in the technology being researched at the M.I.T. Space Engineering Research Center (SERC).

M.I.T. SERC was established to conduct research in controls-structures interaction (CSI). As an initial phase in the effort, the center looked for a valid scientific mission that

would drive the technology goals for CSI development. A space-based optical interferometer proved to have the most stringent requirements for the CSI program and has since become a main focus of the research in SERC. A scale model of an interferometer structure, including the essential elements for the interferometry science, has been constructed in the lab to provide a common testbed on which to try out and evaluate competing CSI techniques and methodologies. The SERC Interferometer also provides a relevant example for a vehicle design project. A system design of the interferometer can give valuable insight on the unique systems impacts of a CSI-intensive spacecraft. The remainder of this chapter gives a tutorial on interferometry, including its motivation and unique requirements, and introduces the SERC Interferometer Testbed created to address these requirements.

1.1 Tutorial on Interferometry

Interferometry is the branch of physics that deals with the interference of light waves. The specific application referred to throughout this thesis is the use of interferometry to synthesize large telescope apertures from small discrete telescopes. The primary driver of a telescope's performance is the size (diameter) of its aperture. This parameter drives both the sensitivity of the instrument through the amount of light it is able to collect and the resolution, which varies directly with the diameter. The largest earth-based telescopes (in the visible part of the electromagnetic spectrum) are on the order of four meters in diameter. Earth-based performance is limited, however, by turbulence in the atmosphere. The solution to this has been to place telescopes in orbit above the atmosphere, such as the Hubble Space Telescope (HST). Unfortunately, launch vehicle and cost constraints will probably restrict space-based filled apertures to less than five meters diameter for the foreseeable future. Interferometry provides a feasible and economical way of achieving the dramatic improvements in resolution desired by astronomers. By using two or more small telescopes of modest diameter, interferometry permits the scientists to achieve the same resolution as a filled aperture of diameter equal to the maximum distance between the discrete telescopes. Interferometers of this type can be used in two different ways. "Imaging" uses the instrument to produce high resolution images of targets of interest, and "astrometry" uses it to make very precise measurements of the positions of celestial objects. Both of these techniques promise great rewards to the astronomical community.

A schematic of a two-dimensional interferometer is shown in Figure 1-1 to assist in describing the operating principles of the instrument. This section is intended to be primarily descriptive, so that the reader can gain a basic understanding of the science and of

its implications. More detailed and rigorous discussions and derivations can be found in [6,16]. Light comes to the instrument from a star and is captured by the collecting optics (A and B). Each light path is then passed through the steering optics, and possibly a delay line, to the combining optics, where it is interfered with its counterpart from the other telescope and forms an interference pattern on the detector. In order to produce a meaningful pattern, the total pathlength taken by the light from the star, through each set of optics, to the detector must be identical to within a fraction of the wavelength of the light. If the star is off-center of the instrument's line of sight by an angle θ, a differential pathlength error of $D \cdot \sin\theta$ will result. This gross error is compensated by the delay line.

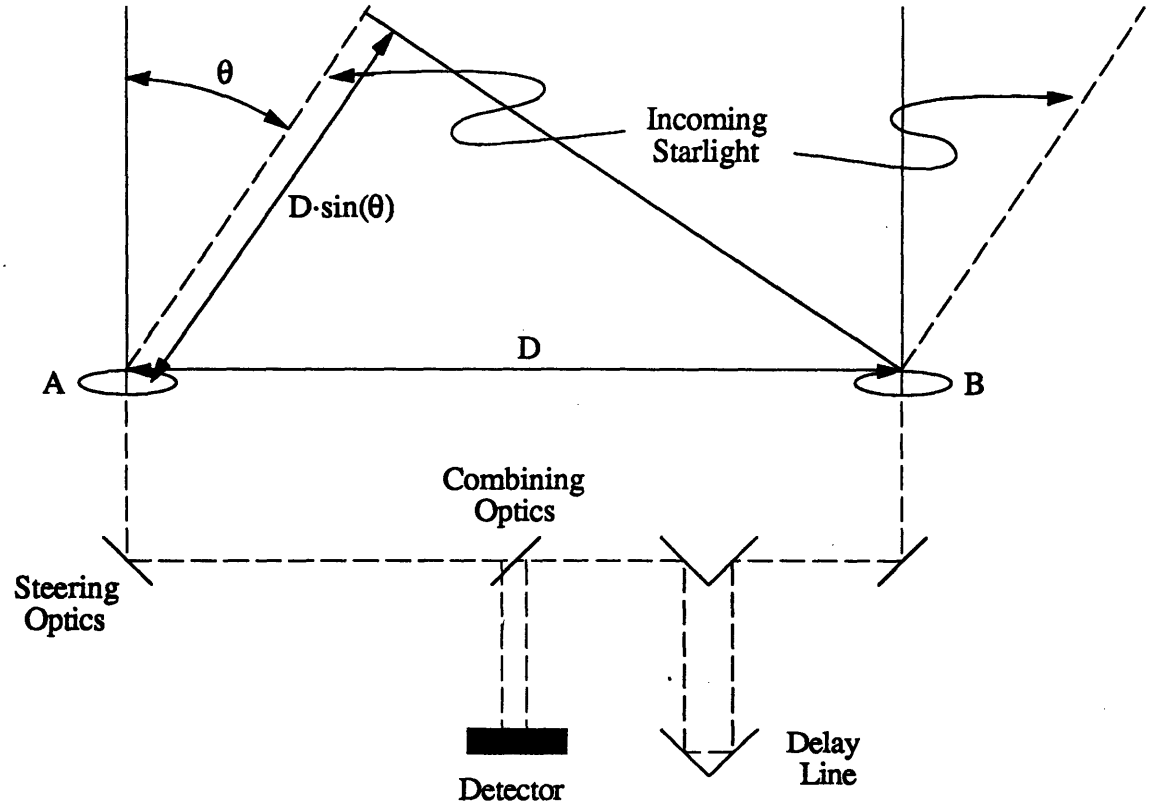

Figure 1-1 Schematic of a Two-Dimensional Interferometer

The interference pattern produced on the detector in a three-dimensional interferometer is a spatial Fourier transform of the true image, hence the image can be recovered by taking the inverse transform. Each data point in the Fourier (U-V) plane corresponds to a unique baseline of the instrument, with 180° symmetry about the line of sight. Each baseline of the instrument is defined by both its angle in the U-V plane and its length, D. The amount of the U-V plane covered by each data point is equal to the fill

fraction of the discrete telescope with respect to the full, synthesized aperture. Complete coverage of the Fourier plane, while perhaps desirable, is not necessary to obtain valuable information about the true image. Imaging and astrometry are further differentiated by the amount of data required for each target. Imaging seeks to fill as much of the U-V plane as possible to permit a reliable inverse transform, while astrometry requires only a single data point in the Fourier domain since it needs only information about the interference fringe as opposed to the transform.

The previously mentioned restriction on the allowable differential pathlength error is necessary to provide reliable fringe intensity (magnitude) information. To retain 99% of the image quality, a maximum root-mean-square differential pathlength error of $\lambda/20$ is required, where λ is the wavelength of the light. At the center of the visible spectrum, the wavelength is about 0.5 μm, yielding a tolerable error of only 25 nm RMS. This extremely tight tolerance in the pathlength error is the primary technological challenge of interferometry for CSI research. A normally operating spacecraft has numerous sources of mechanical vibration that are highly significant at the level of 25 nm and are transmitted to the optical instruments through the structure. This defines the need for applying CSI techniques such as damping, isolation, and even active control to minimize the differential pathlength error. At the system design level there are a number of choices that can be made to minimize or even eliminate some of the sources of vibrational disturbance. A primary focus of this thesis is to highlight the impact of CSI goals in making design decisions for a spacecraft. The SERC Interferometer provides a vehicle for investigating these issues.

1.2 The SERC Interferometer Testbed

The interferometer testbed is intended to represent a realistic scale model of a possible spacecraft, and it has provided a starting point for the design presented in this thesis. As shown in Figure 1-2, the SERC Interferometer is a 3.5 m tetrahedral truss structure with components representing the important elements of the problem. There are mock telescope locations at points A, B, and C on the science plane face, and a laser metrology system mounted at the fourth vertex, F. The metrology system is necessary to provide a precise measurement of the differential pathlength between the telescope locations and the fourth vertex, where the combining optics are assumed to be. A proof-mass actuator is positioned at the top vertex, G, to represent an actual spacecraft disturbance source. Finally, the entire structure is suspended from the ceiling by soft-spring mounts.

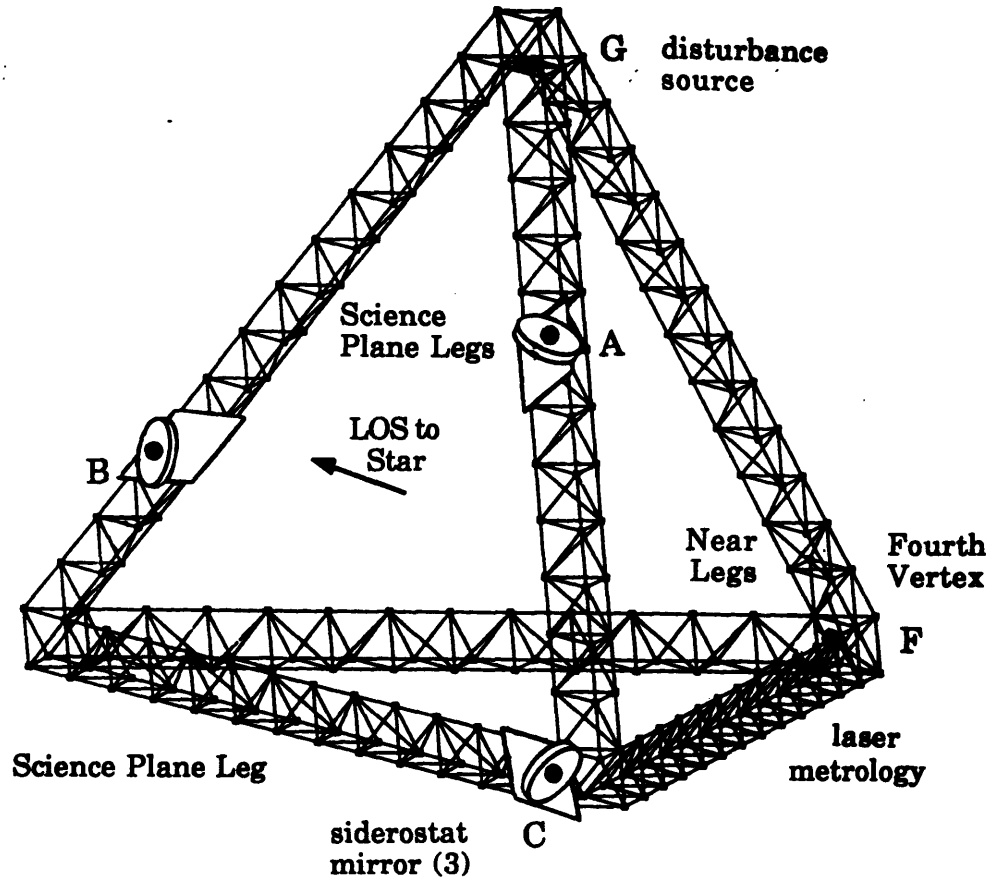

Figure 1-2 The SERC Interferometer Testbed

A significant amount of thought went into the design of the structural configuration of the truss and the placement of the components on it. The tetrahedral shape was chosen because it is a closed architecture that is inherently rigid. It is also nominally iso-inertial, which in an actual spacecraft would minimize some of the environmental disturbance torques experienced on orbit. A tetrahedron also provides a natural reference point from which the metrology system can derive three-dimensional measurements. The combining optics, the metrology mount, and the disturbance source are located in the vertices, positions which represent the confluence of two vibration minimization objectives. First, the vertices are inherently inflexible positions on the structure. If one considers the modal superposition method of describing the flexible motion of the structure, then those locations with generally small modal amplitudes are the best choices for positioning sensitive or noisy components. Locations with small modal amplitude transmit the least amount of vibration to the remainder of the structure. By mounting noisy components and sensitive optics here, the effects of any mechanical disturbances are significantly reduced. The vertices are locations of symmetry where equipment can be mounted without destroying the iso-inertial properties of the tetrahedron. The three locations of the mock telescopes roughly represent

locations of maximum, medium, and minimum flexibility. This allows the simultaneous evaluation of different mounting locations on achieving the CSI goals.

1.3 Outline

The SERC Interferometer testbed provides the focus for the spacecraft design presented in this thesis. To maintain relevance to the SERC research effort, the structural configuration of the testbed truss is taken as the given configuration for the spacecraft structural design, subject to launch and deployment constraints. The following chapters cover the various phases of the spacecraft design task. Chapter 2 discusses the detailed mission requirements, and addresses the orbit selection, deployment, and payload configuration issues. It also summarizes the expected instrument performance for the chosen configuration. Chapter 3 covers the more detailed subsystem analysis. It discusses the trades and sizing involving the attitude control, command and data handling, communications, power, and propulsion subsystems. Chapter 4 addresses the thermal and structural control subsystems, more from a requirements analysis point of view than from a system trade focus. The intent of this chapter is to conduct analysis to unique needs of the interferometer in terms of thermal and structural control, and to estimate the components and size of the subsystems. Chapter 5 presents the conclusions of the thesis and highlights the main design features of the spacecraft. It also suggests possible avenues for further research.

Chapter 2

Mission Design and Instrument Performance

This chapter introduces the topic of space optical interferometry and summarizes the current state of the field in order to motivate the work of this thesis. From this context, the mission requirements and design starting point of the SERC Optical Interferometer Spacecraft are derived. With the above in mind, orbit, deployment, and instrument configuration analyses are performed to determine the top level design features of the spacecraft. Lastly, the expected instrument performance, in terms of both imaging and astrometry, is examined based on the initial design specifications.

2.1 Concepts in Space Optical Interferometry

In 1989, the National Research Council commissioned the Astronomy and Astrophysics Survey Committee to survey their field and report recommendations for new ground- and space-based programs for the decade of the 1990's. The report of this committee (the "Bahcall" report [4]) is widely adhered to by the astronomy and astrophysics community, and is taken as the definitive guide for US funding priorities in the field. The report recommended the start of an Astrometric Interferometry Mission (AIM) within this decade both to achieve a thousand-fold improvement in the accuracy of measuring stellar positions and to serve as a necessary technology step towards the development of more ambitious imaging interferometers. The report conveys a sense of excitement at the potential advances attainable only above the earth's atmosphere and only with the very great resolution of interferometric techniques. It is clear from the Bahcall report that space interferometry is a scientific priority supported by the astronomy community.

A more revealing look at the expected potential of optical space interferometry is found in the working papers of the panels appointed by the Astronomy and Astrophysics Survey Committee [27]. These panels were sub-groups appointed to investigate and advise on the priorities of their particular sections of the field. The expected gains from space

interferometry are separated into astrometric and imaging studies. Resolving the complex structure of binary star systems, galactic nuclei, and the disks of nearby stars are the primary goals for imaging. The desire to achieve at least one order of magnitude improvement in resolution over that of the Hubble Space Telescope (HST) requires that imaging interferometers must be on the order of 25 m or greater in length. The sheer physical size of these instruments implies that imaging satellites will not be flown in the near future. Astrometry will be the main technique for the near term because baselines of less than 5 m are sufficient to provide significant scientific advances. The main technology development required for astrometric interferometers is the construction of ultra-precise (~1 nanometer) laser measurement systems. With the successful development of this technology, astrometry should provide dramatic advances such as an order of magnitude improvement in measurement of the Hubble constant, determination of galactic structure, and probably the first methodical approach to possible detection of nearby planetary systems. To accomplish these goals, the interferometry group set out a fairly detailed plan for evolution of space-based capabilities:

> "We envision an orderly progression from small to large instruments... The recommended progression has three steps: (1) an astrometric mission; (2) a multi-aperture imager (30-100 m baseline); and (3) a major imaging facility with a synthesized aperture of at least one km."

The interferometry panel expounded upon the above classifications, detailing the second as:

> "(2) *During the 1990's we should develop the technology for an imaging interferometer that could be deployed in space early in the next decade.* This logical successor to HST should have a resolution about an order of magnitude greater than HST. Although considerable analysis is required before the architecture of such an instrument is established, we project that it will have a maximum baseline length of at least 30 and possibly as much as 100 m, and total collecting area comparable to HST. The aperture might consist of 20 or more individual segments, arranged in a configuration determined by a trade-off of resolution, sensitivity, time required to form an image, and other factors."

Though the configuration that is ultimately chosen uses less than half the suggested 20 discrete apertures, the physical dimensions and characteristics of the SERC Interferometer spacecraft suggest that it would fit best into this second category.

Over the course of the past decade, there have been a number of conceptual design projects that prompted the plans set forth in the Bahcall report. One of the earliest is the Coherent Optical System of Modular Imaging Collectors (COSMIC) [38]. The COSMIC concept was originally developed in the early 1980's at NASA's Marshall Space Flight Center, with later research conducted at the Smithsonian Astrophysical Observatory. It is an interferometer optimized for imaging low surface brightness objects that can tolerate relatively lower resolution, but require better frequency sampling and greater collecting area. COSMIC envisions using one to four 18 x 4 m modules arranged in a cross-like pattern with three or four 1.8 m diameter telescopes each, and a mass of over 10,000 kg each. While it has sufficient density in baseline lengths to give good spatial frequency resolution, additional baseline angles would be achieved by rotation about the line of sight. COSMIC provides a total collecting area of up to 40.7 m^2 and resolution of one m-arcsec (about 9 and 15 times that of HST respectively) at a total mass of about 41,000 kg. The modules are sized for deployment and mating by the Space Shuttle.

A second project conceived in the early 1980's is POINTS (Precision Optical INTerferometry in Space) [28]. It consists of two U-shaped interferometers of two telescopes each using modest apertures of only 25 cm. The interferometers are mounted on a rotating joint such that they can achieve an angular separation of up to 180° between the line of sight vectors. The instrument is optimized for conducting astrometry down to an accuracy of about 5 μ-arcsec, but no provision would be made for imaging. POINTS will weigh approximately 1300 kg and would probably use an advanced Atlas launch vehicle to place it in an orbit of about 100,000 km altitude [31].

A third concept under consideration is the Optical Space Interferometer (OSI) which had its origin as a focus mission for the efforts of the controls-structures interaction (CSI) research group at the Jet Propulsion Laboratory (JPL) [20,23]. OSI is a Michelson interferometer of approximately 20 m baseline with seven 40 cm diameter apertures arranged along the top of a T-shaped truss structure. A fourth truss member extends perpendicularly from the T to support a three-dimensional reference point for a laser metrology system. OSI is something of a hybrid of COSMIC and POINTS in that it is designed to accomplish both the astrometry and imaging missions. OSI is expected to perform astrometry at the 10 μ-arcsec level, and to provide 5 m-arcsec resolution imaging. Sufficient spatial sampling would be achieved by both rotation about the line of sight and by tilting with respect to the line of sight. OSI would weigh about 3500 kg and could be launched on an advanced Atlas.

The three programs described above demonstrate the extent of varying approaches to space interferometry, and they also set a valid context for initiating the SERC

Interferometer design. As discussed in Chapter 1, this work is intended as both an exercise in spacecraft design and as a means of investigating the particular needs and system design choices associated with this type of spacecraft. The SERC Interferometer configuration is a scaled up version of the SERC testbed with a maximum baseline of 35 m. It would function similar to OSI in that it will be capable of both imaging and astrometry, however the primary focus will be on imaging. With this large baseline length and a primary mission of imaging, the SERC Interferometer is responsive to the second category described in the Astronomy and Astrophysics Interferometry Panel report. Thus, it should be realized that this design actually fits the specifications of a second generation instrument in terms of performance capability.

2.2 Mission Requirements

In order to start the design, the top-level mission requirements need to be defined. The mission requirements must be set to meet the needs specified by the user community, and they should help to limit the scope of the design. For the interferometer, the mission requirements are essentially a set of quantifiable guidelines about the expected scientific performance of the instrument. Subject to these guidelines, the physics and technology involved in interferometry will dictate many of the important design features for the spacecraft.

The expectations of scientific performance can be extracted from the Bahcall report and its working papers. The main goals for an imaging optical interferometer are a resolving power of better than 5 m-arcsec over the visible range of light (0.3-1.0 μm) and the capability of observations at 20th magnitude. Choosing the center of the desired spectrum, SERC further refined the resolution requirement to be 3 m-arcsec at 0.5 μm wavelength. The diffraction limited resolution, ρ, of an optical instrument is a direct function of its physical size as described by:

$$\rho \cong \frac{\lambda}{L} \qquad \text{Eq. 2-1}$$

where L is the maximum baseline length of the instrument. Note that this equation is exact within a factor of two depending on the shape of the aperture. For a resolution of 3 m-arcsec at 0.5 μm wavelength, a maximum baseline length of 35 m is required; hence, the dimensions of the SERC Interferometer.

The magnitude requirement is linked directly to the dimension of the collecting optics, the integration time, the pixel size of the target, and the required signal level in the detectors. All of these parameters are linked by the following two equations [34]:

$$N_{ph} = (1.273 \times 10^{9}) \cdot A_{apt} \cdot T_{int} \cdot 10^{-0.4m} \qquad \text{Eq. 2-2}$$

$$SNR = \frac{\sqrt{N_{ph}}}{\left(\frac{L}{D}\right)^2} \approx \frac{\sqrt{N_{ph}}}{\#_{pixels}} \qquad \text{Eq. 2-3}$$

where N_{ph} = number of photons
A_{apt} = area of collecting optics
T_{int} = integration time
m = stellar relative magnitude
SNR = signal-to-noise ratio in detector
L = baseline length
D = diameter of collecting optics
$\#_{pixels}$ = image size on detector

The aperture size may be further constrained by specifying a collecting area "comparable to that of Hubble," although this is really a guideline and not a requirement. The number of pixels is generally set by the target of observation, and reasonable signal-to-noise ratios would be in the range of five to ten. This leaves a relatively narrow range for the design parameters of integration time and aperture area.

In addition to magnitude and resolution specifications, parameters that reflect the speed and quality of the imaging process need to be defined. Clearly, it would be unacceptable to have an instrument that could successfully image targets as dim as 30th magnitude but required several days to accomplish the feat. A reasonable time for imaging would be comparable to what is achievable with ground telescopes. These are generally scheduled such that all necessary data can be taken in one night. Based on this schedule, the imaging rate for the interferometer is set at greater than one image per day. Note that this will exceed the output of ground-based instruments since it is not restricted by daylight or by weather. One image per day would be the minimum rate assuming the target is 20th magnitude, but since most objects will be considerably brighter than this, the interferometer will usually require less time. The quality of the imaging can be expressed by the amount of U-V coverage in the Fourier plane. Each point in the Fourier plane corresponds to a discrete baseline length and angle, with symmetry over 180 degrees. U-V coverage, then, defines the spatial frequency coverage of the interferometer. Very-long-baseline radio interferometry routinely extracts significant scientific data with Fourier coverage on the order of only one percent. It is generally expected that an optical imager will achieve coverage of at least 50%. Full coverage of the aperture is desirable, but not required. In order to facilitate the comparison of different instrument configurations, the requirement for

minimum coverage is set at 65%, which corresponds to the coverage achievable with eight telescopes (the maximum number as constrained by launch mass) in a single rotation through the U-V plane.

To examine alternative payload configurations, it is also necessary to define a baseline target such that the performance of each configuration can be determined and compared. The measure of this performance will be traded off against such cost parameters as mass and power to determine the best arrangement. A typical target for an imaging interferometer would be a galactic core. An object of this type fills about 45 pixels on the detector, and is about 15^{th} magnitude. A magnitude of 15 is quite acceptable, rather than the limit of 20, since it is desired to analyze the average performance as opposed to the limiting performance. To get useful information from the instrument, a signal-to-noise ratio of at least 5 will be required. These three parameters (pixel size, magnitude, and SNR) are sufficient to derive the performance parameters of the instrument given the number, size, and relative positions of telescopes used.

Although astrometry is not the primary mission of this instrument, its performance in this category is of interest. The Bahcall report calls for astrometric precision of 3 to 30 μ-arcsec to a stellar magnitude of 20. Astrometric accuracy is a function of the wavelength, the number of photons collected, and the instrument geometric parameters as defined by [32]:

$$\text{accuracy} = \frac{\lambda}{2\pi LD\sqrt{N_{ph}}} \qquad \text{Eq. 2-4}$$

Equations 2-2 through 2-4 will be used extensively in the following sections to assist in trading off different telescope arrangements, and to determine the performance of the final instrument configuration.

The last mission requirements that must be specified are guidelines for the program launch and duration. In order to limit costs, which have the potential to grow tremendously for a spacecraft of this size and function, the program is limited to a single launch. In addition, it would be valuable to prohibit the use of manned-assembly. This restriction opens a much broader range of possible orbits, but also requires that the spacecraft go through a relatively complex deployment. This process will be detailed in the next section. It would be logical to specify a mission duration that is comparable with the current and planned great observatories. This leads to a minimum spacecraft lifetime of 10 years at full capability, with perhaps partial capability extending beyond that time frame. With these last

two guidelines set, the specification of the SERC Interferometer mission requirements is completed as summarized in Table 2-1 below.

Table 2-1. SERC Interferometer Mission Requirements and Baseline Imaging Parameters

Mission Lifetime	10 years
Program Constraint	Single launch
Imaging Resolution	3 m-arcsec @ 0.5 μm wavelength
Relative Stellar Magnitude	20
Imaging Rate	> 1 per day
Fourier (u,v) Coverage	> 65%
Astrometric Accuracy	3 - 30 μ-arcsec @ 20^{th} magnitude
Baseline Mission:	15^{th} magnitude target 45 pixel size SNR of 5

2.3 Deployment Analysis

The program constraint of a single launch proves to have a major impact on the design of the spacecraft. The structural characteristics become constrained not only by the existing configuration of the SERC testbed, but also by the payload volume that is available in current launch vehicles. The two largest launch vehicles in the US inventory are the Space Shuttle and the Titan IV. In addition to having the largest payload volume, these are the only two US launch vehicles with sufficient capacity to place the approximately 12,500 kg interferometer into orbit. The Titan IV has a slightly larger payload volume due to the cone section above the main fairing. Partly for this reason, but mainly for reasons of orbit selection as explained in section 2.4, the Titan IV is selected as the launch vehicle. This section will summarize the structural characteristics of the SERC Interferometer testbed and how they impact the spacecraft as the initial design configuration. The section then presents a possible deployment scheme that is compatible with the Titan IV payload fairing and investigates the implications of this scheme on the spacecraft design.

2.3.1 SERC Interferometer Testbed Design

Figure 2-1(a) is a drawing of the bare testbed truss structure. It does not show any of the suspension metrology, mock siderostat, or actuation hardware present on the actual testbed, but it does show the basic configuration of the trusswork that served as an initial design point for the spacecraft. Figure 2-1(b) shows a close-up of a truss-beam section and cross-section. Each regular strut in the truss (longerons and cross-members) are 25 cm long, with the diagonal battens at 35 cm. With 14 bays in each leg, each side of the tetrahedron is 3.5 m long; thus, the testbed truss is a tenth-scale model of the spacecraft. In the interests of maintaining some degree of commonality with the testbed, the spacecraft structure will maintain the basic size and proportions of the testbed truss, subject to launch and deployment constraints.

Some preliminary work on the design of an interferometer spacecraft of this configuration has already been completed [11]. This work provides us with further information for initial design assumptions, which will prove useful in orbital analysis and in determining the best telescope configuration. This design under-estimated the mass at 10,700 kg and over-estimated the power at 5000W.

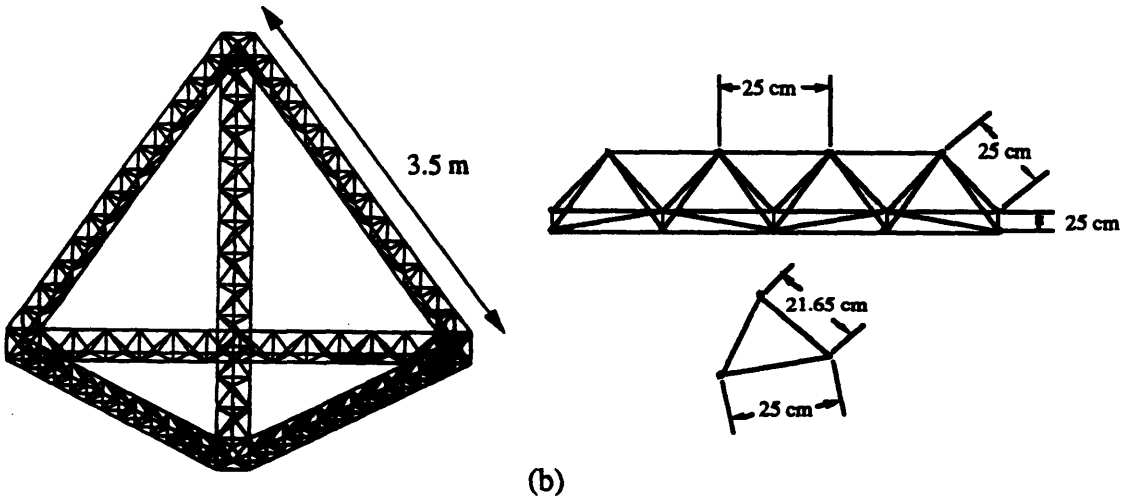

Figure 2-1 a) SERC Interferometer Testbed Bare Truss b) Truss Beam Section and Cross-Section.

2.3.2 Deployment Scheme

In designing a deployment scheme for the interferometer spacecraft, one is immediately confronted with the task of how to fit a 35 m tetrahedral truss structure into a standard

payload fairing. The Titan IV/NUS (No-Upper-Stage) payload fairing is a cylinder of 18.8 m length by 5.0 m diameter. There is an additional 1.3 m length in the interface region where the fairing meets the second stage, and an additional 3.5 m length in the 15° cone section at the top of the fairing. Truss structures have generally presented no problems in past deployments since they can collapse into very compact forms. The interferometer cannot take advantage of such schemes, however, since the interior of the truss beams contain extensive optical components. The main problem with this is that the total volume contained in the six truss beams is larger than the total volume in the Titan IV fairing. This demonstrates the need for collapsing at least part of the beams, and doing so in such a way as to not interfere with the optical train. There is also the need for breaking three of the legs and having them meet and join in the deployment process.

Figure 2-2 shows a stowed configuration that will meet the above constraints. The trapezoidal piece at the base of the fairing is the fourth vertex. The near legs (1-3) are attached to the fourth vertex by hinged joints and are constructed so as to double their length in a telescoping motion. The halves of the science plane legs (4-6, A & B), which contain the collecting optics, are attached to the near legs by a two-axis hinge at the top end. During launch, these legs would be attached to the near legs at several other points, and the near legs would be attached to each other at the top end to maintain rigidity. At deployment, these constraints would be released.

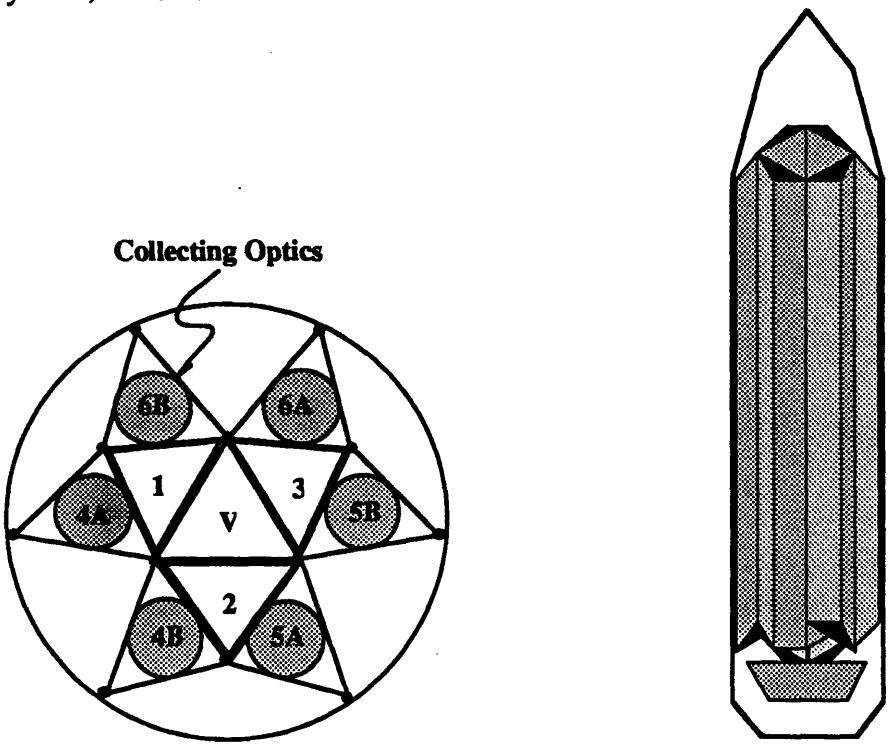

Figure 2-2 SERC Interferometer Stowed Configuration

Figure 2-3 (a-f) shows the deployment of the tetrahedron from this stowed configuration in a sequence of six positions. Throughout the sequence, the truss legs are shown as solid triangular beams rather than trusswork beams. In the transition from (a) to (b), the near legs open in an umbrella-like fashion about the fourth vertex, rotating about one hinged side until the free point contacts the fourth vertex and is locked into position. In the transition from (b) to (c), the near legs undergo a telescoping motion, doubling their length from 17.5 to 35 m. Note that this movement implies that the half of each near leg closest to the fourth vertex must be small enough to fit inside the cross-section of the outer portion of these legs. In going from (c) to (d), the A portion of the science plane legs have rotated about their two-axis joint until the adjacent point of the triangle meets the end of the near leg and locks into a single-axis rotation joint. Transforming from (d) to (e) entails a rotation of the A legs about the axis from the single- to the two-axis joint to their final position. In the last transition, from (e) to (f), the B portions of the science plane legs undergo the same process that the A legs just completed. To complete the deployment, the B legs must meet the A legs and lock into place. The actuators and mechanisms involved in this deployment scheme would necessarily be quite complex, however their detailed design and integration are not considered in this thesis.

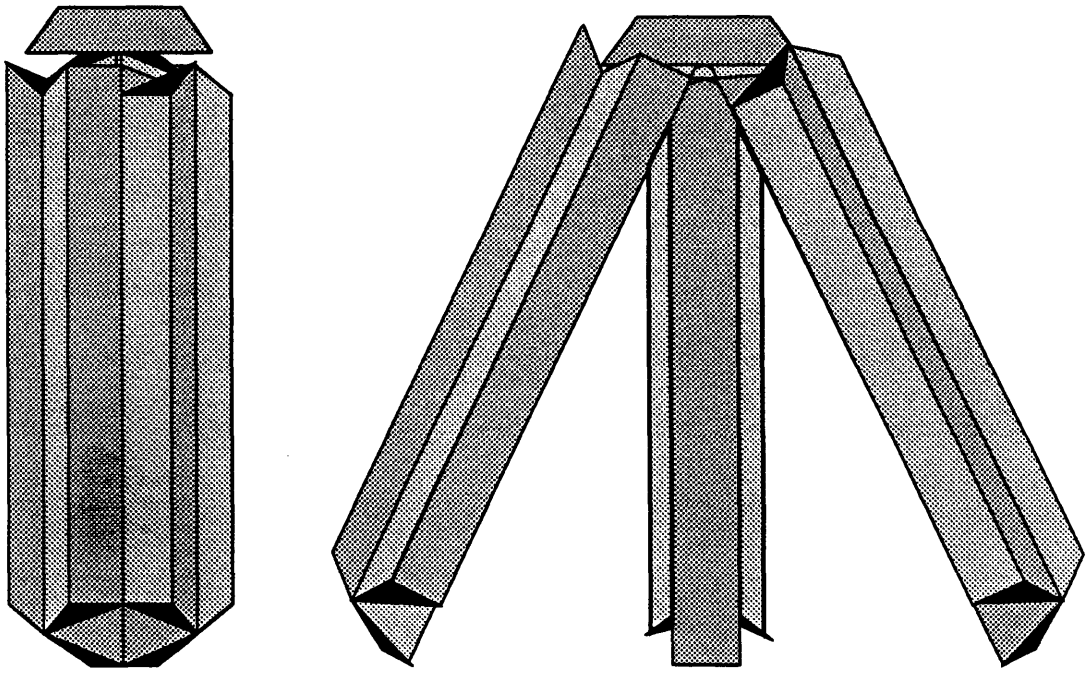

(a) (b)

Figure 2-3 (a-b) SERC Interferometer Deployment Sequence

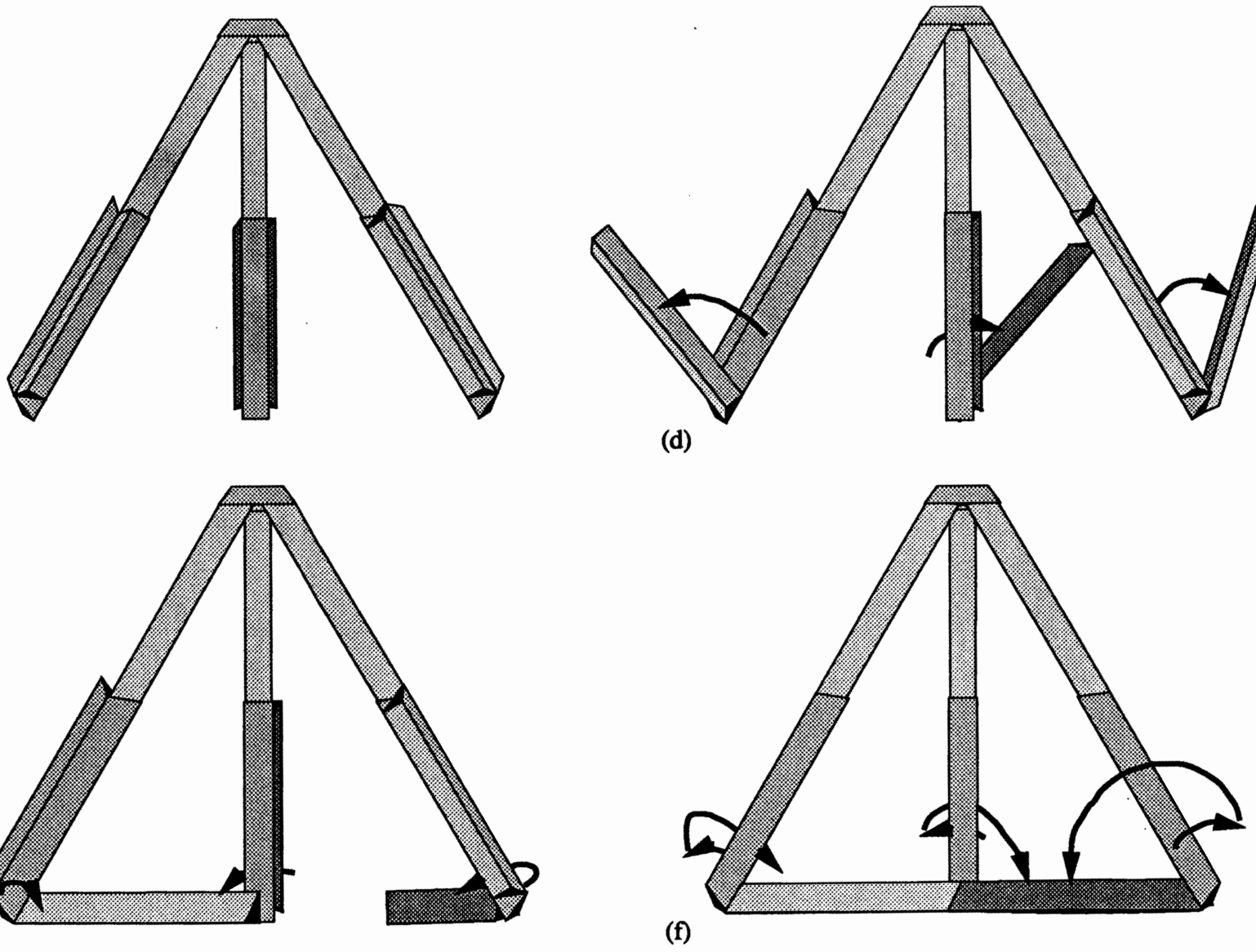

Figure 2-3 (c-f) SERC Interferometer Deployment Sequence

2.3.3 Implications of Deployment Scheme

Using the stowed configuration just shown requires some additional constraints on the structure. One of these is the previously mentioned need to telescope the near legs to half their deployed length in order to fit lengthwise in the payload fairing. The fairing diameter also applies a constraint, this time on the dimensions of the beam cross-section. If the testbed dimensions are simply scaled up by a factor of ten, the diameter of the stowed configuration is 7.7 m. This is significantly larger than any current or planned payload fairing, the largest of which is that for the Ariane V at 5.4 m. If the spacecraft is to be launched in a Titan IV, the size of the beam cross-section must be reduced by cutting the nominal strut length. The maximum strut length that can be used, assuming the same truss pattern, is 1.68 m. This would require a batten strut length of 2.38 m and a total of 21 bays to achieve a leg length of 35.3 m.

One obvious effect of reducing the cross-section of the truss-beam is a reduction in the stiffness of the structure. If one models the truss leg as a Bernoulli-Euler beam, the frequency of the structural modes varies as

$$\omega \propto \sqrt{\frac{EI}{mL^4}} \qquad \text{Eq. 2-5}$$

The only one of these parameters that changes with the reduced cross-section is the inertia, I, which varies as the square of the ratio of the strut lengths. Consequently, it can be determined that:

$$\frac{\omega_{2.5}}{\omega_{1.68}} = \frac{\ell_{2.5}}{\ell_{1.68}} = 1.49 \qquad \text{Eq. 2-6}$$

In other words, by reducing the nominal strut length from 2.5 m to 1.68 m, the stiffness of the structure should decrease by a factor of about 1.5.

The reduced cross-section has further implications as well. While the length of the legs remains approximately the same, the density of cross-members has increased, resulting in an increase in the structural mass of 478 kg. The last implication has to do with the optical components. With the chosen stowed configuration, it is not possible to mount the telescopes on the face of the science plane. Instead they will have to be mounted on the inside of the truss-beam. The strut length of 1.68 m then places a constraint of 79 cm on the maximum diameter of the collecting optics. With the 2.5 m length, this dimension would have been 117 cm. This results in a decrease of 54% in the collection area of the optics.

2.4 Orbital Analysis

Before any subsystem design work can occur the spacecraft orbit needs to be determined. The orbit has an impact on each of the subsystems, from sunlight effects on power and thermal design to gravitational effects on propulsion and attitude control. Because of the large mass of the spacecraft, it will obviously be limited to a low earth orbit (LEO). Equatorial low earth orbits have the benefit of permitting higher launch mass due to the rotational velocity of the earth, but they have a strong disadvantage due to an eclipse period during each orbit. For a 10 year mission with power requirements in the multi-kilowatt range, an eclipse during every orbit would require very large battery masses. Eclipses also cause repeated thermal transients in the structure, which complicates the structural design; thus it would be extremely valuable to eliminate eclipses through proper orbital selection.

The only way to avoid eclipses in LEO is to use a polar, sun-synchronous orbit along the terminator, a so-called "twilight" orbit. In a sun-synchronous orbit, the oblateness of the earth acts to precess the plane of the spacecraft orbit at a rate equal to the mean motion of the earth about the sun. The net effect is that by matching a particular inclination to the altitude, the spacecraft orbital plane maintains the same orientation with respect to the sun. If such an orbit is placed along the day-night line, the orbit should always be in sunlight.

Eclipse-free twilight orbits are actually somewhat more complex than just described. The reason for the additional complexity is the tilt of the earth's rotation axis with respect to the ecliptic plane. The effect of this tilt is that the sun appears to move through a $\pm 23.5°$ north-south drift over the course of the year, with the extremes occurring at the solstices. For orbits below 295 km altitude, eclipse periods will occur at both the winter and summer solstices, once per orbit [15]. Below 1333 km, eclipse periods will occur once per year at the summer solstice. The difference in solstice conditions occurs due to the fact that the orbit plane is tilted towards the sun over the north pole, leading to less severe eclipse conditions. The solution of this problem is to either place the spacecraft in an orbit above 1333 km altitude or to design the energy storage system to accommodate the eclipse season.

2.4.1 Orbital Limitations

It is fairly obvious that twilight orbits offer unique advantages for this type of spacecraft at the cost of somewhat reduced payload mass and somewhat higher radiation over the polar regions. The advantages of thermal stability throughout most, if not all, of the year

outweigh the disadvantages, so a twilight orbit is selected for the interferometer. The remaining choice is the altitude of the orbit. The altitude is limited by three factors: radiation effects, atmospheric drag, and lift capacity.

Radiation affects the spacecraft system in two ways. First, it degrades the effectiveness of solar arrays over time by altering the atomic structure of the semiconductor solar cells. Radiation degradation is a problem that must be addressed in the design of any spacecraft solar power system. Second, radiation damages all electronic components via the same mechanism that degrades solar cells. Radiation can cause single event upsets in digital electronic components by permanently altering voltages in semiconductor chips. For an interferometer, the primary concern is the effect on the CCD photodetectors, which are generally quite sensitive to radiation effects. Shielding can help mitigate radiation effects, but since radiation increases significantly with inclination and altitude, choice of the orbit has a dominant effect on the radiation environment. Reference [2] compares radiation environments of polar orbits at 900 and 1500 km altitude over five years at solar minimum. External proton (20 MeV) and electron (1 MeV) fluences increase by an order of magnitude from 900 to 1500 km altitude, and trapped proton peak flux increases by more than two orders of magnitude. Total radiation dose through 3 mm aluminum shielding is expected to be 10 Krads and 60 Krads respectively. Since the SERC Interferometer will be a 10 year mission, it will be exposed to the majority of the 11 year solar cycle. Consequently, the doses encountered can be expected to more than double. Radiation effects, therefore, strongly favor a lower altitude orbit.

Drag effects have the opposite influence of radiation by causing orbital decay and ultimately re-entry, which limits the mission lifetime. Since atmospheric drag increases with density, which decreases with altitude, lifetime can be increased by using a higher orbit. The lifetime of a satellite can be estimated by modelling the effects of the drag force on the orbital altitude. The acceleration due to drag can be approximated by

$$a_d = \frac{1}{2M_{s/c}} \rho C_D A v^2 \qquad \text{Eq. 2-7}$$

where $M_{S/C}$ is the spacecraft mass estimated of 11,700 kg, ρ is the density as a function of altitude as taken from the 1976 Standard Atmosphere [26], C_D is the coefficient of drag estimated at 2.2, S is the spacecraft cross-sectional area which varies from 126 m^2 to 253 m^2 depending on orientation , and v is the circular orbit velocity. The effect of this acceleration on the altitude can be estimated by using Hill's equations, which are commonly used for orbital rendezvous operations. The linearized equations are:

$$\frac{d^2x}{dt^2} - 3n^2x - 2n\frac{dy}{dt} = a_x \qquad \text{Eq. 2-8}$$

$$\frac{d^2y}{dt^2} + 2n\frac{dx}{dt} = a_y \qquad \text{Eq. 2-9}$$

where x is the radial direction from earth's center, y is tangential in the direction of the velocity vector, n is the mean motion of the orbit, and a_x and a_y are the acceleration terms. Using these equations to numerically solve for the change in x over a single orbit, one can plot the expected change in altitude as a function of altitude as shown in Figure 2-4. The two lines represent the extremes in cross-sectional area for the interferometer, and the discontinuity at 500 km altitude is due to separate curve fits of the atmospheric density data. The 1976 Standard Atmosphere, measured about halfway between a solar maximum and minimum, is a nominal atmospheric model; therefore, these calculations should give anaverage estimate of the orbital decay. Over a ten year mission, the interferometer will go through approximately 55,000 orbits. If a minimum altitude of 200 km is specified at end-of-life, and the average between 200 km and some initial altitude is used to estimate the

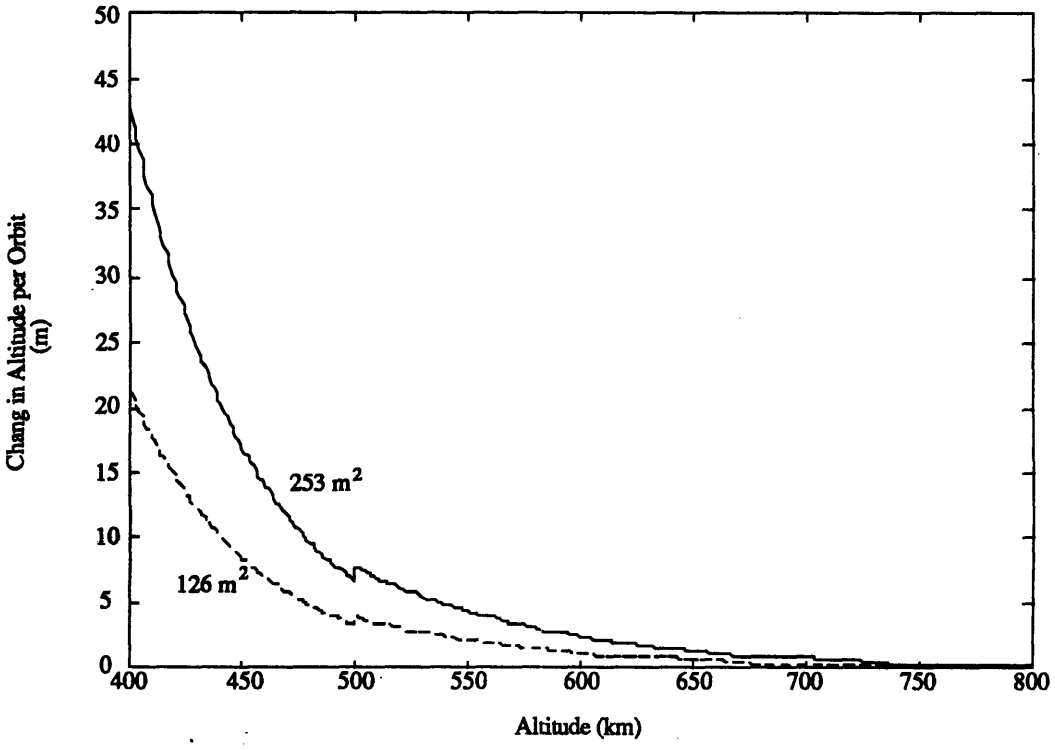

Figure 2-4 Estimated Change in Altitude Per Orbit Due to Drag as a Function of Altitude

average decay rate, one finds that the minimum initial altitude required is 650 km. This estimate of the average decay rate is fairly conservative, however the minimum cross-sectional area curve is used to offset the conservatism. Since the interferometer is inertially pointed, its cross-sectional area is constantly varying with respect to the velocity vector. As a final design margin, an initial altitude of 700 km is specified to ensure meeting the desired mission lifetime.

The last factor constraining the orbital altitude is probably the most important, the capacity of the launch vehicle. The Titan IV is capable of placing a payload mass of 11,700 kg (the interferometer estimated mass without its apogee kick motor) in a circular polar orbit of only 300 km altitude [37]. This is clearly insufficient given the previous lifetime constraint. In order to permit the Titan to place the interferometer directly into a 700 km circular orbit, the payload mass would have to be restricted to only 5000 kg, less than half the estimated mass. This, too, seems unacceptable. Another option, however, is possible, The Titan is capable of placing 12,500 kg into a 125 x 700 km elliptical orbit. To place the interferometer in the minimum altitude orbit, then, requires either an upper stage to perform a Hohmann transfer from 200 to 700 km, or an apogee kick motor to circularize the elliptical launch trajectory at 700 km. The details of this trade are discussed in the propulsion subsystem section of Chapter 3.

Considering the fact that both radiation and launch capacity strongly favor lower orbits, it seems most reasonable to select the 700 km minimum lifetime altitude. The only factor strongly favoring a higher orbit is the eclipse problem, which would require a minimum altitude of 1333 km. Besides the fact that switching to this altitude would entail about an order of magnitude increase in the radiation fluences, the Titan IV lift capacity precludes the use of an elliptical initial orbit. A Hohmann transfer would have to be used, requiring an increase of 433.2 m/s delta v over that required to circularize the 125 x 700 km orbit at 700 km. For these reasons an orbital altitude of 700 km is selected.

2.4.2 Eclipse Periods

As described in the first part of this section, choosing a twilight orbit altitude below 1333 km will result in eclipse periods during summer solstice. The extent of these eclipse periods can be found by solving for the limiting angle to the ecliptic in the following two equations [15]:

$$\dot{\Omega} = -\frac{3J_2R_e^2}{2}\sqrt{\frac{\mu}{a^7}}\cos i \qquad \text{Eq. 2-10}$$

$$\frac{R_e}{a} = \cos\left(\varepsilon \pm \delta + i - \frac{\pi}{2}\right) \qquad \text{Eq. 2-11}$$

Equation 2-10 is the sun-synchronous orbit condition that matches the inclination to the altitude when $\dot{\Omega} = 1.991 \times 10^{-7}$ rad /sec. $J_2 = 0.00108264$ is the second zonal harmonic of the earth's oblate spheroid. Equation 2-11 must be satisfied for the intersection of the orbit with the ray from the sun tangent to the earth. ε is the angle between the ecliptic and the equator, and $\delta = 0.2731$ degrees is the apparent radius of the sun's optical disk. Using $+\delta$ gives the penumbra condition, and $-\delta$ gives the umbra condition.

By setting the altitude and solving for the inclination in the first equation, one can then find the limiting ecliptic angle for eclipse. Using 700 km altitude gives a sun-synchronous inclination of 98.188°, a penumbra ecliptic angle of 17.25°, and an umbra angle of 17.8°. Figure 2-5 shows the variation of the ecliptic angle over the year together with the penumbra bound. The angle is greater than 17.25° for a total of 86 days centered on the summer solstice, or about 23.5% of the year. The average eclipse time per orbit during this period is 14.75 minutes, with a maximum eclipse duration of 18.78

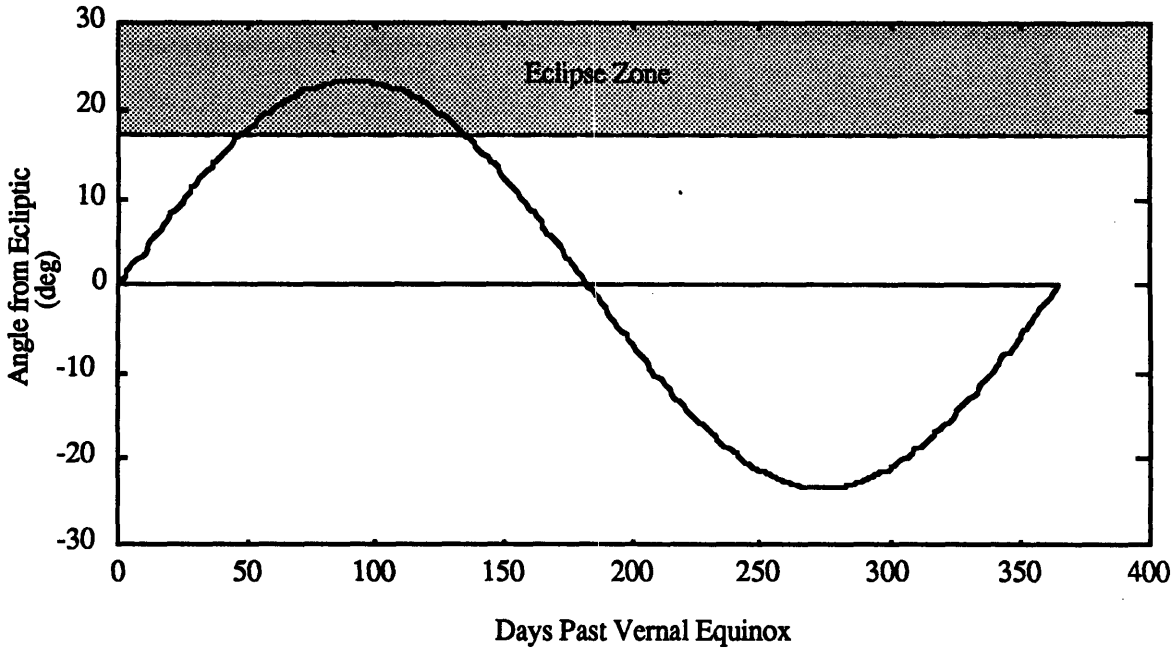

Figure 2-5 700 km Altitude Twilight Orbit Eclipse Zone

minutes. All important orbital information for the SERC Interferometer is summarized in Table 2-2.

Table 2-2 SERC Interferometer Orbital Information

Mission Lifetime	10 years
Orbit Type	polar, sun-synchronous
Altitude	700 km
Inclination	98.188°
Period	98.77 min
Eclipse Season	summer solstice (86 days)
Average Duration	14.75 min (14.9%)
Maximum Duration	18.78 min (19.0%)

2.5 Payload Configuration Analysis

Besides the deployment and orbital issues, the other top-level design choice that significantly impacts the design of the spacecraft subsystems is the size and configuration of the payload. So far, the only established specification is that the spacecraft is an interferometer with a primary mission of imaging. No decision has been made as to the number, type, and position of the telescopes. The type of telescope that is assumed for this design is a siderostat/beam-compressor combination. The siderostat is a large flat mirror that, via tip and tilt control, steers the light from the target into a Cassegrain beam compressor. The advantage of this arrangement over a beam compressor without siderostat is that one needs to control the steering of only the siderostat to very tight tolerances rather than the entire spacecraft. This allows for much less stringent pointing requirements for the attitude control system. The number and position of the siderostat/beam-compressor assemblies (hereafter called simply "siderostats") are left as free design parameters. The selection of these entails a trade of increasing performance in terms of time required for imaging, sensitivity, and percentage Fourier coverage against increasing cost in terms of mass and power. Also involved in this design trade is the choice of science operating mode. There are several methods of achieving sufficient Fourier coverage with varying numbers of siderostats. These entail combinations of rotation about the line of sight (LOS), tilting the spacecraft with respect to the LOS, and using trolley mounted siderostats that are free to translate along the face of the science plane truss legs. This section details the design trade and the resulting payload configuration.

2.5.1 Science Operating Modes

The science operating mode refers to the method by which different baseline lengths and angles are created in the process of imaging. As mentioned above, there are several different ways of generating sufficient coverage. Previous design work on this interferometer [11] assumed three siderostats mounted on trolleys that could translate the length of the truss leg. During the data taking mode, the spacecraft orientation would remain inertially fixed, and one pair of siderostats would be collecting data while the third translated to a new position. Delay lines for each siderostat would also have to translate to a new position to correct the total pathlength. By this method, a maximum of 83% of the Fourier plane could be covered in the space of approximately five hours. Although this method provides for a relatively simple attitude control problem, the translating siderostats introduce complexities. The motion of a siderostat produces mechanical vibrations that would interfere with the operation of the other pair, and it would require a laser metrology system that is capable of tracking the components as they move down the length of the beam. Having masses of about 168 kg (~1.4% of total mass) moving on the truss would require a more complex structural control scheme that would entail such techniques as gain scheduling.

A second option is that used by OSI. It uses a small number of fixed siderostats with non-redundant baseline lengths. Baseline angles are varied by rotating the entire spacecraft about the LOS, and additional lengths are attained by tilting the spacecraft with respect to the LOS. This method eliminates the vibration and metrology tracking problems involved in moving the siderostats, but still requires translation of the delay lines for each tilt angle. The benefit of this approach is the extreme flexibility of operations, meaning the amount of Fourier coverage and time for an image can be adjusted to suit the particular target by altering the number of tilt angles used. The largest problem with this method is the complex attitude control problem: the spacecraft must be rolled very precisely about any arbitrary axis, which implies more complex operations and interfacing.

The third option is to use a sufficient number of siderostats arranged in such a way as to give a large and even spread of baseline lengths. The baseline angles would be varied by rotation about the LOS, and with enough siderostats, the total Fourier coverage would meet the requirement. This method eliminates both siderostat and delay line motion as sources of vibration and as causes of more complex control schemes. The need for the metrology system to track the siderostats is also eliminated. The attitude control required for this option is relatively simple, needing precise roll control about only a single LOS axis. The main drawbacks to this approach are additional mass and power requirements

and a limit to the performance flexibility of the system. The coverage and imaging time cannot be tailored to the particular target.

Table 2-3 summarizes the advantages and disadvantages of each of the three approaches described above. Since the major technological challenge of an interferometer spacecraft is maintaining the baseline, differential pathlength, and wavefront tilt errors within very tight tolerances, a primary goal of the system design is to eliminate possible sources of mechanical vibration. In addition to significantly complicating the metrology system by requiring the tracking of moving targets, the science operating mode that uses translating siderostats deliberately adds a strong source of mechanical vibration. It is obvious that this method is contrary to the objectives of our system design, so it will not be considered in the remaining trade study. The other two modes will be addressed in the following study of the number of sets of collecting optics, with the rotation-only option being an extreme case of the tilt and rotate mode.

Table 2-3 Advantages and Disadvantages of Different Science Operating Modes

Mode	Disadvantages	Advantages
Translating Siderostats	• Siderostat and delay line motion during data mode • Metrology tracking required • Changing structural plant	• Inertially fixed attitude control • Coverage and imaging time adjustable
Line-of-Sight Rotation and Tilt	• Delay line motion • Changing structural plant • Roll control about arbitrary axis	• No siderostat motion during data mode • No metrology tracking • Coverage and imaging time adjustable
Line-of-Sight Rotation	• Additional mass and power • Roll control about single axis • Coverage and imaging time fixed	• No siderostat or delay line motion during data mode • No changing structural plant • No metrology tracking

2.5.2 Procedure for Determining Configuration Trade

In all calculations, a maximum primary mirror diameter of 79 cm is assumed. Recall that this is the maximum diameter that will fit inside the truss beam cross-section. The performance impact of this assumption is examined in section 2.7. To evaluate the "best" number of siderostats and the better science operating mode, a set procedure will be used. Each discrete number from 3 to 8 siderostats is considered with the minimum set by the desire for a symmetrical mass distribution, and the maximum set by total mass considerations. Symmetrical mass distribution is desirable in order to minimize gravity gradient torques that drive attitude control actuator sizing. The first step in the trade procedure is to choose an arrangement that minimizes redundancy in baseline lengths and provides relatively good symmetry distribution for each number of siderostats. Since the number of baseline lengths is given by

$$n_{bl} = \frac{n_{sid}!}{2!\,(n_{sid}-2)!} \qquad \text{Eq. 2-12}$$

the problem of determining positions that give non-redundant baselines gets complex for large n_{sid}. Each possible arrangement is considered with two siderostats positioned in vertices to give the maximum 35 m baseline and the remaining siderostat positions stepped in one meter increments. For each arrangement, the corresponding baseline lengths are found and sorted. The mean and standard deviation of the differences in each consecutive baseline length are then found. "Good" patterns are those that have a large mean and small deviation in the baseline differences. A large mean implies a pattern that covers most of the range from 0 to 35 m baseline length, and a small deviation implies a pattern that has baselines distributed relatively evenly over the range. For each number of siderostats, all possible patterns are searched for the 10 to 15 "best" patterns according to the above criteria. These patterns are then examined to determine which one gives the most symmetric mass distribution. This pattern is then chosen as "best" for the given number of siderostats.

The second step in the procedure is to determine the amount of Fourier coverage given by the "best" pattern. If the coverage is less than the required 65%, then the spacecraft must tilt with respect to the LOS in order to generate additional baseline lengths. The tilt angles used are those that minimize redundancy in baseline lengths and that minimize the total tilt angle required. The number and angles of the tilts are then recorded in addition to the total amount of coverage given by the pattern. Only for the maximum

number of siderostats (eight) are no tilt angles required. Eight siderostats, then, represents the data mode that uses only LOS rotation.

Once the siderostat pattern and tilt angles are determined, the last step is to estimate the performance and cost parameters. Performance is measured by the amount of U-V plane coverage and the time required to image the baseline mission, as defined in Table 2-1. The cost parameters are the estimated mass and power consumption, and the estimated cost of the primary optics (siderostat and primary mirrors). Each siderostat entails an actual siderostat mirror, the beam compressor, a pathlength compensation device (PCD), and assorted fast steering mirrors. As shown in the mass and power listing in Appendix A, the estimated mass of an additional siderostat is approximately 245 kg with a 25% design margin. Each siderostat also requires approximately 75 W power for operation. The actual cost of the primary optics is estimated assuming cost directly proportional to the radius, with a one meter mirror costing approximately one million dollars [30]. These parameters are combined and compared as described in the following section.

2.5.3 Results of Payload Configuration Trade

The relevant parameters for each number of siderostats are shown below in Table 2-4, with normalized values on the second line of each entry. The Fourier coverage is rather simply derived by computing the annular area swept out by the collecting optics at each baseline length and dividing by the entire 35 m aperture area. The integration time is derived from equations 2-2 and 2-3. For the baseline mission the integration time required by a single telescope pair is 82 seconds. Since each telescope is matched with (n_{sid}-1) other telescopes, the total integration time per data point is (82 sec)(n_{sid}-1). The total time for imaging includes the time required for each data point through the rotation of 180°, the time required to initiate the LOS rotation, and the time required for tilting the spacecraft with respect to the LOS. The optics mass and power values are simply 245 kg per siderostat plus the spacecraft dry weight and 75 W per siderostat plus the spacecraft peak power. The cost of the major optical components is $1 million times the average radius (0.395 m for the primary and 0.559 m for the siderostat). The last parameter shown is a measure of the system reliability, assuming each siderostat has a reliability of 0.9. Naturally, the system reliability increases with the redundancy of additional components, but the total is proportional to only (n_{sid}-1) since a lone siderostat would be relatively useless.

To compare the six options, all six performance and cost values need to be combined. The first step is to normalize each parameter. The performance measures are normalized by the mission requirements of 24 hours and 65%, and the mass and power are

Table 2-4 Interferometer Payload Configuration Trade Parameters

Number of Siderostats	Number of Tilt Angles	Time Required (hrs) (NT)	U-V Coverage (%) (N%)	Optics Cost ($M) (NC)	System Mass (kg) (NM)	System Power (W) (NP)	Reliability (R)	Trade Parameter (P)
3	9	28.89 1.204	64.4 0.991	2.615 0.0043	10677 1.074	3375 1.071	0.99	4.4798
4	5	24.36 1.015	65.7 1.011	3.487 0.0070	10922 1.099	3450 1.095	0.999	4.8957
5	4	27.36 1.140	73.6 1.132	4.539 0.0091	11167 1.123	3525 1.119	0.99999	4.4115
6	2	17.12 0.713	68.9 1.060	5.231 2.000	11412 1.148	3600 1.143	1.0000	6.2065
7	2	22.16 0.923	78.7 1.211	6.103 0.0105	11657 1.173	3675 1.167	1.0000	5.1305
8	1	12.99 0.541	68.4 1.052	6.974 0.0139	11902 1.197	3750 1.191	1.0000	7.1771
Normalizing Value		24	65	500	9942	3150		

normalized by the estimated spacecraft dry mass of 9942 kg and peak power of 3150 W (these numbers do not include the mass or power of the optics). The optics cost is normalized by a rough estimate of the total system cost (about $250 million for the Titan IV and $250 million for the spacecraft), and the reliability is already normalized. The final trade parameter is found from the following equation:

$$P = \frac{N\%\cdot R}{NT}\left(\frac{1}{NC\cdot NM\cdot NP}\right)^{1/3} \qquad \text{Eq. 2-13}$$

The cube root is used to weight the three cost parameters as a single value in the equation, giving the performance parameters twice the weight of the cost parameters.

As the parameters indicate, the best option for the payload configuration is that with eight siderostats and no tilt angles. It offers significantly more performance, higher reliability, better sensitivity, and simpler attitude control operations at the cost of moderately larger mass, power, and dollar cost. Both the mass and the power remain within the bounds of our system and launch capacity. The driving factor in terms of performance is the imaging time, which is drastically increased when additional tilt angles are added to the process. In fact, some of the options with small numbers of siderostats and correspondingly large number of tilt angles are not able to meet the imaging rate requirement of greater than one image per day. The above analysis rather clearly illustrates that the best payload configuration for this particular spacecraft is an arrangement of eight siderostats with LOS rotation to vary the baseline angles. Figure 2-6(a), below, shows the pattern of these eight siderostats on the science plane face of the interferometer structure. Figure 2-6(b) shows the maximum aperture pattern generated by this arrangement of siderostats assuming a full 180° rotation. It covers 68.4% of the aperture with a fairly good spread in spatial frequencies.

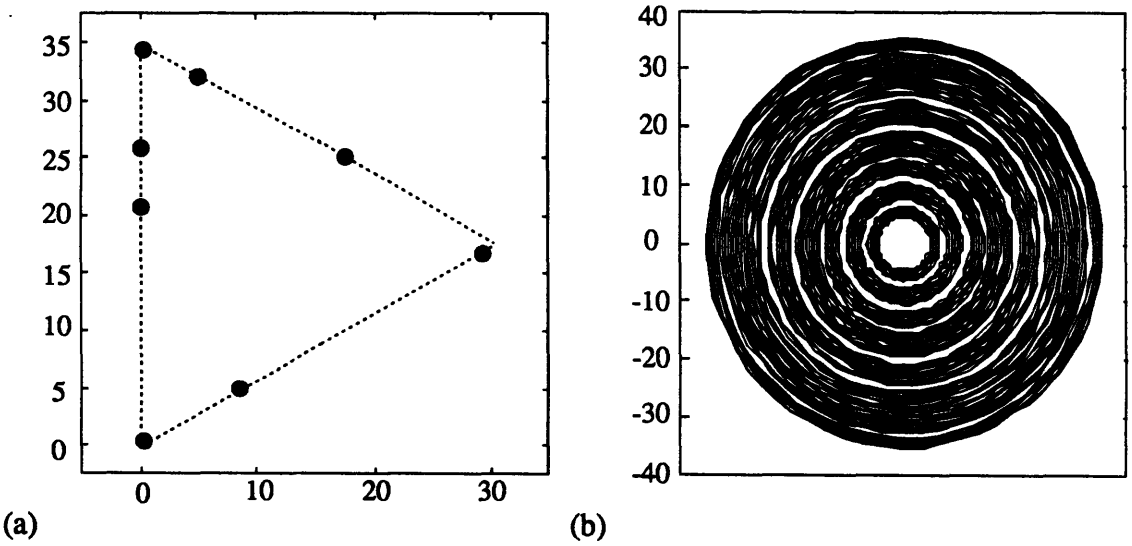

Figure 2-6 **(a) Minimum Redundancy Positions of Eight Siderostats on Tetrahedron Face (b) Aperture Pattern Generated by Eight Siderostat Arrangement**

2.6 Instrument Performance

With the payload configuration selected as described in the previous section, all of the top-level design choices have been made. The majority of the remaining work is in the more

detailed subsystem design and sizing. Before going into this material in Chapters 3 and 4, it would be interesting to see what effect the configuration selection has on instrument performance. By setting the siderostat diameter and number, the performance parameters specified in the mission requirements are determined.

The design parameter that probably has the largest impact on the astronomical performance of the system is the size of the discrete apertures. This strongly influences the sensitivity of the instrument and drives the time required for imaging. Figure 2-8 shows a plot of integration time per U-V data point versus relative stellar magnitude for apertures of 20 cm to 1.5 m diameter. The plots are derived directly from equations 2-2 and 2-3 assuming SNR = 5 and an image complexity of 45 pixels (values from baseline mission). The horizontal lines in the plot mark relevant time increments. For a desired maximum stellar magnitude of 20 and for a 0.79 m aperture, this instrument would require approximately two orbits integration time (~200 min) per data point. If the diameter were increased to one meter, the time required drops to only about one orbit. For targets around 20th magnitude, diameters much greater than one meter start to get diminishing returns.

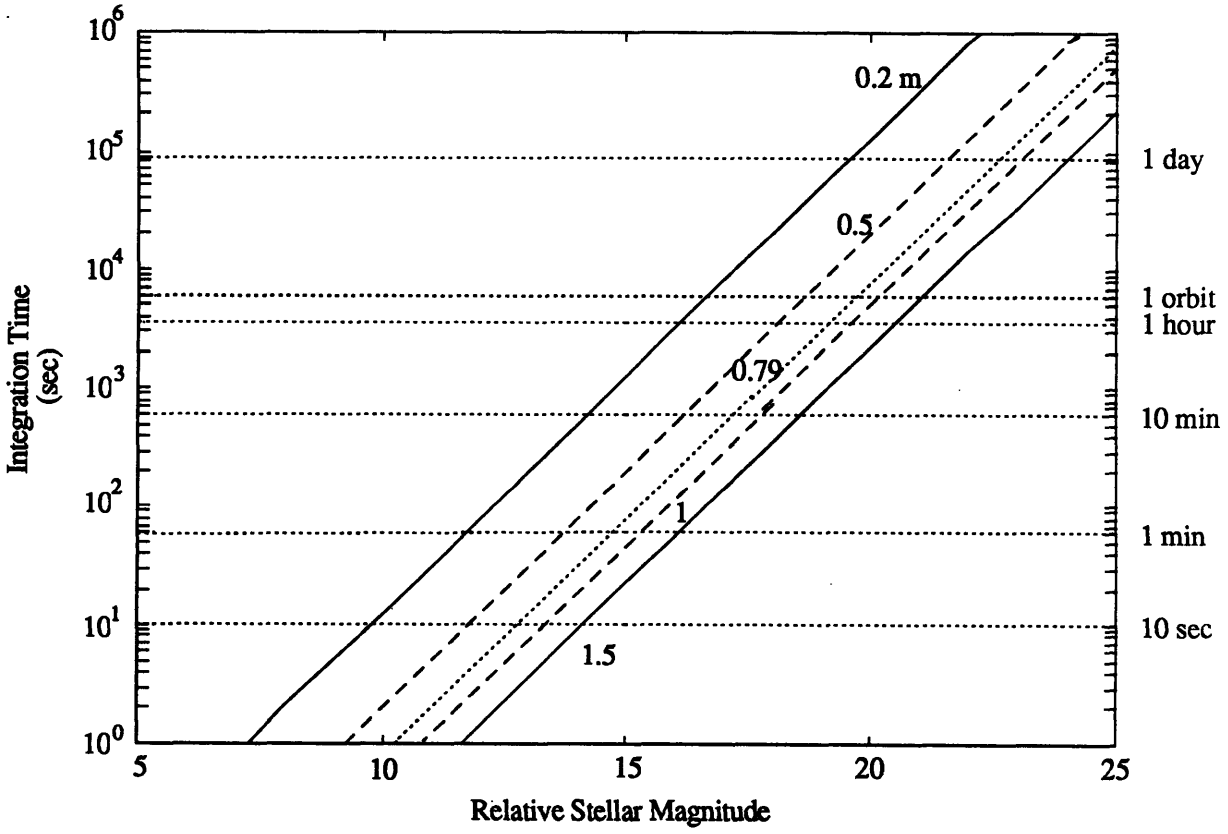

Figure 2-7 Integration Time as a function of Stellar Magnitude for Varying Aperture Diameters

The imaging performance can be examined in a slightly different way, as shown in Figure 2-8 on the next page. This is a plot of image complexity versus stellar magnitude assuming SNR = 5 and a one hour integration time. The plot indicates that for a magnitude of 20, the SERC interferometer can collect a single U-V data point on a target of approximately 30 pixels, and at 15th magnitude, the instrument can handle targets of about 300 pixels complexity with this integration time. Lastly, Figure 2-9 shows the capabilities of different apertures at performing 3 μ-arcsec astrometry. This plot is computed directly from equation 2-4. The interferometer spacecraft would be capable of this precision at 20th magnitude with an integration time of one orbit, and at 15th magnitude the figure of merit drops to just one minute. Plots such as these are useful tools for evaluating the performance of the instruments with different apertures. The primary performance parameters of the SERC Interferometer spacecraft are summarized in Table 2-5, along with their corresponding mission requirements.

Table 2-5 SERC Interferometer Astronomical Performance

Mission Requirement or Guideline	Interferometer Capability
• Resolution of 3 m-arcsec @ 0.5 μm	• Range of 0.3 - 1.0 μm with resolution of 1.8 - 5.9 m-arcsec
• Capable of 20 *m* observations SNR = 5 SNR = 5 in 82 sec	• Collects single U-V data point on target of ~30 pixels complexity in 1 hour at • Collects single data point of one pixel at 20 *m* and SNR = 10 in 16 sec • Image (max. U-V coverage) baseline mission of 15 *m* and 45 pixels at
• Imaging rate > 1 per day	• Image baseline mission in 13 hours
• U-V Coverage > 65%	• Maximum of 68.4% coverage
• Sensitivity comparable to HST	• 84% aperture area of HST
• 3 - 30 μ-arcsec astrometry @ 20 *m*	• 3 μ-arcsec @ 20 *m* in 99 minutes • 3 μ-arcsec @ 15 *m* in 1 minute

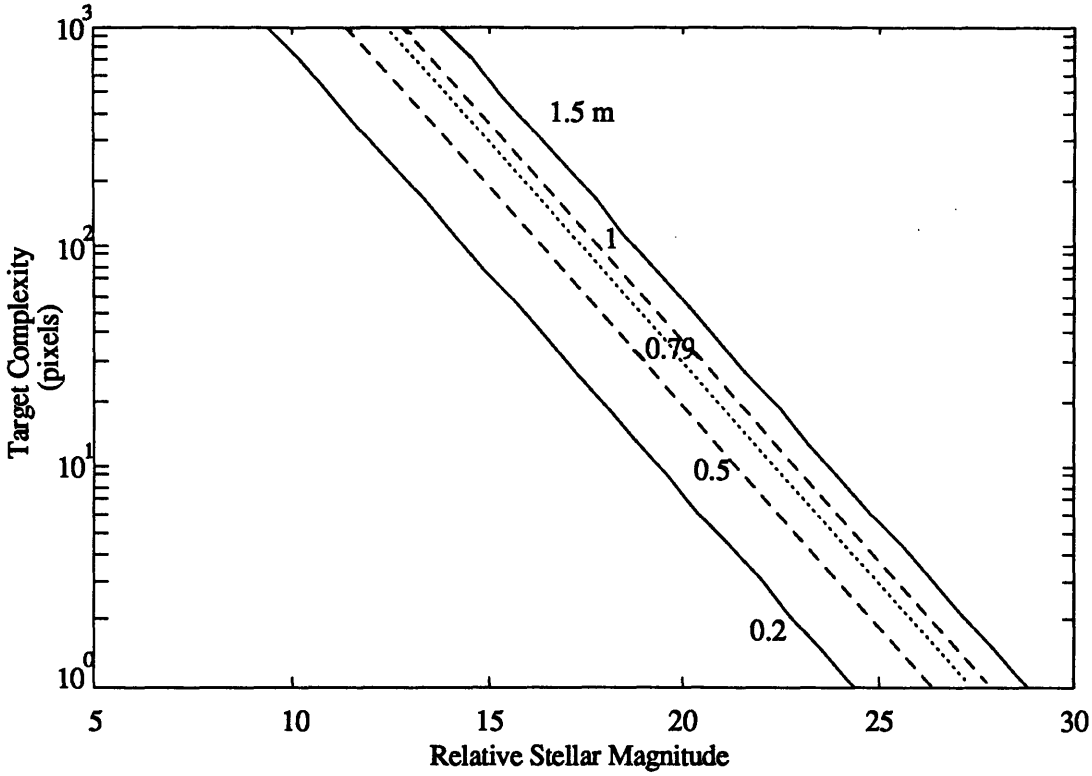

Figure 2-8 Imaging Capability as a Function of Stellar Magnitude

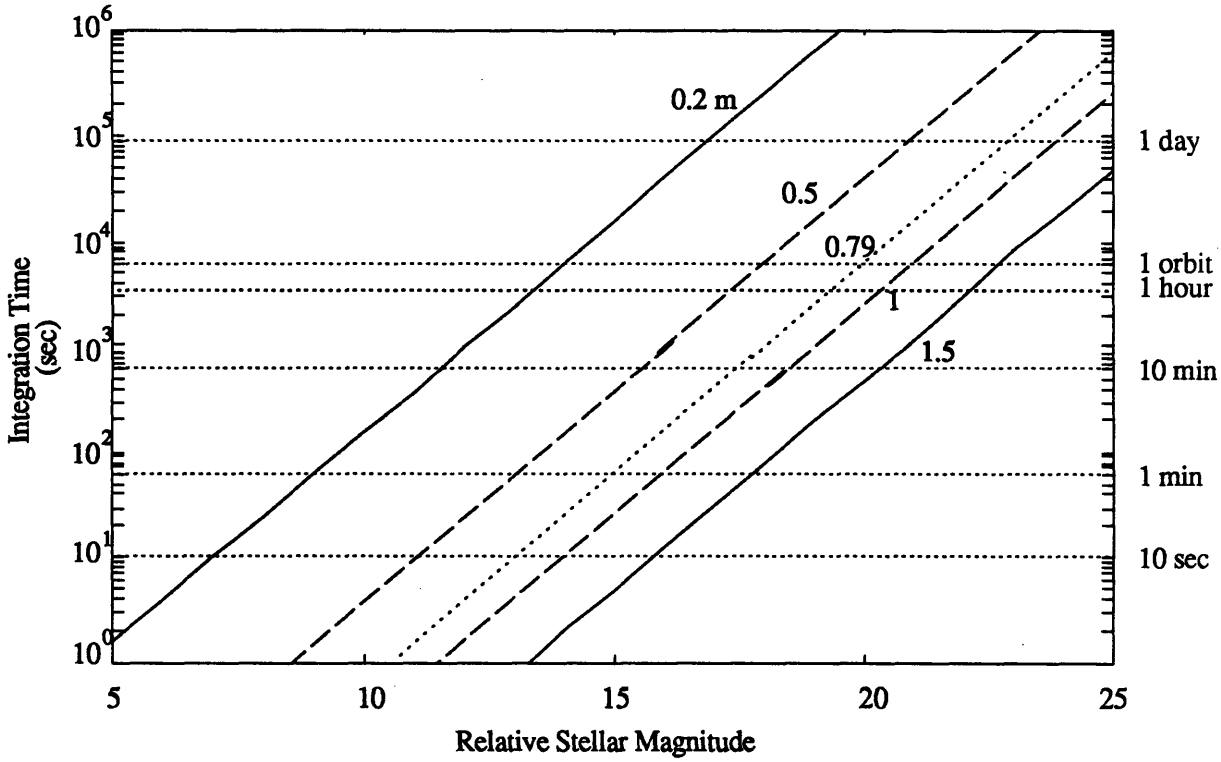

Figure 2-9 3 μ-arcsec Astrometry Capability as a Function of Stellar Magnitude

Chapter 3
Spacecraft Subsystems

The purpose of this chapter is to investigate the primary subsystem designs. It includes summaries of the attitude control, command and data handling, communications, power, and propulsion systems. The structure, structural control, and thermal analyses will be covered in Chapter 4. Each section in this chapter loosely follows a standard organization beginning with system requirements, identification of the main trades, and system architecture, and concluding with component selection and sizing and with an equipment and performance summary. Analyses are generally kept at a simple, first-order level, often using rule-of-thumb estimates for component units. For mass, power, and performance data, values are taken from product brochures where available, otherwise they are just estimated. Appendix A contains a complete listing of the spacecraft components with their mass and power requirements.

Throughout the chapter, there are two design principles unique to this spacecraft that are frequently referenced. The extremely precise nature of interferometry establishes minimization of spacecraft structural excitation as the cardinal rule of interferometer system design. This rule usually manifests itself in the decision to entirely eliminate sources of mechanical noise, sometimes at the expense of increased mass and complexity. The second principle, specific to this particular interferometer concept, aids the application of the first principle. It notes that the SERC Interferometer is not strongly constrained by individual component mass or volume. The sheer physical size of the structure precludes the use of any launch vehicle smaller than a Titan IV; consequently, subsystem mass is constrained only by the requirement that the total wet mass be less than about 12,500 kg. Likewise, the subsystem volume is relatively unconstrained. While the total structural volume is constrained by the payload fairing, there is over 15 m^3 of volume available within the vertices alone. This relative freedom in terms of mass and volume is unusual in spacecraft design, and allows the complete elimination of some common sources of mechanical vibration.

3.1 Attitude Control Subsystem

The attitude control system (ACS) is generally responsible for the guidance, navigation, and pointing functions of the spacecraft through each phase of the mission. Initially, it must navigate and guide the satellite during the transfer orbit and circularization burn, then it must control the deployment of the truss into the tetrahedral configuration. Through the bulk of the mission, its primary task is attitude determination and pointing control during acquisition of science data. Obviously, the system must be inertially oriented, which requires three-axis control. The following analysis concentrates on the science portion of the mission since that places the most stringent requirements on the system.

3.1.1 Requirements Definition

The requirements that drive the ACS design are shown below in Table 3-1. The mission lifetime is taken from the mission requirements specified in section 2.2, and the altitude range represents that expected from worst case orbital decay over the lifetime. The minimum altitude of 600 km is used hereafter in actuator selection and sizing since environmental disturbances increase with decreasing altitude. Using the minimum altitude then ensures that the spacecraft will be able to function effectively through the end of its mission.

Table 3-1 Attitude Control System Requirements

Mission Lifetime	10 yrs
Altitude Range	700-600 km
Slew Rate	90 deg/75 min
Science Mode Rotation Rate	90 deg/7.9 hrs
Time for LOS Spin-Up	$t \geq 100$ sec
Science Mode Pointing Accuracy	0.01 arc-sec
Science Mode Pointing Stability	0.007 arc-sec/sec

The slew rate is selected to provide a reasonable time for reorienting from one target to the next and includes the time needed to start and stop the rotation. At 90° in 75 minutes, the interferometer is able to point to any possible direction within 2.5 hours. Usually the time to point to a new target will be considerably less than 2.5 hours since the reorientation will not be over a full 180°. As shown later, the slew requirement is a major contributor to the actuator momentum load, but does not really drive the torque loads. The science mode

rotation rate is the maximum rate that can be tolerated as defined by the instrument integration time. Recall from Chapter 3 that the integration time for the baseline mission is (82 sec)(n_{sid}-1). Continuous rotation about the line of sight (LOS) can be used to generate different baseline angles only if the rotation rate is slow compared to the integration time. The minimum time for LOS spin-up is set by the desire to use a shaped torque command with frequency content at least an order of magnitude below that of the structure's fundamental mode. While this requirement specifies only a minimum, the time required for the spin-up should be kept near this specification in the interest of minimizing overall mission time. The science mode pointing requirements are those required in order to accomplish interferometry as specified in [19]. The pointing must be controlled to this high level to reduce the wavefront tilt errors that reduce the performance of the imaging process, and to keep the target within the interferometer's field of view. It should be noted here that the accuracy required from the attitude control system is the same as that specified for HST [10]. Although the actuator authority required to achieve this level of accuracy is quite large due to the interferometer's large size, the accuracy level itself is within the realm of current capability.

3.1.2 System Architecture

The very nature of the astronomical mission requires the interferometer to be inertially pointed, which in turn requires three-axis control. There are really only three trades involved in the ACS three-axis design, two of which can be resolved in full merely through logical argument. The trade that requires some quantitative assessment is the choice of control actuators. With such precise control requirements, the only actuators that are feasible are some sort of momentum exchange wheels, but whether these should be reaction wheels (RWA's), control moment gyros (CMG's), or a hybrid of both is a trade that is addressed in a following section. Since all of these options will require a mechanism for desaturating the wheels, there is a second trade for actuator selection. The only two practical choices are propulsion thrusters and magnetic torque rods. The decision between these two is easily solved by considering the issue of contamination. The effluents from propulsion units will contaminate the optical components of the system, with the possibility of seriously degrading the performance of the instrument. In the face of this possibility, the only logical choice is a magnetic torque system. The details of the magnetic system are addressed later in the actuator sizing section.

The third trade that must be considered is the manner in which the precise levels of attitude control are achieved, whether by actuating the entire spacecraft or just part of the

payload. The solution of this has already been assumed to a certain extent in the design of the collecting optics. One method of control is to simply use fixed telescopes and then point the entire spacecraft in the manner of HST. The other possibility is to use a siderostat mirror before the primary mirror in tip and tilt mode to achieve precise control at a high frequency. The choice between the two is fairly simple if one considers the energy required to move eight 0.79 x 1.117 m elliptical siderostats at high frequency versus that required for a 35 m tetrahedral truss. The siderostat approach requires somewhat more mass for the additional optics and motors, but results in far less stress on the main attitude control system which can now be allowed to operate at a much lower frequency.

The last point to consider in the ACS architecture is reliability and system redundancy. The use of wheel actuators implies at least three separate assemblies in order to get control authority in all three axes. Normally, to enhance reliability, a fourth wheel is added that permits three-axis control even in the face of actuator failure. Since the center of mass of the interferometer is in the open space at the center of the tetrahedron, the actuators cannot be placed near the center of mass. Instead they are placed in each of the four vertices with their axes pointing to the center of mass. This symmetric arrangement maintains the inertial properties of the spacecraft while providing redundancy for three axis control.

3.1.3 Disturbance Quantification

Several natural forces act on the spacecraft to torque it about its center of mass. The effects of each on the interferometer are described in this section and summarized in Table 3-2. More detailed derivation of these effects can be found in numerous reference texts such as [1,13,39]. All of these effects are computed for the worst case 600 km altitude. Note that all of the values listed in the table represent estimates of the peak disturbance forces. Since it is not expected that all disturbances will be in phase, the total cyclic and secular values are computed as the root sum square.

The strongest disturbance force is that due to gravity gradients, or the minute differential in gravitational force between one part of the spacecraft and another. Gravity gradient torques can be separated into cyclic and secular components that depend on the inertial properties of the spacecraft. The torques and their consequent angular momentum are computed from the following equations:

$$\tau_{cyc} = \frac{3\mu_e}{R^3} \times \Delta I_p \quad H_{cyc} = \frac{3\mu_e^{1/2}}{2R^{3/2}} \times \Delta I_p \qquad \text{Eq. 3-1(a)}$$

$$\tau_{sec} = \frac{3\mu_e}{R^3} \times \Delta I_{cross} \quad H_{sec} = \frac{3\pi\mu_e^{1/2}}{R^{3/2}} \times \Delta I_{cross} \qquad \text{Eq. 3-1(b)}$$

where ΔI_p refers to the largest difference in principle moments of inertia, and ΔI_{cross} refers to the largest inertia coupling term. If a coordinate frame is defined with the origin at the center of mass, the z axis in the direction of the line of sight, and the y axis through one of the near legs of the tetrahedron, the inertia matrix is

$$\begin{bmatrix} 2.40\text{x}10^6 & & \text{symm.} \\ -9.18\text{x}10^3 & 2.35\text{x}10^6 & \\ 2.66\text{x}10^4 & -1.93\text{x}10^4 & 1.92\text{x}10^6 \end{bmatrix}$$

The resulting principle moments of inertia are

$$\begin{bmatrix} 2.3488\text{x}10^6 & & \\ & 2.4035\text{x}10^6 & \\ & & 1.9177\text{x}10^6 \end{bmatrix}$$

The above matrices lead to a ΔI_p = 485,800 kg·m^2 and maximum ΔI_{cross} = 26,600 kg·m^2. The resulting gravity gradient torques are 0.094 Nm secular and 1.71 Nm cyclic, with 272 Nms and 789 Nms angular momentum, respectively.

The second largest disturbance is due to solar radiation pressure. If the spacecraft presents a non-symmetric cross-section to the sun, the radiation pressure will produce an off-center net force. The torque produced by this net force can be estimated by

$$\tau_{rad} = P_r A_r L(1+q)\ \cos i \qquad \text{Eq. 3-2}$$

where P_r is the solar radiation pressure of 4.617 x 10^{-6} N/m^2, A_r is the cross-sectional area of 253 m^2, L is the center-of-pressure to center-of-mass offset estimated at 5 m, q is the reflectance factor of 0.6, and *i* is the angle of incidence estimated at 0°. These factors give an estimated torque of 0.009 Nm. The solar pressure angular momentum is simply the torque integrated over one orbit, or 54 Nms.

Aerodynamic forces can also produce net torques on the spacecraft if a non-symmetrical cross-section is presented with respect to the velocity vector. The torque can be approximated by

$$\tau_{aero} = \frac{1}{2}\rho v^2 C_D A L \qquad \text{Eq. 3-3}$$

where C_D is assumed to be 2.2, ρ is 1.14×10^{-13} kg/m^3 at 600 km altitude, v is orbital velocity, A the cross-sectional area, and L the estimated offset of 5 m. The estimated aerodynamic torque is 0.009 Nm with 54 Nms angular momentum.

The magnetic field also acts to disturb the orientation of the spacecraft according to the following equation

$$\tau_{mag} = \mu \times B \qquad \text{Eq. 3-4}$$

where μ is the spacecraft net magnetic dipole moment estimated at 40 A·m^2, and B is the earth's magnetic field of approximately 3×10^{-5} T. The resulting torque and angular momentum are 0.001 Nm and 7 Nms.

Table 3-2 Estimated Environmental Disturbance Torques

Environmental Effect	Torque Level (N m)	Angular Momentum (N m s)
Gravity Gradient		
(secular)	0.094	272 per orbit
(cyclic)	1.710	789
Solar Radiation	0.009	54
Aerodynamic	0.009	54
Magnetic Field	0.001	7
Total Secular (RSS)	0.094	277
Total Cyclic (RSS)	1.710	791

3.1.4 Actuator Selection and Sizing

As already discussed, the control actuators will be some sort of momentum exchange wheel, with magnetic torque desaturation. The choice must still be made as to the type of wheel, and both magnetic and wheel actuators need to be sized. The first step in selecting the control actuators is to specify the torque and momentum loads they will be expected to carry. In order to minimize structural excitation, a smoothed torque command is used for both slewing to a new target and for initiating the line of sight rotation. Figure 3-1 shows the torque and angular velocity profiles for a slew of 90° in 75 minutes. The maximum torque and momentum required for the maneuver can be found from

$$\tau_{slew} = \frac{4\theta I}{t^2} \qquad \text{Eq. 3-5}$$

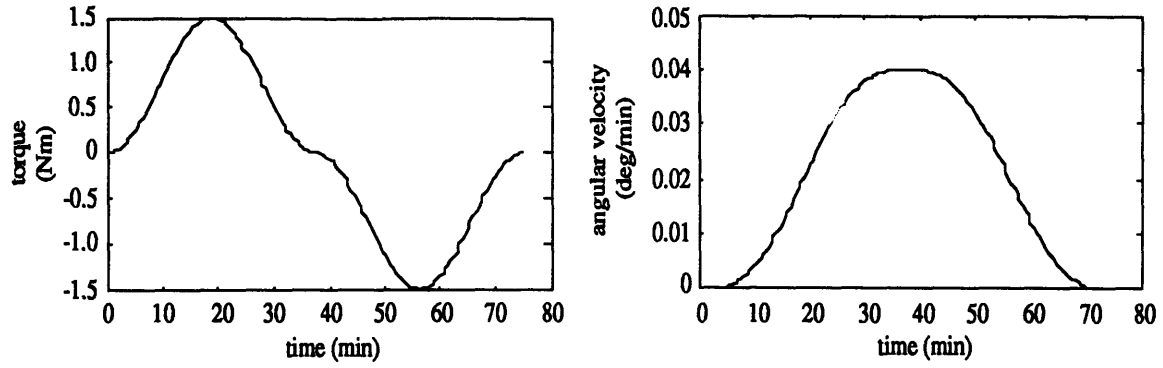

a) b)

Figure 3-1 (a) Smoothed Torque Command for 90° Slew Maneuver (b) Angular Velocity Profile for Slew Maneuver

For the required slew rate about the worst case moment of inertia, the resulting torque is 0.746 Nm with angular momentum of 839 Nms. For the LOS rotation, the required torque to initiate the maneuver is approximately

$$\tau_{LOS} = 2I \frac{\Delta\omega}{\Delta t} \qquad \text{Eq. 3-6}$$

To initiate the maneuver in 100 seconds requires 2.124 Nm torque and angular momentum of 106 Nms. If the maximum torque and momentum from these two maneuvers are root sum squared with the environmental loads, and a design margin of 1.5 is used, then the total actuator loads are those shown in Table 3-3.

Table 3-3 ACS Actuator Loads

	Torque (Nm)	Angular Momentum (Nms)
Total Cyclic	4.09	1730
Total Secular	0.141	415

Now the ACS actuators can be selected and sized. The first step is to determine the desaturation system. The wheel actuators should be able to handle the cyclic loads that are sinusoidal at the frequency of the orbit, but they cannot compensate for the secular loads over a long period of time. If the magnetic torque system is to prevent the wheels from becoming saturated, it must be able to account for the secular loads on the system. The magnetic torque loads are then 0.141 Nm torque and 415 Nms momentum. The magnetic dipole needed to meet these requirements can be found from:

$$D = \frac{\tau}{B\left(10^{-7}\right)} \qquad \text{Eq. 3-7}$$

where τ is the required torque, B is the earth's magnetic field in gauss estimated at 0.4, and D is the dipole in pole·cm. This gives a value of $D = 3.525 \times 10^6$ pole·cm ≈ 3525 A·m^2. Since a design margin of 1.5 has already been assumed in determining the loads, additional margin in the actuator size is unnecessary. The torque rods used in HST give a magnetic moment of 3600 A·m^2, so these are selected as the hardware for the interferometer. The rods are 2.1 m long and 8.9 cm in diameter, weigh about 45 kg each, and consume up to 16 W of power [9]. In order to give three-axis redundancy, four of these rods are used, one in each vertex, for a total mass of 180 kg and a total power of 64 W.

Finally, the trade must be made as to which type of wheel actuator will be used. The only real choices for control actuators are either CMG's or RWA's, which leads to something of a dilemma. RWA's typically provide excellent accuracy, but insufficient authority. CMG's provide more than enough authority, but relatively poor accuracy. To study this trade more closely, three systems are considered: one with only CMG's, one with only RWA's, and a hybrid system that uses both. All options assume a magnetic suspension/isolation system similar to those described in [3,17] to help eliminate vibrations. This improvement comes at the expense of 36 kg and 57 W for each isolation unit. The formulas used to estimate the mass and power requirements for each actuator below are taken from [39].

Option 1: CMG's only. In this case, the CMG's are assumed to have sufficient gimbal-angle measurement, control, and stability to meet the science mode pointing requirements. The CMG's will have to meet both the maximum torque of 4.09 Nm and the maximum momentum of 1730 Nms about each axis. Using estimates from [39], and adding the weight and power for the magnetic isolation system described in [3], we can then find the mass and power per CMG.

$$M \approx 35 + 36 + 0.05H = 157.5 \text{ kg}$$
$$\text{S.S. Power} \approx 30 \text{ W} + 57 \text{ W} = 87 \text{ W}$$
$$\text{Peak Power} \approx 0.2\,\tau \text{ W} + \text{SS Power} = 88 \text{ W}$$

If one CMG is assumed in each vertex to provide both redundancy and inertia balance, the following system mass and power are found:

$$M_{CMG} = 630 \text{ kg}$$
$$\text{S.S. } P_{CMG} = 348 \text{ W}$$
$$\text{Peak } P_{CMG} = 352 \text{ W}$$

Using this option, the interferometer is easily able to accomplish the LOS spin-up maneuver within 100 seconds.

Option 2: RWA's only. In this case, the assumption is made that reaction wheels capable of providing 1.3 Nm torque and 900 Nms momentum are available. Two reaction wheels are placed in each of the four vertices, thus yielding a total capacity of 2.6 Nm torque and 1800 Nms momentum. This option concedes the fact that it may not be able to meet the torque load for a 100 sec LOS spin-up on demand. The main restriction in performance is that the LOS rotation cannot be initiated at the same time and direction as peak environmental loads. The actuator requirements are then 2.6 Nm and 1730 Nms momentum for each axis. Once again using the estimates from [39] and adding mass and power for one magnetic isolation system in each vertex, the following mass and power are derived for each reaction wheel:

$$M \approx 5 + 18 + 0.1H = 113 \text{ kg}$$
$$\text{S.S. Power} \approx 25 \text{ W} + 28.5 \text{ W} = 53.5 \text{ W}$$
$$\text{Peak Power} \approx 500\tau \text{ W} = 650 \text{ W}$$

Using two of these reaction wheels in each of the vertices yields a total system mass of 904 kg, an average power of 428 W, and a peak power of 1621 W. Again, the main restriction with this system would be a prohibition against initiating a LOS rotation at the same time and direction as peak environmental loads. The coincidence of these two torque demands is expected to be a relatively rare occurrence, and would at worst introduce a delay of about 15 to 20 minutes in initiating the next rotation.

Option 3: CMG's and RWA's. In this option, no advancement in current actuator technology is assumed. Low accuracy CMG's and low authority RWA's are used in a complementary two-stage scheme to meet the necessary requirements. The CMG's are used for the high torque and high momentum slew loads, while the RWA's are used for precision control during the science mode. It is assumed that the RWA's must meet only the cyclic environmental loads, since slewing tasks will be handled by the CMG's and secular environmental loads by the magnetic system. The expected loads for the RWA system are 2.6 Nm torque and 1185 Nms angular momentum. If three reaction wheels are used in each vertex, then the unit torque and momentum requirements are 0.87 Nm and 395 Nms. Using the formulas from option 2, this gives unit characteristics of

$$M_{RWA} \approx 56.5 \text{ kg}$$
$$\text{S.S. } P_{RWA} \approx 43 \text{ W}$$
$$\text{Peak } P_{RWA} \approx 1687 \text{ W}$$

The CMG's of this two-stage system will be required to meet the slewing loads of 3.186 Nm torque and 1300 Nms momentum. From the formulas in option 1, the unit characteristics are

$$M_{CMG} \approx 136 \text{ kg}$$
$$\text{S.S. } P_{CMG} \approx 87 \text{ W}$$
$$\text{Peak } P_{CMG} \approx 88 \text{ W}$$

With three reaction wheels and one CMG in each vertex, the total system mass and power for this option will be 1222 kg, 864 W average, and 2039 W peak.

The important system parameters for all three options are summarized in Table 3-4. The dramatic difference in mass and power between the systems is immediately apparent. The conclusion to be drawn from this is that by pushing for advances in technology

Table 3-4 ACS Actuator System Options

System Component	Units	Option 1 CMG	Option 2 RWA	Option 3 Hybrid
CMG				
Total Torque	Nm	4.09	-	3.19
Total Momentum	Nms	1730	-	1300
Unit Torque	Nm	4.09	-	3.19
Unit Momentum	Nms	1730	-	1300
Unit Mass	kg	157.5	-	136
Unit Ave. Power	W	87	-	87
Unit Peak Power	W	88	-	88
Quantity		4	-	4
Development Risk		High	-	Current
RWA				
Total Torque	Nm	-	2.6	2.6
Total Momentum	Nms	-	1730	1185
Unit Torque	Nm	-	1.3	0.87
Unit Momentum	Nms	-	900	395
Unit Mass	kg	-	113	56.5
Unit Ave. Power	W	-	53.5	43
Unit Peak Power	W	-	650	435
Quantity		-	8	12
Development Risk		-	Low	Current
Magnetic Torquers				
Total Torque	Nm	0.141	0.141	0.141
Total Momentum	Nms	415	415	415
Unit Torque	Nm	0.141	0.141	0.141
Unit Mass	kg	45	45	45
Unit Ave. Power	W	16	16	16
Quantity		4	4	4
Development Risk		Current	Current	Current
System Mass	kg	810	1084	1492
System Ave. Power	W	412	492	928
System Peak Power	W	416	1685	2103

(options 1 or 2), large increases in total performance over the present state-of-the-art (option 3) can be achieved. Since it is fairly clear that in terms of mass and power, option 1 is better than option 2 which is better than option 3, the decision rests on how much confidence can be placed in advances in technology. The advance required in CMG technology for option 1 is an improvement in gimbal accuracy and noise. Unfortunately, there are no indications of expected advances in this area. Option 2 requires increases in either torque or momentum over current devices, and these advances are expected to occur within the next decade [25], clearly within the design time frame for this type of spacecraft. In fact, a high momentum (1350 Nms), magnetically suspended reaction wheel was developed and tested several years ago, although it was a low torque device [17]. Option 3 is well within the current state-of-the-art, which means that no new development is needed to meet the requirements, but the system adds complexity without the benefit of true redundancy, since neither the CMG's nor the RWA's could accomplish the other's task in the event of a failure. Because of the benefits of its advances in technology, and the relative confidence in its achievement, option 2 is selected as the baseline choice for the interferometer system. It is also recommended, however, that since it promises such a significant increase in performance, research should be pursued on improving CMG gimbal accuracy and noise to a level necessary for astronomical missions.

3.1.5 Sensor Selection

Determination of the required sensors is fairly straightforward. Primary navigation and orbital position knowledge are provided by ground track and an inertial measurement unit (IMU) during launch and deployment, and by TDRSS ranging measurements during the operating life. This should provide adequate position information since precise positional knowledge is not necessary for the mission. For attitude sensing, a variety of components are used in a layered approach according to degree of precision. A set of sun sensors provides the initial, rough estimates of attitude and feed information to star trackers for high accuracy attitude information. The star trackers are used to update the IMU which is the primary attitude sensor. During the science mode, additional precision is provided by a fine guidance interferometer (FGI) separate from the primary science interferometers. The FGI locks onto a bright guide star in the "background" around the target object and uses fringe tracking to determine pointing error. The FGI is the only instrument presently capable of providing sufficient accuracy for science mode pointing control. The component used in the mass and power listings is a device with 40 cm aperture diameter used in JPL's OSI design [23]. The last sensors that are required for the spacecraft are magnetometers

which are needed for use with the magnetic control system. The sensors, their quantity, and estimates of their mass and power are summarized in Table 3-5.

Table 3-5 ACS Sensor Component Summary

Component	Quantity	Unit Mass (kg)	Unit Power (W)
Sun Sensor	2	1.5	1
F. H. Star Tracker	2	15.0	10
IMU	1	17.0	23
FGI	2	43.4	36
Magnetometer	3	0.8	1
Sensor Total		139.2	120

3.1.6 Control Algorithm

For this section, rather than develop equations of motion for the spacecraft dynamics, the attitude control system is presented in a functional block diagram form which illustrates the flow of information and decisions/control. Only rigid body dynamics are addressed here; flexible motions are considered later in the structural control section of Chapter 4. Figure 3-2, below, shows the top level flow of the attitude control system. Disturbance torques affect the vehicle rotational dynamics in both rate and position. Rotational position errors are sensed from star light by the sun sensors, star trackers, and FGI, while rotational rate is sensed by rate gyros in the IMU. Sensed position and rate information is fed into the ACS computer which, based on the control law, commands torques on the reaction wheels and also feeds information to the magnetic control system. The reaction torque from the RWA's then affects the vehicle rotational dynamics.

The reaction wheel speeds are fed to the magnetic control system along with data from the magnetometers which sense the local geomagnetic field. The magnetic control system acts to reduce reaction wheel speeds to prevent wheel saturation. Based on the magnetic desaturation law, the ACS computer sends commands for varying current to the magnetic torquers. The interaction of the large magnetic torque rods with the earth's magnetic field generates torques which affect the vehicle rotational dynamics. Magnetic desaturation commands are ultimately counteracted by the reaction wheels resulting in reduced wheel speed.

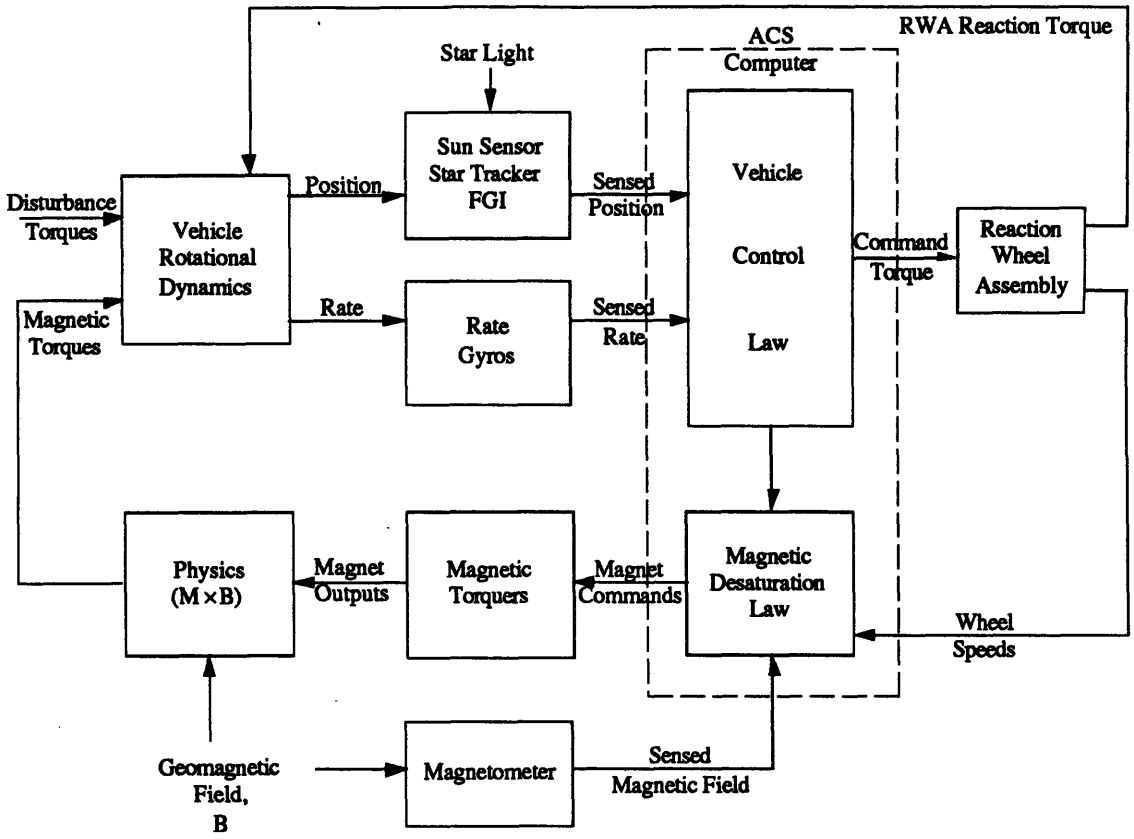

Figure 3-2 Attitude Control System Block Diagram

3.1.7 Subsystem Summary

The attitude control system is primarily responsible for orienting the spacecraft and maintaining very high precision pointing during science data collection. The system maintains three-axis control using an arrangement of two 1.3 Nm/900 Nms reaction wheels in each vertex of the tetrahedron. The RWA's are mounted in a magnetic isolation system that isolates the vibrational disturbances normally caused by rotor imbalances and bearing friction. Wheel desaturation is provided by magnetic torque rods of 3600 $A \cdot m^2$ moment in each vertex. The tetrahedral arrangement of actuators enhances reliability by providing an orientation in which at least two sets of actuators can act in any arbitrary axis. This allows for system operation in the event of the failure of any single station. The actuators are fed by attitude sensors including sun sensors, star trackers, and an IMU. The very precise attitude sensing required for data collection is provided by fine guidance interferometers tracking bright guide stars near the target. Magnetometers are also provided to supply the magnetic control system with necessary information about the earth's magnetic field. Finally, navigational information is given by communications link ranging information.

The actuator complement weighs approximately 1100 kg and consumes an average power of about 550 W. Peak power demand of almost 1700 W occurs with peak torque demands. With sensor suite characteristics of 140 kg mass and 120 W power, the subsystem totals are 1240 kg mass, 670 W average power, and 1850 W peak power.

3.2 Command & Data Handling Subsystem

The command and data handling (C&DH) subsystem is responsible for receiving, processing, and distributing all information on board the spacecraft. It must interface with all of the other subsystems on board the interferometer and with the ground through the communications subsystem. All subsystems have some data processing requirements that need to be met, and they need to supply information for telemetry on the spacecraft status. There exists a rather intimate relationship between the communications subsystem and the C&DH subsystem in that processing and storage requirements are largely driven by the capacity of the communications link. This section approaches the C&DH design by first examining the processing and storage requirements for each subsystem, including the payload, and then considering what type of architecture would best meet the needs of the entire system. Since the C&DH system is so vital to all of the other subsystems, this trade places a large emphasis on the inherent reliability of the various architectures.

3.2.1 Requirements Definition

To determine the requirements of the system, the separate requirements of each constituent part need to be examined. The processing tasks on the interferometer break down rather neatly into six major categories:

1) *Communications* for receiving, decoding, processing, and distributing commands and for collecting, formatting, encoding, and transmitting telemetry and data. Data fault detection and correction are also needed here for high accuracy transmission.

2) *Attitude Control* for collecting and processing sensor data, implementing the attitude control law, and sending the necessary commands to the control actuators.

3) *Subsystems* for fault detection and correction, power system regulation, thermal system regulation, and spacecraft autonomous functions that do not fall under any of the other categories.

4) *Global Structural Control* for receiving information about the optical pathlengths and metrology and implementing global control algorithms using actuators such as active struts, variable isolation mounts, and thermal elements.

5) *Pathlength Control* for implementing the pathlength control devices/delay lines. These will be closely tied to the global structural control processor.

6) *Science Data* for collecting, processing, storing, and releasing the science and metrology data.

For each of these processing categories, the required memory and throughput can be estimated. The estimates for the first five categories are based largely on typical values described in [39]. The main results are summarized here, while a more detailed discussion is presented in Appendix B. The science data processing requirements are derived from the actual amount and type of data that is acquired, the rate at which it is taken, and the amount and type of data that is transmitted to the users. Since the large amount of science data generally drives the system size, its requirements are described here in detail.

For each processing category, the total processing job is broken down into individual application tasks. Executive processors to run the operating system and control input/output tasks are similarly addressed. Typical values for each processing task are considered in terms of throughput (based on the desired frequency of the task), and code and data memory. The requirements are then totaled and roughly multiplied by a factor of two. This large margin accounts for both a suggested 50% uncertainty in initial requirements and for another 50% spare capacity for on-orbit adjustment and expansion. In all cases, a 16 bit, 1750A class processor is assumed with a high level software code such as Ada. The processing requirements for each category are discussed below and summarized in a series of tables.

Communications: The communications processor has three application tasks: ground command processing, spacecraft telemetry processing, and payload data processing. Communications processing involves mostly formatting and encoding data, and decoding and distributing commands. The encoding and decoding are necessary because the TDRSS requires prefixes and encoding to differentiate users. Values for

command and telemetry tasks are derived in Appendix B. The processor requires about 26 K of memory and 28 KIPS of throughput.

Attitude Control: The ACS processor must receive data from the attitude sensors, process the data through the control algorithm, and then generate commands for the actuators. The sensors used on the interferometer are rate gyros, sun sensors, star trackers, magnetometers, and a fine guidance interferometer,. The actuators used are magnetic torquers and reaction wheel assemblies. Implementation of the control algorithm entails the use of both kinematic integration and error determination. Finally, data for orbit and ephemeris propagation processing have been included. Taking all these factors into account, the complete ACS processor requires about 95 K of memory and 196 KIPS throughput.

Subsystem Control: As stated in the first section, the subsystem controller is responsible for system wide fault detection and correction, thermal and power management, and other autonomous tasks. It is estimated to require a total of 92 K of memory and 96 KIPS of throughput.

Global Structural Control: Structural control entails accepting information from the metrology system and the pathlength fringe trackers and determining the appropriate commands to send to the actuators. With the control system running at approximately 1000 Hz, the required processing can be estimated from that needed for a Kalman filter. Based on this, the estimate is for the processor to require 18 K of memory and approximately 20 MIPS throughput. Note that the throughput requirements for structural control are quite large. This is due to the large number of states that must be run in the controller and to the high frequency of operation.

PCD Controller: The optical pathlength control is a subset of the global structural control, and can be approached in one of two ways. In the first case, the 29 pairs of optical pathlengths (including the FGI) can be controlled to prevent differential pathlength errors, yielding 29 variables that have to be controlled. In the second case, each of 7 science pathlengths can be controlled to match the eighth pathlength, and one of the FGI legs can be controlled to match the other. The second case yields only 10 variables that need to be controlled. The implication here is that the option with the fewer variables will require less processing, and therefore is the preferred option. Each of the pathlength control devices requires its own processor to accept information on the pathlength from the global controller and then send commands to the actuators in the device. It is assumed that these

devices operate at about 2000 Hz, and require about 132 K of memory and 1.76 MIPS of throughput. Even though the PCD operates at twice the frequency of the global structural controller, it has a significantly lower number of inputs, outputs, and states. The result is a much lower throughput requirement.

Science Data (Payload): The payload processor is approached in a different manner than the other processing categories. There are no typical values available to use in estimating the requirements, so instead the data rates and total amounts of data are estimated. There are three relevant questions that guide the estimation process:

1) What is the input to the payload processor?
2) What is the output from the payload processor?
3) What data needs to be stored?

The answers to these questions give the input and output data rates and volume, and the necessary storage capacity. It is important to point out at this time that the vital information for the scientific mission is the pixel data, and that the pathlengths and baseline vectors are needed for post-processing of the image [19].

Data is received by the science processor from the communications processor, the ACS processor, the mass memory unit (MMU), the CCD's, the metrology system, and the pathlength detectors. Since the ACS information is of a "start/stop" command nature, and since ground commands via the communications processor will not occur during science mode, neither of these inputs need to be considered in sizing the payload processor. Likewise, data from the MMU is supplied only on demand, so it too can be ignored. The only remaining relevant data inputs are those of the CCD's, the metrology system, and the optical pathlengths.

The following information is assumed about the CCD detectors. There are 28 detectors, one for each unique pair of baselines. In the worst case, data are released from the arrays every 574 seconds (82 sec)(n_{sid}-1). Each detector is a 2000 x 2000 pixel array, the standard silicon array size for current technology [7]. It is also assumed that each pixel yields 16 bits of information, and that for the nominal mission, there are 1444 distinct baselines over a period of 13 hours. From this information, the peak and average raw data rates and the raw data volume per image can be determined:

$$DR_{CCD} = \frac{(2000^2 \text{ pix/det})(16 \text{ bits/pix})(28 \text{ det})}{574 \text{ sec}} = 3.122 \text{ Mbps peak} \quad \text{Eq. 3-8}$$

$$D_{CCD} = (2000^2 \text{ pix/bline})(16 \text{ bits/pix})(1444 \text{ bline}) = 92.4 \text{ Gbit} \quad \text{Eq. 3-9}$$

$$DR_{\overline{CCD}} = \frac{92.4 \text{ Gbit}}{46800 \text{ sec}} = 1.97 \text{ Mbps average} \quad \text{Eq. 3-10}$$

For the optical pathlength processing, 10 pathlengths are assumed (8 science and 2 FGI) at a sampling frequency of 2000 Hz. With 16 bits per sample and science mode time of about 13 hours, the average pathlength data rate and volume are:

$$DR_{PL} = (10 \text{ pathlengths})(16 \text{ bits/pathlength})(2000 \text{ Hz}) = 320 \text{ kbps} \quad \text{Eq. 3-11}$$

$$D_{PL} = DR_{PL}\,(46800 \text{ sec}) = 14.98 \text{ Gbit} \quad \text{Eq. 3-12}$$

The metrology data is calculated in a similar way. There are 33 laser legs, at 16 bits per leg, sampled at 2000 Hz for a period of 13 hours. This yields:

$$DR_{MET} = (33 \text{ legs})(16 \text{ bits/leg})(2000 \text{ Hz}) = 1.056 \text{ Mbps} \quad \text{Eq. 3-13}$$

$$D_{MET} = DR_{MET}\,(46800 \text{ sec}) = 49.42 \text{ Gbit} \quad \text{Eq. 3-14}$$

This all gives a grand total of 4.498 Mbps peak and 3.356 Mbps average data rates and 149.82 Gbit of data per image. This extremely large amount of raw data presents a strong case for a significant amount of on-board processing and data compression.

The data that is passed from the science data processor to either the communications processor for transmission or to the MMU for storage is only that data which is necessary for the scientists. As stated above, the information that the scientists require is the pixel data, and the pathlength and baseline vectors as functions of time. Both the pixel data and the pathlength data are essentially the same as the input to the processor. The baseline vectors, however, need to be reduced from the metrology data. Either the baseline vectors themselves or the positions of the siderostats can be transmitted. Transmitting the vectors would require 28 x 3 = 84 words per time point. For the siderostat positions, 9 x 3 = 27 words per time point would need to be transmitted (8 for the science siderostats and 1 for some inertial reference such as the IMU). At a 2000 Hz sampling frequency and 16 bits per word, this yields 2.688 Mbps for the vectors and 0.864 Mbps for the siderostat positions. Obviously, only the siderostat positions should be transmitted to reduce the overall data rate and/or storage requirements. Since the metrology system determines only the change in relative position between two points for all the points of interest, it needs to find three relative measurements for each position. This should be sufficient information

for setting up a system of linear equations to solve for the siderostat and IMU positions in three-dimensional space, a relatively simple computer operation.

Though the pixel data is essentially unchanged by the processor, the output data rate will be that of the average data rate, rather than the peak rate described above. By using a buffer, the processor should be able to establish a fairly constant output data rate from the discontinuous CCD data. Therefore, it is assumed that there will be 1.98 Mbps output due to the CCD's. The science mission requires only the eight science pathlengths, so only these will be released to the transmitter, but the two FGI pathlengths will be passed to the structural control processor along with the raw metrology data. The total data and data rates passed from the science data processor are summarized in Table 3-6.

Table 3-6 Science Data Processor Inputs and Outputs

Destination	Data Rate (Mbps)	Total Data Per Image (Gbit)	Data Components
Communications Processor	3.1	145.1	Average CCD data Processed metrology data (vectors) Eight pathlengths
Structural Control Processor	1.38	18.72	Raw metrology data Ten pathlengths

With this large amount of image information, the science data processor should utilize some sort of data compression scheme. It is therefore assumed that the baseline and pathlength data are compressed such that 16 bits are required for the first data point, and 4 bits for each point thereafter to denote the change in value rather than the value itself. The CCD data will be assumed to undergo a similar, though not identical compression that reduces the volume by a factor of 4. Image compression factors of about 3-10 can usually be achieved by schemes such as labeling and transmitting data only from pixels with

Table 3-7 Compressed Data Volumes and Rates for Transmission

Data Type	Data Rate (kbps)	Data Per Image (Gbit)
CCD Data	495	23.10
Pathlengths	64	3.00
Baselines	216	10.12
Total	775	36.22

significant information; therefore, a compression factor of 4 is a fairly conservative estimate. The compressed data that is then passed by the payload processor to the communications processor for transmission is shown in Table 3-7.

The science data processor must accomplish the following tasks:

- Receive raw data from the CCD's, the metrology system, and pathlength measurements at an average rate of 3.356 Mbps and a peak rate of 4.498 Mbps.
- Buffer CCD input such that a constant output data rate is achieved.
- Process raw metrology data to derive siderostat and IMU positions over time. This involves solving a system of linear equations.
- Pass the raw metrology and pathlength data to the structural control processor at a constant data rate of 1.38 Mbps.
- Compress science data (CCD's, 8 siderostat positions, 8 pathlengths).
- Pass processed and compressed science data to the MMU for storage, and later transmission. This occurs at a rate of 775 kbps for a total of 36.22 Gbit per image.

The data storage requirements are determined largely by the transmission schedule detailed in the communications section. In this case, the science data is assumed to be dumped once per orbit with a maximum transmission time of 20 minutes. For the baseline mission of 13 hours, just under eight orbits occur over the data taking phase. By dividing the total data per image by the eight orbits, a data transmission capacity of about 4.5 Gbit per orbit is derived. If, on the other hand, the target has to be much brighter than the 15th magnitude specified for the baseline mission, the data period could be considerably shorter. With the maximum spacecraft rotation rate of 90° in 75 minutes, the minimum science period is 2.5 hours, or about 1.5 orbits. Rounding this up to two orbits leads to a minimum capacity of 12.3 Gbit in order to meet the storage requirements of all possible targets.

Executive Controller: The last processing category that needs to be addressed is that for the executive direction of the operating system, input/output, and utility functions. The executive controller is sized mainly by the total number of tasks per second and the total amount of data per second handled by the entire C&DH system. This should obviously lead to fairly large demands for processing speed. The details of this are covered in Appendix B, and the total requirements are 48 K operating memory and 6 MIPS throughput.

3.2.2 System Architecture

Now that the elaborate process of determining the system processing requirements is finished, a system architecture that both meets the system needs and provides high reliability can be derived. The total processing and memory requirements for the first four computing categories are 20.32 MIPS and 231 K. The eight pathlength control devices require about 66 K and 1.8 MIPS each., and the science processing requirements are 13.2 Gbit memory storage and about 15 MIPS throughput [23]. The system executive requires 48 K memory and 6 MIPS throughput. There are several concepts in data systems design that allow for task sharing and high reliability computing systems. The centralized approach allows a single large processor to handle all of the processing tasks on the spacecraft. This is not a very attractive option because it establishes a mechanism for single point failure of the system, although this weakness can be mitigated by adding a redundant CPU. The centralized approach also does not work very well for systems with large processing requirements. The distributed approach uses a number of smaller processors, either attached to a common data bus with a central executive, or even distributed to different locations to accomplish localized tasks.

The interferometer uses a combination of both methods of distributed design. Dedicated processors are used for the science processing and for the PCD controllers, both because of their localized functions, and because of their relatively large processing requirements. A common data bus with several smaller processors makes up the rest of the system. For redundancy, a dual data bus with dual executive units is used to connect all processing units and storage devices on board the spacecraft. To handle the 20.32 MIPS

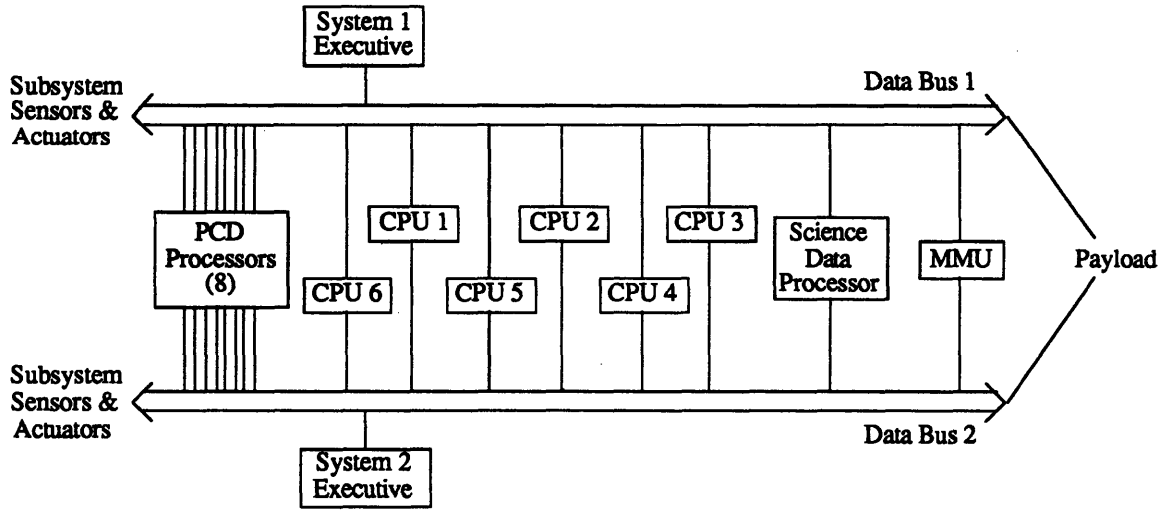

Figure 3-3 Schematic of C & DH Network

worth of processing required by the basic spacecraft systems, six processors of approximately 5 MIPS each are attached to the data bus. This provides about a 48% design margin in capacity, and allows for the failure of up to two of the units before system performance is seriously affected. None of these six processors are dedicated to any particular task, but each is directed to accomplish what is necessary by the dual executive systems. Figure 3-3 shows a schematic of the interferometer's C&DH system which illustrates the function and interaction of the components.

3.2.3 Hardware Specifications and System Summary

Using data from both [23] and [39], mass, power, and volume for the system can be estimated. Most of the useful processors described in the references are still under development for space qualified purposes. Table 3-8 summarizes the parameters for the processors selected for the system. Present forms of mass data storage are transitioning from tape recorders to solid-state recorders. Currently, only tape recorders have the very large volume required for scientific missions, but they are relatively heavy, and they produce mechanical vibrations. However, undergoing development and test are solid-state recorders that use a three-dimensional technique for chip packaging. The result has been recorders with large capacity, but small mass and power requirements [35]. In addition, these recorders produce no mechanical noise that will affect the payload. Table 3-8 also lists data for the solid-state recorder described in [35], sized to give 13.2 Gbit worth of data storage.

Table 3-8 Interferometer Processor and Data Storage Components

Processor	Mass (kg)	Ave. Power (W)	Pk. Power (W)	Volume (cm^3)	Estimate Source
Executives	22	15	60	8800	2 x IBM GVSC
Bus Processors	66	45	180	26400	6 x IBM GVSC
PCD Controllers	40	56	140	36800	8 x JPL OSI
Science	34	45	120	13200	3 x HI GVSC
MMU	2.5	15.4	15.4	1804	TI SSR
Total	164.5	176.4	515.4	87004	

3.3 Communications Subsystem

The communications subsystem is the spacecraft's link with the users and operators. It must consistently provide information to the operators about its status and receive commands from them for targeting and error correction. It must also pass on the huge amounts of data collected by the payload to astronomers on the ground for evaluation. The approach taken in designing the communications subsystem is to define the requirements for the system capacity and performance, and then conduct a series of trades to arrive at an acceptable system. The system design is driven mainly by the very large capacity of science data that needs to be transmitted, but it should be remembered that it is also desirable to minimize any vibrational disturbances. The trades considered in this section include decisions on the system architecture, the frequency band, the type and positions of antennas, antenna aperture vs. transmitter power, and the type of power amplifier.

3.3.1 Requirements Definition

From the previous discussion of the command and data handling subsystem, the interferometer science data storage requirement is known to be up to 36 Gbit per image. To determine the capacity of the communication system, the rate at which this data is transmitted must also be specified. However, the data rate is a parameter that is left free to vary in the design process. As a guideline for maximizing the efficiency of the system, it is assumed that the data is transmitted during the science collection mode approximately once per orbit. The baseline mission is expected to take approximately thirteen hours to complete, or just under eight orbits. This gives an average data transmission rate of 4.5 Gbit per orbit. Another guideline for the desired rate of transmission is the capacity of other components of the communications system, particularly the receiving station. If a dedicated ground station is assumed, the interferometer's share of its capacity is obviously 100%, and this constraint is removed. On the other hand, if it shares time on a multi-user system, such as TDRSS, its consumption of system capacity should be kept to a reasonable level. As will soon be described, the interferometer uses the TDRSS system, and therefore, it is specified that no more than 10% of TDRSS capacity should be used.

Finally, some measure of the performance of the link must be specified, and the standard measure of this is the bit error rate (BER). The TDRSS User's Guide [24] uses 10^{-5} as a standard example of link BER. Other space interferometer programs, however, have specified 10^{-6} [23]. Since the additional power required to transmit at 10^{-6} is only about 10 W, a BER of 10^{-6} is specified for this system as well. The communications

subsystem requirements are then concisely stated as: transmit up to 36 Gbit within thirteen hours, using less than 10% of any shared system capacity, at a bit error rate of 10^{-6}.

3.3.2 System Architecture

This particular trade is a rather simple choice between a cross-link to a system such as TDRSS and a direct ground link to a dedicated receiving station. The option of a dedicated ground receiver is quickly at a disadvantage on the basis of additional costs, but the performance parameters should be examined as well before rejecting it outright. An important parameter to consider in this respect is the view time, which has a large impact on mission flexibility. If a single dedicated ground station with a 120° field of view is considered, then the spacecraft is visible for only one third of its orbit while passing overhead. In addition there is a period of four hours out of every twelve when the satellite remains out of sight. When considering this, it is apparent that one could end up in a situation at the end of a data taking run where the satellite will be out of sight, and therefore useless, for the next three to four hours. In fact the total availability of a single ground station to the interferometer is only about 22%. Even if three receiving stations were positioned at 120° separations around the earth (with commensurate costs), the satellite would still remain out of sight 33% of the time. TDRSS, on the other hand, is available to the satellite a *minimum* of about 96% of the time. The maximum time it will be out of sight is for two 15 minute periods every 12 hours. It is fairly clear that TDRSS will give a much greater view time with no new construction costs, and is therefore the better choice.

3.3.3 Subsystem Component Design Trades

Antenna Type: The trade considered here is whether to use a standard gimbaled parabolic dish or a phased array antenna. The important parameters to the trade are vibration and dynamics, mass, cost, and reliability. Vibration, dynamics, and reliability all favor the phased array system. It has already been stipulated that in the interests of mission efficiency, data will be transmitted during the science mode, which requires tracking TDRSS with the antenna. The gimbaled system can only do this with mechanical actuation which will transmit vibrational disturbances to the payload. The phased array antenna can track TDRSS, and even switch quickly from TDRS East to TDRS West, by electronically steering its main lobe, requiring no mechanical actuation. More importantly, a parabolic dish must be positioned out away from the spacecraft body, which results in dynamical interaction with the truss structure. The phased array antenna can be mounted as a plate in

the trusswork, which actually enhances the structural performance by stiffening the location. A parabolic dish also needs to be deployed, which inherently reduces its reliability (e.g., GRO and Galileo). Since the phased array antenna is made up of several elements working in concert, it is possible for individual elements to fail without significantly affecting performance of the whole. This allows a graceful degradation in the system with any equipment failures. The phased array antenna is also space qualified, with one antenna being flown on each TDRS. The performance of a parabolic dish can be severely affected by any failure in its feed system or in its gimbaling mechanism.

The parameters of cost and mass both favor the parabolic dish. A phased array system is an inherently heavier system due to its greater concentration of electronics. In order to compare the two options, the phased array is assumed to have twice the mass per area of a parabolic dish (16 kg/m^2 from [39]). This is probably a conservative estimate in favor of the parabolic dish if one considers the additional mass that might be necessary to isolate the gimbaling disturbances from the payload. For the maximum phased array antenna diameter of 0.97 m (as constrained by the geometry of the trusswork), the mass differential is only 5.9 kg per antenna, or 0.05% of the spacecraft mass. Even if three antennas are used (a maximum), this amounts to a mass differential of only 0.15% of the spacecraft, which is relatively insignificant. In terms of cost, the parabolic dish is a simpler system with much fewer electronic components. On the other hand, additional mechanical and electronic design will be needed to isolate vibrations due to a gimbaled dish. Since both structural dynamic and reliability considerations strongly favor the phased array system, and since only cost strongly favors the parabolic dish, it seems that a phased array antenna would be the better choice for the interferometer.

Antenna Number and Position: The object of this trade is to establish the minimum number of antennas that are needed such that they have a view to TDRSS for sufficient time to transmit data during the science mode. A limit of less than 20 minutes per orbit is placed on the system so that only a reasonable amount of TDRSS capacity is used. Figure 3-4 shows the orientation of the interferometer orbit with respect to the sun, the earth, and the TDRSS satellites. Since the interferometer is in a twilight orbit, the orbital plane will always be perpendicular to the sun-earth vector. Science viewing is restricted to the hemisphere facing away from the sun, with the "excluded viewing directions" becoming available as the earth revolves about the sun. TDRSS consists of two satellites in geosynchronous orbit at 41 and 171 degrees west longitude, resulting in an angular separation of 130°. With this configuration, TDRSS provides continuous coverage to LEO except for a small exclusion zone centered at 74° east longitude. The ground trace of the

exclusion zone for a satellite at 700 km altitude is an oval of approximately 20° longitude by 120° latitude. The size decreases with altitude up to 1200 km when full coverage becomes available. In the figure, the TDRSS satellites and the earth will rotate once per day with respect to the orbit. This geometry indicates that at least one TDRS will always be visible to the interferometer except for a maximum of twice each day when it passes through the no-coverage zone.

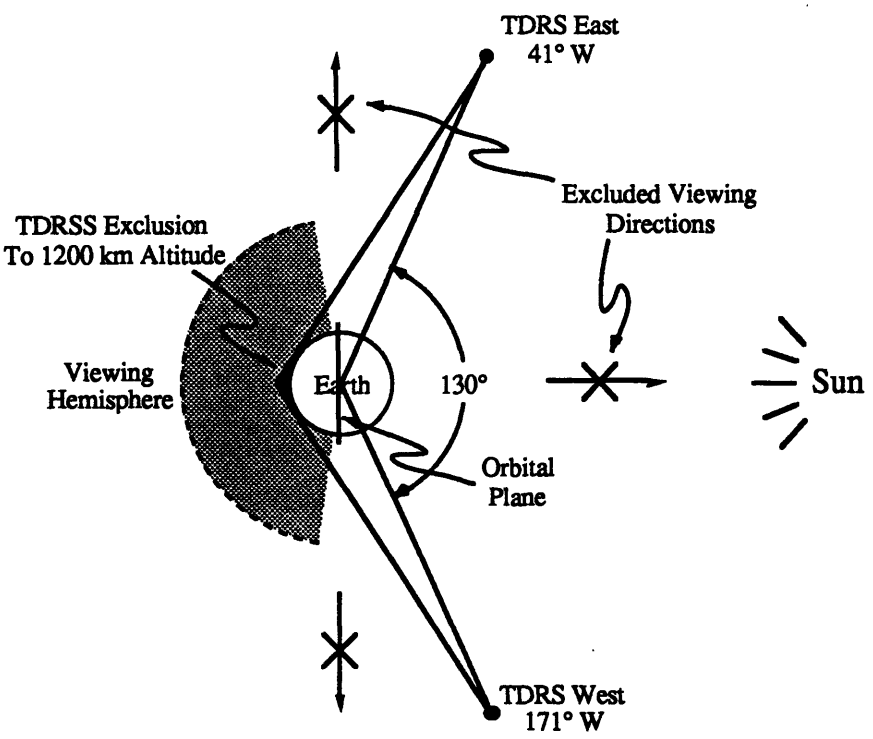

Figure 3-4 Interferometer-TDRSS Geometry

Since it has been established that the interferometer has a nearly continuous view of one or the other TDRS, it now needs to be determined how many antennas to use and where to place them. Positions should be selected that provide good coverage both during rotation about the LOS and for angles with respect to the LOS. A typical phased array antenna can provide a field of view of approximately ±60°, or a 120° cone. Since data is transmitted during the science mode, involving a rotation through 180° about the LOS, a single antenna is insufficient. The next obvious choice is to consider a pair of antennas. Note that the placement of these antennas is somewhat restricted. For example, the outside of the fourth vertex is unavailable since this is the position of the apogee kick motor, and the inside of the science plane legs is unavailable since it turns out to be the best position for the solar arrays. A good location is the outside faces of two of the science plane

vertices. The coverage provided from these positions is shown in Figure 3-5. In figure (a), the science plane is facing out of the page, and one can see that the antennas will

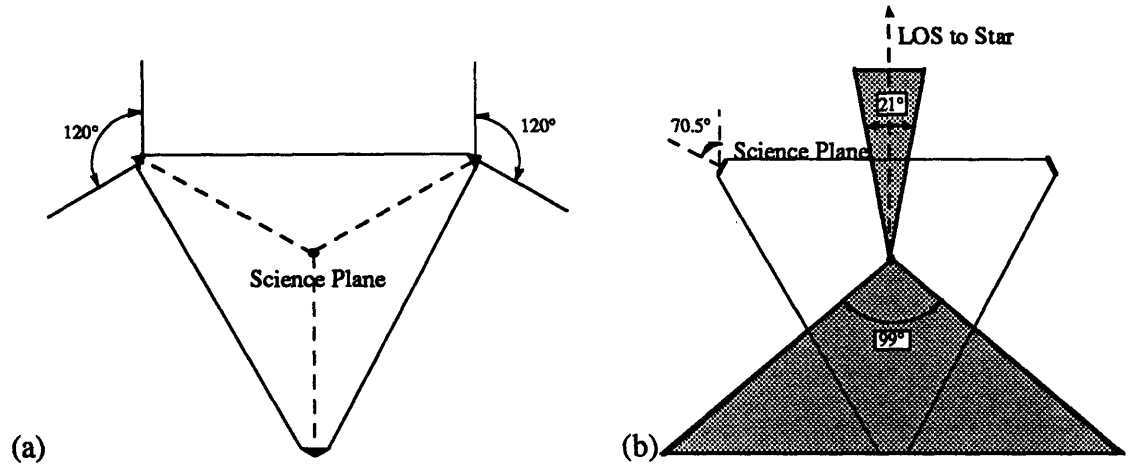

Figure 3-5 Antenna Viewing Geometry

provide approximately 240° coverage about the LOS vector. Since the starting point of the LOS rotation is arbitrary, it can be initiated such that a TDRS always falls within this field of view. In figure (b), the side of the interferometer is showing with the LOS pointing to the top of the page. Zones that are not in view of the antennas are shaded. The outside faces of the vertices are at 70.5° from the science plane, leaving a gap of at least 21° along the LOS and 99° through the fourth vertex.

To determine if this coverage is sufficient, examine the Figure 3-4 in relation to the two extreme cases in spacecraft pointing. The first case is where the interferometer's LOS points into or out-of the page along the north-south axis of the earth. This proves to be an easy case since even with the interferometer over the pole, the angle formed between the science plane and the TDRSS orbital plane is only 9.5°. Thus, provided the LOS rotation is initiated from the proper position, a single TDRS will be within view for at least half an orbit throughout the science mode. The second case is where the interferometer's LOS is pointing along the sun-earth vector. The worst possible arrangement for this case occurs once each day when TDRS East also lies on this vector and the interferometer is on the far side of earth from TDRS West. In this configuration, TDRS East is in the forward shadow zone of the antennas. By the time the interferometer goes through half an orbit, both TDRS East and TDRS West have progressed 12.4° with respect to the interferometer orbit. This leaves TDRS East still in the forward shadow zone while TDRS West has moved into the rearward shadow zone. But after only another half-orbit , TDRS East will have cleared the

forward zone, and there should be no further problems for the rest of the day. If an effort is made to time this particular position with the time when the interferometer is reorienting itself to a new target, it should not prove to be a significant problem. From this analysis it can be concluded that two antennas placed on the outside faces of the science plane vertices provide adequate coverage during the mission.

Frequency Band: Since the interferometer uses TDRSS for communications, there is a choice of three link services: S-band multi-access (MA), S-band single access (SSA), and Ku-band single access (KSA). The multi-access services can support up to 20 simultaneous users with return-link data rates up to 50 kbps. Recalling that the expected data volume can reach 36 Gbit, the MA service would require *8.3 days* to transmit the information from a single image. Clearly, this is unacceptable, and the remaining choice is between the SSA and KSA services. The important parameters in this trade are mass, power, and transmission time.

This trade can be quickly evaluated by examining the capacities of the two systems. The SSA service operates at 2.2875 GHz and can accept a maximum data rate of 6 Mbps. The KSA service, operating at 15.003 GHz, will accept data rates up to 300 Mbps. If we assume a worst case antenna steering angle of 60°, then the time required to transmit a full image at the maximum SSA data rate is 100 minutes, or 12.5 minutes per orbit. This is about 6.3% of the total TDRSS SSA capacity. Recalling that no more than 10% of any single access capability should be used, an SSA system would have to operate at better than half of its capacity, suggesting that the KSA system may actually be better.

To address this a little more directly, the two frequency bands are compared by specifying the maximum allowable transmission time to be 25 minutes per orbit (~10% of capacity) and then calculating the required mass and power for each. Assuming the maximum range to TDRS of 44748 km, a link margin of 6 dB, and the use of solid-state power amplifiers, the required input power is 25 W for the KSA and 182 W for the SSA. The total system mass, including amplifiers, antennas, and transponders, is 36 kg for the KSA and 53 kg for the SSA. The details of this link calculation are described in Appendix C. With this analysis, it is fairly obvious that the TDRSS KSA service is the superior choice.

Antenna Aperture vs. Transmitter Power: A classic trade in designing a space communications system is increasing antenna aperture in order to maximize gain and minimize transmitter power at the expense of additional mass. Figure 3-6 plots communications system mass in kilograms and input power to the amplifier in Watts versus

antenna diameter for a system using solid-state amplifiers and for one using a travelling wave tube amplifier (TWTA). The calculations were made assuming KSA service at a maximum data rate of 16 Mbps. Due to the rapid increase in required power below about 80 cm diameter, it is fairly obvious that an antenna larger than this is desirable. Unfortunately, the antenna diameter is constrained at the upper end of the scale by the dimensions of the interferometer trusswork. With a 1.68 m nominal strut length, the maximum diameter that will fit at the outside face of a vertex is 97 cm. This is the antenna size chosen for the system, and it results in a system requiring 9.6 W transmitter power and a total system mass of 51 kg.

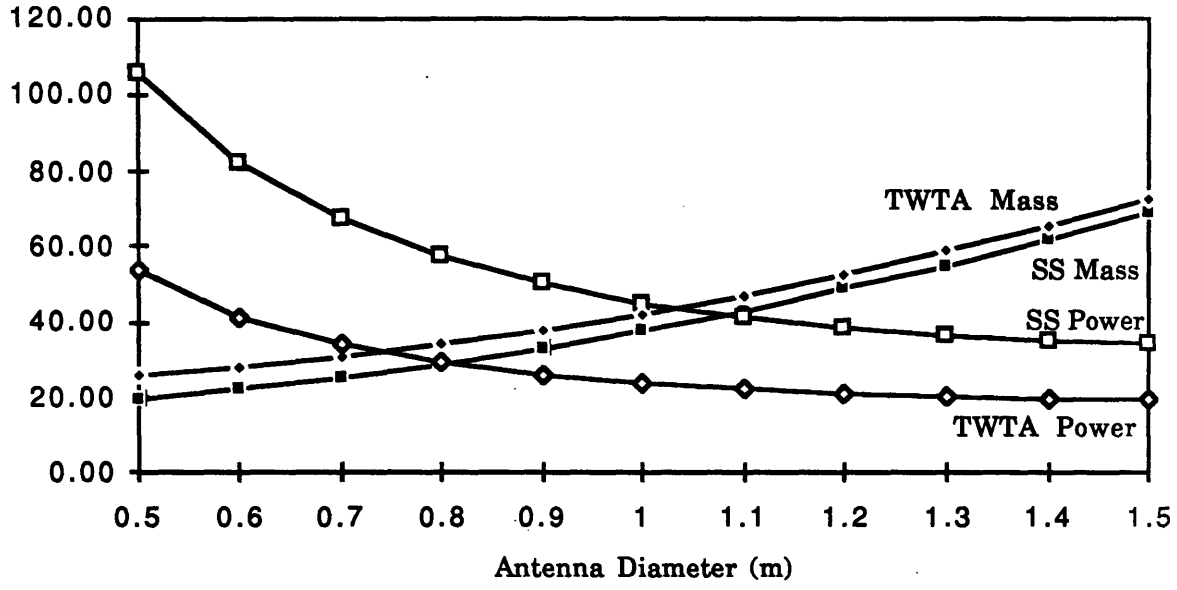

Figure 3-6 Variation of System Mass (kg) and Power (W) with Antenna Diameter

Amplifier Type: The last design trade considered is whether to use a TWTA or solid-state amplifiers. The above figure rather clearly favors TWTA's since they give a savings of about 20 W input power at the expense of only 4.5 kg mass, but the figure does not address the driving factor in amplifier selection: reliability. Solid-state amplifiers hold a significant advantage in reliability in that they are made up of a set of relatively small (and low power) components. Similar to the trade of a phased array antenna versus a gimbaled parabolic dish, a solid-state architecture allows for the failure of a few individual elements without significantly affecting the performance of the whole. TWTA's function as a single

element and require additional electronics to provide operating voltages on the order of ten thousand. The reasons TWTA's have historically been chosen are their efficiency, and mainly, the fact that solid-state amplifiers have not been able to provide adequate power levels until recently. The solid-state amplifier architecture, however, provides a means of graceful degradation in system performance over the mission lifetime and eliminates a mechanism for catastrophic single point failures. Since the enhanced reliability of a solid-state system is obviously of great value, TWTA power savings on the order of only 1% of the total system power seem insignificant. For these reasons, solid-state amplifiers are chosen for the system.

3.3.4 Link Calculations and Performance Summary

This section summarizes the important link performance parameters. The details of the computations involved in the link analyses can be found in Appendix C. The main design parameter used in the analyses is the transmission time. A total data volume of 36 Gbit over the length of approximately eight orbits gives a data rate of 4.5 Gbit per orbit. By setting the allowable transmission time per orbit, the data rate in bits per second is determined. Calculations are made for both minimum and maximum antenna steering angles and for minimum and maximum ranges to TDRS. In all calculations, a link margin of 6 dB is assumed.

The nominal system performance is set by assuming an acceptable worst case (antenna angle and range) transmission time of about 20 minutes per orbit, or only 6.7% of TDRSS capacity at 3.75 Mbps. To transmit at this rate requires a transmitter power of 4.5 W and an amplifier input power of 27.7 W. Solid-state amplifiers are very insensitive to power level up to an output power of about 40 W, well beyond the expected operating range of this system [39]. To add additional redundancy, then, at the cost of only about 3 kg, two amplifiers of five units each are included for the two antennas. Since each unit supplies about 2 W power, up to two of the units in each amplifier may fail without significantly affecting performance. The additional amplifiers also give a level of flexibility in transmission capability, with transmitter power up to 10 W. Figure 3-7 shows amplifier input power for a range of maximum transmission times. Note that this incorporates the efficiency of the amplifier. The corresponding transmitter power runs from 9.0 W for 10 minutes down to 1.5 W at 60 minutes, meaning the whole range is well within system capacity. For reference, the corresponding minimum transmission times (for steering angle of zero degrees) are 5 to 30 minutes.

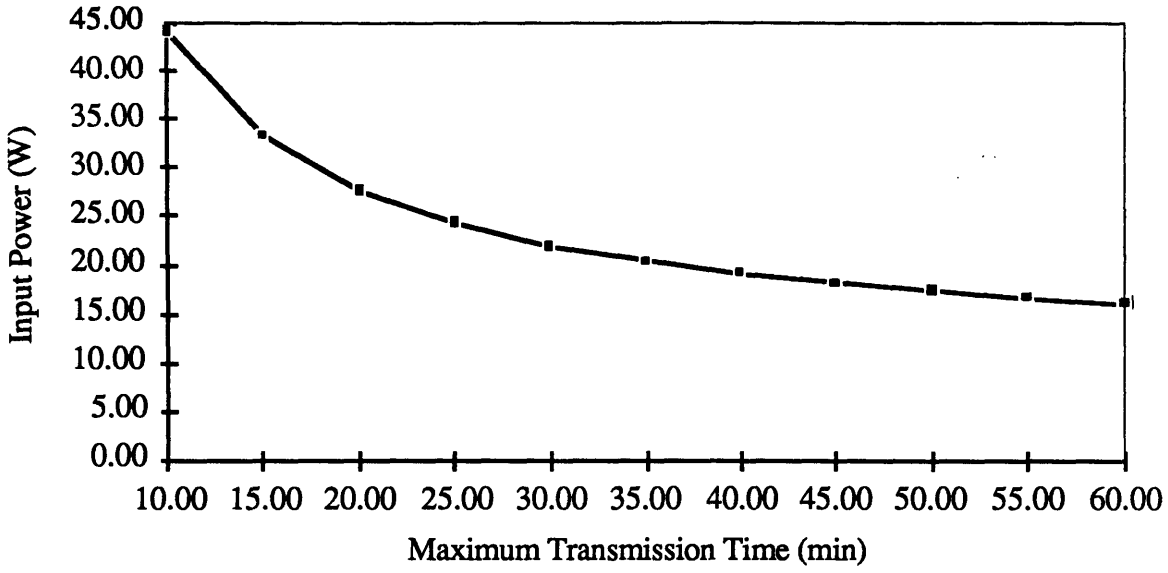

Figure 3-7 Required Amplifier Power as Function of Maximum Transmission Time

An additional calculation is made for an omni antenna. This is the antenna that is used during deployment and emergencies as well as to transmit general housekeeping telemetry. If two perpendicular biconical-horn antennas are assumed, the antenna pattern is a pair of perpendicular toruses, with the worst case gain of about 0 dB. In order to minimize system complexity, these antennas also operate at Ku-band where the minimum TDRSS data rate is 1 kbps. Using this value for the minimum data rate, and still assuming a link margin of 6 dB, the power required from the system is only 5.6 W, well within the system parameters.

Figure 3-7 clearly demonstrates the effect of power on transmission time performance, but the effects of several other parameters have not been addressed. Antenna steering angle, antenna diameter, and antenna pointing error can all have a strong influence on the link performance. The main influence of the antenna steering angle is on the antenna gain, or more specifically the effective area of the antenna. Steering the beam off the main axis reduces the effective antenna area by a factor of the cosine of the angle. This has a direct impact on the achievable data rate, hence, the maximum steering angle of 60° reduces the transmission time performance by a factor of 0.5. Figure 3-6 showed the relationship of antenna diameter to system mass and power, but its roughly quadratic effect on data rate performance can be deduced from the influence on antenna area, and therefore, antenna gain. The impact of pointing error is important only when it becomes a significant fraction of the beamwidth, which decreases with both frequency and antenna diameter. The 3 dB

beamwidth for the KSA phased array antenna is 1.47°. This suggests that the pointing error should be kept well under one degree. An error 0.5° is assumed in all link calculations, which should be no problem for a spacecraft that is required to point at a star within 0.01 arc-sec.

The last point to address in the component design is the construction of the phased array antennas. As already mentioned, a phased array is made up of a large number of individual elements. The size and number of these elements is dependent on the operating frequency of the antenna. The maximum spacing that can be tolerated between elements without aliasing is one-half of the wavelength. At 15.0034 GHz, the wavelength is approximately 2 cm. This implies an element spacing of about 1 cm. If an octagonal panel with maximum crosswise dimension of 0.97 m is assumed for the array, then the minimum element count per array is 7609. The minimum number of elements required for the system then, is 15,218. This large number of array elements presents a strong case for using a space-fed array rather than a distributed feed. In the distributed feed, each element is connected with the main feed by its own cable, which for arrays with a large number of elements can lead to considerable cabling mass and complexity. With a space-fed array,

Table 3-9 Communications Subsystem Component Mass and Power

Component	Number	Mass (kg)	Power (W)
Low Gain Omni Antennas	2	3	-
Phased Array Antennas	2	23.6	-
Transponder &Electronics	2	10.3	30
Power Amplifiers	2	2.5	28
Coax Cabling		11.25	-
Total		50.7	58

each element is fed across a vacuum by a main feed horn. This eliminates the complex wiring, but retains the possibility of a single point failure in the feed horn.

Table 3-9 summarizes the mass and power requirements for the communications subsystem. Note that even with the use of heavier phased array antennas, the subsystem mass is rather small, at roughly 0.5 % of the spacecraft mass. The data for the transponders and cabling are taken from [39], assuming a NASA standard TDRSS equipment.

3.4 Power Subsystem

The power subsystem is responsible for producing and delivering electrical power to the system components at an adequate level throughout the spacecraft lifetime. The primary drivers of the power system are the mission lifetime, the orbit, and the magnitude and time profile of the electrical loads. For the interferometer, the mission lifetime is specified at 10 years, and the orbit is a twilight sun-synchronous orbit at 700 km altitude. There are two main implications of the twilight orbit for the power system: 1) the orbit about the terminator means that the spacecraft is usually in sunlight with short eclipse periods once per year, and 2) the orbit is polar, which means a more severe radiation environment. The spacecraft mass and power listing in Appendix A gives a summary of the power requirements. From the appendix, a steady-state load of 1980 W and a peak load of 3500 W at end-of-life (EOL) are required. The large majority of the peak load (~60%) is due to the attitude control actuators reacting to environmental torques that occur sinusoidally at the frequency of the orbit. Thus, the power system will have to deliver the full peak load once every 98 minutes.

The main trades addressed for this subsystem have to do with how to configure the system, where to position the solar arrays, and what type of cells to use. The configuration of the system influences how the large differential between the average and peak loads is covered and how the power distribution and control affect the system reliability. The main considerations in these trades will be system mass, dynamic interaction, and reliability.

3.4.1 System Architecture

For a spacecraft power system delivering 3.5 kW in low earth orbit, the only energy conversion mechanism that makes real sense is solar photovoltaic. Primary batteries and fuel cells have insufficient lifetime, and nuclear sources are politically unacceptable in LEO for power levels within range of solar systems. Solar thermal-dynamic systems are feasible, but they require advanced development and necessitate dynamic interaction with the structure during the science mode. Solar photovoltaic energy conversion is adequate for the interferometer's needs, and is a highly reliable and well proven technology.

In working out the power system architecture, one is immediately confronted with the problem of how to meet the additional 1.52 kW over the steady-state level demanded by the attitude control system. The orbit specifications indicate that the batteries will not usually be needed to cover eclipse periods; instead, their energy storage capacity could be used to handle the peak demand. In other words, the solar arrays would supply both the

steady-state demand plus the battery charging power. The batteries would cover the difference between the steady-state and peak demands. The peak demands can be considered to occur as a sine function at the orbital frequency of 98 minutes, since the majority of the peak power is taken by the RWA's counteracting the environmental torques. This means that the batteries go through a complete charge-discharge cycle once per orbit. If one assumes that the arrays produce 2740 W, and the batteries an additional 760 W, the required battery capacity is 47 Whrs. If only 49 minutes are allowed to recharge this capacity at 0.9 efficiency, the required charging power is calculated as

$$P_{ch} = \frac{Pt_{dis}}{t\eta} = 64 \text{ W} \qquad \text{Eq. (3-15)}$$

where Pt_{dis} is the capacity. This power, added to the minimum steady-state power of 2740 W, gives a total array power of 2805 W. At first glance, this architecture seems to be quite attractive, but the analysis does not take battery lifetime into consideration. For battery discharge once per orbit, the battery lifetime must be about 53,700 cycles, whereas for the architecture in which the batteries must cover only eclipse periods, the lifetime is only about 12,600 cycles. This difference translates into a change in the allowable depth of discharge from 30% to 50%. This results in a change of approximately 4 kg per cell in battery mass, for a total increase of 108 kg. As described later, the specific power of the solar arrays at EOL is 123 W/kg. If arrays are required to cover the full 3500 W of peak power, the mass increase is only about 5.7 kg. In the end result, using batteries to cover the large peak-average differential costs an additional 100 kg without reducing complexity or adding redundancy. Considering this, the assumed system architecture will be solar arrays providing the peak EOL power of 3500 W, and batteries relegated to the role of supplying deployment and emergency power, as well as eclipse loads. The details of the power control and distribution will be addressed later in section 3.4.4.

3.4.2 Solar Array Design

In the interests of using a very low mass solar array, the design will assume performance data from the Advanced Photovoltaic Solar Array (APSA) program [18]. This program involves the development and test of an ultra-lightweight, flexible blanket fold-out array giving performance of about 138 W/kg specific power at BOL. Since the interferometer may use body mounted arrays, the mass of most of the deployment and support structure can be disregarded. Including a 10% design margin, this yields specific powers of 223 W/kg and 140 W/m^2 at BOL. The array cell choice, discussed in more detail below,

is for 2 x 5.7 cm silicon (Si) cells at 50 μm thickness. The substrate is 50 μm germanium coated Kapton, and the cover glass is 50 μm ceria-doped glass with ultra-violette and anti-reflective coatings. Much more detail on the design and construction of these arrays is given in the reference.

The choice of solar cell material is generally limited by current technology to either silicon or gallium-arsenide (GaAs). Si has been the standard cell because of its long history of reliable use and its relatively low cost. GaAs is attractive because of its higher inherent efficiency and better radiation hardness. The drawbacks to GaAs are that it is more dense, it cannot be manufactured as thinly, and it costs approximately six times as much as Si. The conclusion reached in the APSA study is that in producing a very lightweight design, a primary driver is the thickness of the array. Since Si is less dense and can be cut at about half the thickness of GaAs, the overall specific power performance is approximately the same. For an array in the interferometer's power range, GaAs provides a specific power advantage of only about 2 W/kg at EOL. This results in a difference in total mass of less than 3 kg. This tiny mass savings is clearly insufficient to justify the much greater expense of GaAs. Currently, the high cost of GaAs will probably limit its use to those missions where its efficiency and hardness make it a mission enabling technology.

The next step in solar array design is to estimate array losses over the mission lifetime. As a conservative estimate, 5% degradation due to installation errors and random cell failures is assumed. An additional 5% (~0.5% per year) is assumed for lifetime degradation due to such things as coverglass darkening and thermal cycling of the interconnects. 10% degradation will be assumed due to array temperature of approximately 50 °C (~0.5% per °C above 28), and radiation degradation due to the relatively high radiation environment of a polar orbit is assumed to be 2.5% per year, or 25% total. The resulting total estimated degradation is 45%. Note that APSA assumes a 33% degradation over 10 years in LEO, but stronger effects are assumed for the interferometer because of the polar orbit radiation environment and a somewhat higher operating temperature. 45% degradation in performance will give EOL specific performance of 123 W/kg and 77 W/m^2 for the APSA array. The corresponding BOL power requirements are then 3600 W steady-state and 6363 W peak, which requires 45.5 m^2 of effective illuminated area.

Array Type and Positioning: The main trade involving the interferometer array design is the positioning of the panels. The choice is between deployable, sun-tracking arrays and body-mounted arrays. The important parameters in this trade are the mass of the panels and their impact on the structural dynamics of the spacecraft. Sun-tracking arrays

will require smaller area due to their ability to remain normal to the sun, but will interact with the low frequency structural dynamics and would require mechanical actuation during the science mode. Body-mounted arrays require greater area due to shadowing and sun angle effects, but will actually enhance the structural dynamic performance by adding stiffness and/or damping to the truss legs. The real question becomes whether the savings in mass given by sun-tracking arrays is large enough to outweigh the dynamic complications. To investigate this trade, one must determine the mass of sun-tracking arrays, and then determine the best position for body-mounted arrays and their corresponding mass.

If APSA data is again used, the specific mass at BOL of a deployed array with a 0.1 Hz structure is 131.7 W/kg and 140 W/m^2. These numbers include a 10% mass margin. With two-axis control, the arrays are able to point at the sun from any spacecraft orientation if they are cantilevered from the truss legs (note this arrangement will interfere with the field of view of the Ku-band antennas). If 6363 W at BOL are needed, and a pointing accuracy of 30° is assumed, then the mass of the array is

$$A = \frac{6363\ W}{\left(140\ \frac{W}{kg}\right)\cos 30°} = 52.5\ m^2 \qquad \text{Eq. 3-16}$$

$$M_{ST} = \left(52.5\ m^2\right)\left(1.06\ \frac{kg}{m^2}\right) = 55.7\ kg \qquad \text{Eq. 3-17}$$

Note that with two-axis sun-tracking, there are large variations in the structural plant as the arrays change position during rotation about the line of sight. If it is decided to reduce plant variations by restricting sun-tracking to one axis only, an additional panel must be added to account for sun angle effects. This raises the array mass to 83.6 kg, and there will still be interference with the antenna field of view and strong coupling of the array dynamics with those of the truss. With these disadvantages, the mass savings of sun-tracking arrays will have to be quite significant to justify their use.

For body-mounted arrays, there are only two choices of location that provide enough area to generate the required power. The first option (A) places panels on the inside faces of the science plane legs. The second option (B) places them on the outside faces of the near legs. The science plane face is obviously unavailable since it is restricted from facing the sun. Comparing options A and B is rather difficult since the shadowing and sun angle varies so much depending of spacecraft orientation. Note that for either option, there must be enough area on each face for full power generation in the face of shadowing constraints. One easy way of comparing the two options is to set the areas

equal (thus equalizing the array masses) and examine which spacecraft orientations meet the EOL peak power requirements. For both options, the array area on each face is set at 53.7 m^2, the maximum available in option A. To account for possible shadowing by the near legs, the option A area used in the power calculations is reduced to 52.3 m^2. The unit normal vectors for each face can be easily calculated, and then the sun vector can be varied through all acceptable viewing orientations.

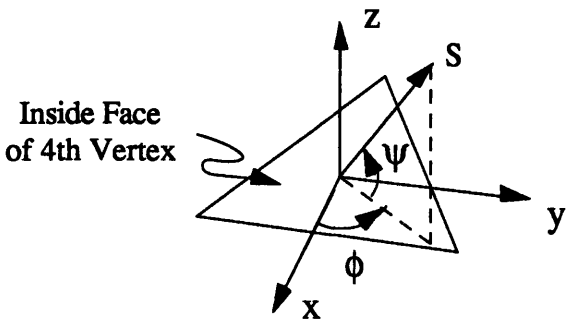

Figure 3-8 Definition of Sun Vector Orientations With Respect to the Spacecraft Coordinate Frame

The geometry is defined as shown in Figure 3-8. The origin of the coordinate system is set in the center of the inside face of the fourth vertex with the **z** direction pointing in the direction of the science plane and the **x** direction perpendicular to one side of the triangular face. The angle ϕ is measured in the **x-y** plane to the direction of the sun unit vector, **S**. The angle ψ is measured from the **x-y** plane towards **z**. Thus, **z** is in fact the interferometer line of sight, where $\psi = 90°$ and ϕ is undefined. When **S** is set such that $\psi = 90°$, the sun vector and the line of sight are parallel, and the interferometer is facing directly away from the sun. To get all acceptable sun angles, **S** is set for $\phi = 0 - 360°$ at 5° increments, and for each ϕ, $\psi = 0 - 90°$ in 5° increments. Note the for a set value of ψ, changing ϕ is the standard operating maneuver of rotation about the LOS.

From the dot product of the sun vector and the array normals, the sun angle with respect to each panel, θ, and the effective array area, A cos θ, can be determined. The maximum allowable θ is 70°, meaning that the effective area is set to zero for θ greater than this angle. The reason for this is that the power generated by a solar cell falls off with the cosine of the sun angle up to about 60°, and after 70°, is essentially useless. The total effective array area is the sum of the three effective face areas. The EOL power is the total effective area multiplied by the EOL specific power (77 W/m^2 at 45% degradation). If this is below the required peak power of 3500 W, the sun vector direction is marked in the plots of ϕ versus ψ in Figures 3-9 and 3-10.

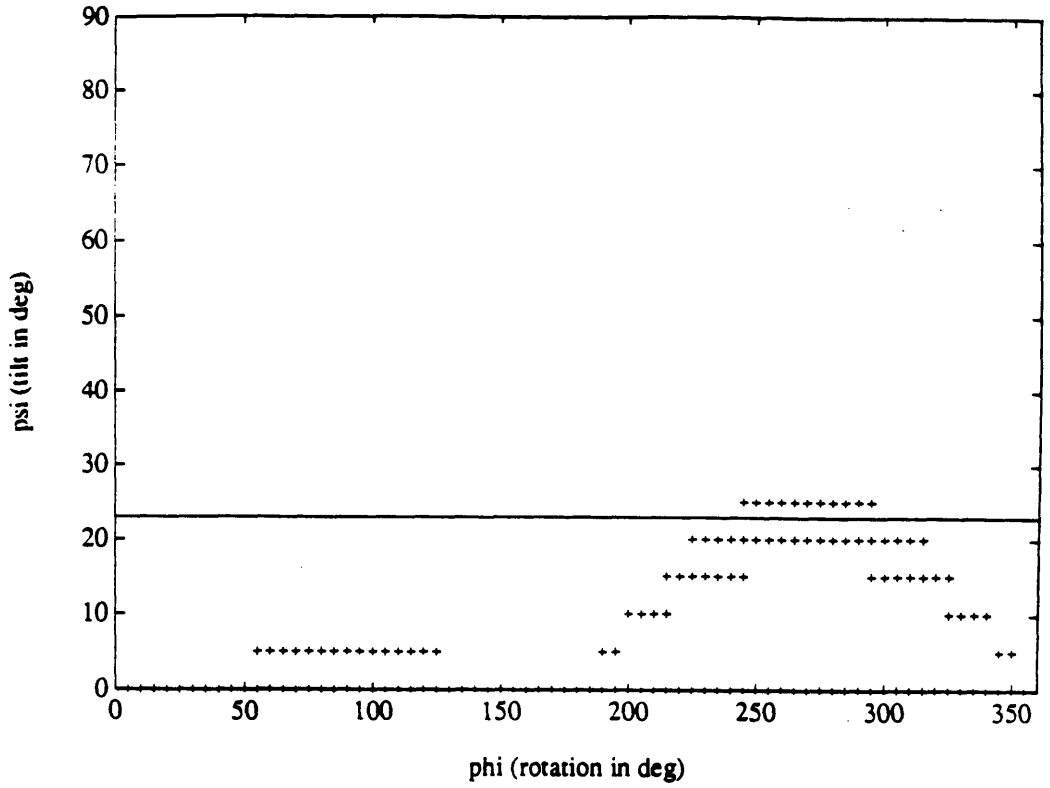

Figure 3-9 Positions Not Meeting 3500 W EOL Power for Array Option A

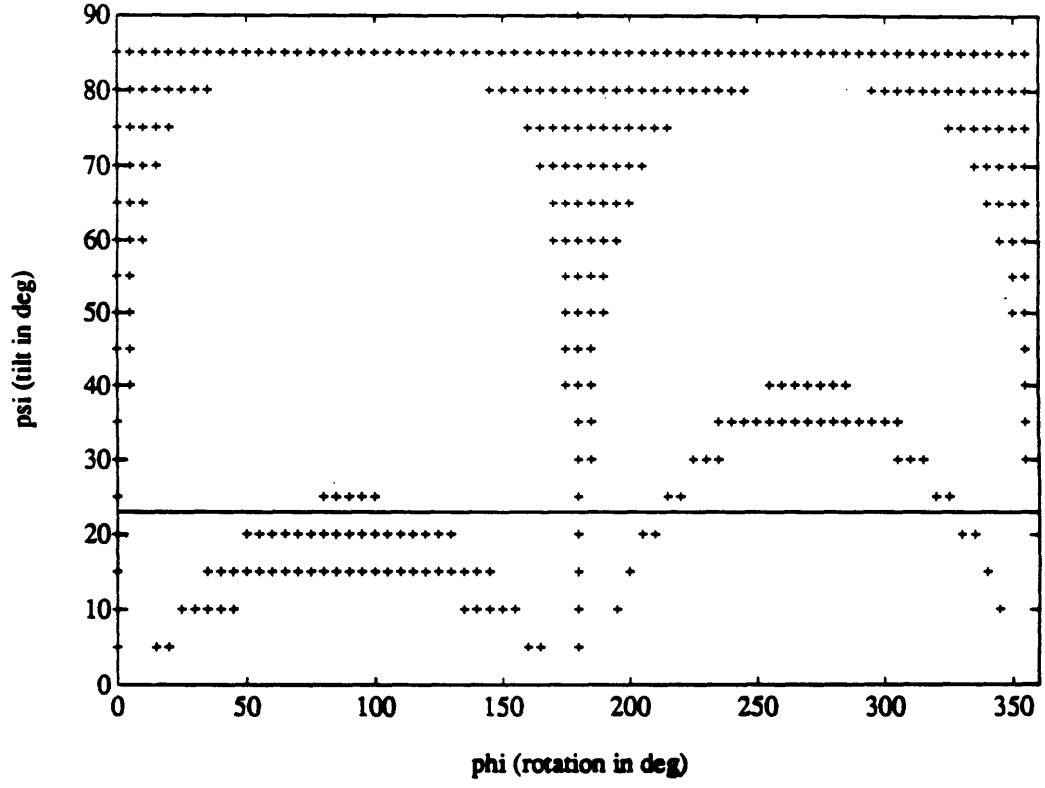

Figure 3-10 Positions Not Meeting 3500 W EOL Power for Array Option B

Figure 3-9 is for option A, and Figure 3-10 for option B. A comparison of the two rather clearly demonstrates that option A is the better choice, and the simple reason for this is that the sun angles for option B are frequently greater than 70°, especially as ϕ approaches 90°. The solid line on both plots marks the 23.4° tilt of the earth with respect to the plane of the ecliptic. The significance of this is that the interferometer does not have to tilt to angles less than 23.4° since the stellar regions within that angle of the poles can be explored by taking advantage of earth's tilt at the proper time of year. With option A, viewing may have to be restricted at EOL to areas more than 5° from the poles or power budgeting will have to be practiced such that sufficient power is available to run the attitude control and payload. Another option is to tap some of the emergency battery power to provide the additional 125 W that are needed to operate at extreme orientations. Due to generally larger sun angles, option B cannot provide sufficient power with only 53.7 m^2 of array area per face, but it is not constrained in total area as option A is. Option B can provide full power at all orientations with an array area of 65 m^2 per face, for a total mass difference of 21.3 kg.

Since it offers slightly lower mass and generally better operating conditions for the solar cells, option A is chosen over option B as the body-mounted configuration. For option A, the entire inside faces of the science plane legs are covered with solar panels for a total area of 161 m^2. With an APSA derived body-mounted specific mass of 0.627 kg/m^2,

Table 3-10 Comparison of Sun-Tracking and Body-Mounted Solar Arrays

Solar Array Configuration	Advantages	Disadvantages
Sun-Tracking	• Mass savings of 45.3 kg • Lower operating temperature	• Additional deployment • Additional drag area • Strong dynamic coupling with truss structure • Changing structural plant • Mechanical actuation during science mode • Limits antenna field of view
Body-Mounted	• Added stiffness/damping enhances dynamics • No additional deployment • No additional drag area • No actuation • No field of view limitations	• Additional mass • May require cooling

the total array mass is 101 kg. The last step in deciding on the array positioning is to compare the sun-tracking and body-mounted options. The main advantages and disadvantages of each choice are summarized in Table 3-10.

The sun-tracking array has only two advantages. Since one side of a sun-tracking array has an unobstructed view of deep space, it will tend to have a lower operating temperature than the body-mounted array, which will have a somewhat obstructed view. The lower operating temperature leads to a higher efficiency in the power conversion process, and this has been taken into account in estimating a minimum array temperature of about 50 °C. The other advantage of a sun-tracking array is a savings of 45.3 kg, or less than one-half percent of the spacecraft mass. As previously discussed, these advantages carry with them rather severe implications for the structural dynamics. The fundamental frequency of the array is near that of the truss structure, which leads to strong interactions as the arrays are moved to track the sun. The changing of the position of the arrays implies a changing of the structural plant, which has implications for any control schemes used on the structure. In the face of these complications, a mass penalty of only 0.4% seems a small price to pay for an array configuration which actually enhances the structural performance. For these reasons, the interferometer uses body-mounted arrays on the inside surfaces of the science plane legs.

Array Design: Because there are orientations at which only one of the faces will be illuminated, each face must supply the power bus. In addition, it is desirable to avoid having array electrical connections across the deployment junctions of the science plane legs. For these reasons, the solar arrays are configured into 6 panels with two panels on each face connected to the power bus for regulation and distribution.

The power bus must supply 3500 W at EOL, implying that each panel must deliver about 1750 W. For the APSA solar cells, representative cell current and voltage are derived from the cell size and specific power. For the remaining analysis, the following cell characteristics are assumed:

$$I_{mp} = 0.347 \text{ A} \qquad V_{mp} = 0.46 \text{ V} \qquad @ 25 \text{ °C}$$

If standard EOL temperature coefficients of $\alpha_i = 0.0024$ A/°C and $\alpha_v = -0.0022$ V/°C are also assumed, the EOL cell voltage and current characteristics can be derived from the following equations [1]:

$$V_{cell} = [V_{mp} - \Delta V + \alpha_v(T - 25)]\, K_r \qquad \text{Eq. 3-18}$$

$$I_{cell} = [I_{mp} + \alpha_i(T - 25)]\, K_a\, K_d\, K_s \qquad \text{Eq. 3-19}$$

where, $\Delta V = 0.005$ V panel wiring loss; $K_a = 0.95$ assembly loss factor
$T = 50$ °C operating temperature; $K_d = 0.95$ environmental loss factor
$K_r = 0.75$ radiation loss factor; $K_s = \cos 35°$ solar incidence factor

Applying the above equations yields:

$$I_{cell} = 0.301 \text{ A} \qquad V_{cell} = 0.30 \text{ V}$$

From these characteristics, the number of cells required in series and parallel for each panel is determined. The total panel current is simply the panel power divided by the bus voltage. If a standard bus voltage of 30 ± 2.5 V is assumed, then the resulting panel current is 58.33 A. The number of cells in parallel is computed by

$$N_p = \frac{I_{panel}}{I_{cell}} \cong 194 \text{ cells} \qquad \text{Eq. 3-20}$$

If voltage drops of 0.9 V for both the panel blocking diode and the wiring harness are assumed, the required number of cells in series is

$$N_s = \frac{V_{bus}+V_{drop}}{V_{cell}} \cong 107 \text{ cells} \qquad \text{Eq. 3-21}$$

This gives a total count of 20,758 cells per panel, and 124,548 cells for the entire spacecraft. The total voltage per panel is 30.3 V, and total current per panel is 58.39 A. This gives a power per panel of 1769 W, and a total power at worst case orientation of 3538 W for a power margin of 38 W.

3.4.3 Energy Storage Design

Although the interferometer's orbit seems to minimize the need for batteries during eclipses, they are also needed to provide power during deployment and initial sun acquisition, and later, for emergency use. In order to size the components, we need to determine the power requirements for these two phases, and for the eclipse periods. The energy requirements for the eclipse period can be found by integrating the power demand over the 14.75 minute average eclipse period. By assuming the eclipse period is centered on the time of peak power demand, the energy requirement is computed as

$$Pt_{dis} = P_{pk} \int \sin\left(2\pi \frac{t_{ave}}{P}\right) dt + P_{ave} t_{ave} \qquad \text{Eq. 3-22}$$

where P_{pk} is the peak-average power differential of 1520 W, P is the period of the orbit, and P_{ave} is the steady-state power of 1980 W. The energy required is then 510 W·hrs, which it turns out is considerably smaller than that required for deployment or emergency power. Equation 3-15 can be applied to determine the amount of power required to recharge the batteries. At a charging efficiency of 0.9, using the full 84 minutes of sunlight during each orbit, the power is 405 W, which if not drawn during peak demand, requires no additional solar array power.

For the launch and deployment phase, the batteries need to power the spacecraft during the transfer orbit, circularization burn, initial check-out, truss deployment, final check-out, and sun acquisition. Estimates of power levels and duration for each of these tasks are shown in Table 3-11. Batteries are also needed in the event of emergencies. This would entail some sort of array failure, or perhaps a major failure in some other system that required shutting down the entire spacecraft. It would seem reasonable to allow ground controllers up to one day's time to decide on a proper course of action before requiring the the system to be powered up. Estimates of the emergency requirements are also summarized in Table 3-11.

Table 3-11 Power Level Estimates for Deployment and Emergency

Phase	Duration	Power Level	Attitude Control Required
Launch & Deployment			
Orbit Transfer & Circularization	30 min	High	yes
Initial Check-out	30 min	Medium	yes
Umbrella Movement	60 min	Medium	no
Extension Movement	60 min	Medium	no
Science Leg Movement 1	60 min	Medium	no
Science Leg Movement 2	60 min	Medium	no
Final Check-out	30 min	Medium	no
Sun Acquisition	120 min	High	yes
Total Time	7.5 hrs		
Emergency			
Diagnosis & Decision	24 hrs	Low	no
Sun Acquisition	2 hrs	High	yes
Total Time	26 hrs		

Now the actual power required for the different levels must be estimated. Low power is used only in the emergency phase. During the one day decision period, power would be required for only the basic computer tasks and the transmission of telemetry for diagnosis. At the medium power level, power is needed to run the basic computer systems

and telemetry along with the deployment actuators. At high power, all systems except for the payload and high rate communications need to be available. These classifications are summarized in Table 3-12, below.

Table 3-12 Estimated Demand at High, Medium, and Low Power Levels

Low Power		Medium Power		High Power	
Component	(W)	Component	(W)	Component	(W)
ACS Comp & Elec	20	ACS Comp& Elec	20	ACS Comp & Elec	20
Power Control	20	Power Control	20	Power Control	20
C & DH	30	C & DH	40	C & DH	40
Communications	25	Communications	25	Communications	25
Thermal Control	20	Thermal Control	20	Thermal Control	50
		Mechanisms	300	IMU	23
				Sun Sensors	2
				Magnetometers	3
				Magn Torquers	75
				Reaction Wheels	1050
Totals	115		415		1308

Using these estimates of power and the estimates of duration from above, the energy requirements can be determined. The deployment and check-out phase requires 5345 Whrs capacity, and the emergency phase requires 5375 Whrs. By assuming the larger of the requirements, one has enough information for a detailed sizing of the battery system.

Since ideally the full battery capacity will only be used once, and certainly less than 10 times, the depth of discharge (DOD) can be specified at 100%. Assuming a discharge efficiency of 0.9 and a bus voltage of 30 V, the required Ahr capacity is computed as

$$C = \frac{Pt}{DOD \cdot V_{bus} \cdot \eta} = 199.1 \text{ Ahrs} \cong 200 \text{ Ahrs} \qquad \text{Eq. 3-23}$$

where Pt is the capacity of 5375 W·hrs. By rearranging equation 3-23, the depth of discharge used by the system during eclipse periods is determined to be only 9.4% for 510 Whrs capacity. This low DOD indicates that the system will normally operate at low efficiency. The number of cells required in series can be computed from the bus voltage and the individual cell voltage of 1.24 V. In addition, an open-circuit failure of one cell with bypass diode voltage drop of 1.1 V is assumed. The number is calculated as

$$N_S = \frac{V_{bus}+V_{diode}}{V_{cell}} + 1 = 26.1 \text{ cells} \cong 27 \text{ cells} \qquad \text{Eq. 3-24}$$

This gives a minimum discharge voltage of 33.48 V. A NiH_2 cell of 200 Ahr capacity weighs 4.308 kg [12], yielding a total battery mass of 116.4 kg.

The last step in the battery design and sizing is to verify the conventional wisdom that NiH_2 cells provide better performance than NiCd batteries. [12] indicates that NiCd cells are available in sizes up to 50 Ahrs. At this capacity, the required bus voltage is 56 V, and the estimated cell mass is 94 kg. This gives a mass difference of just 23 kg over the NiH_2 cells, but with all the additional complexities of the much higher voltage. The only real reason to use NiCd cells with this type of performance is if one is faced with tight volume constraints. While the interferometer is volume constrained in terms of the truss fitting in a payload shroud, there is plenty of volume available within the trusswork. For the interferometer spacecraft, NiCd batteries offer slightly better mass performance at the cost of a higher complexity system.

3.4.4 Power Distribution and Regulation

Design of the power distribution system and power regulation is guided by four principles that also apply to spacecraft design in general [5]. First is to eliminate single-point failure modes, which is usually accomplished through use of redundant components. Second, is to design for graceful degradation in performance. This is achieved by configuring the system such that failures of single components slowly reduce system performance rather than causing loss of whole parts of system function. Third, is to avoid the propagation of failures, and this is accomplished by isolating components from each other such that individual failures do not affect the performance of other pieces. Fourth, is to provide for adequate testing in the design. This means using only those components that can be tested and providing for testing of the entire system before launch. It also implies designing for sufficient telemetry to give detailed knowledge of system performance on orbit.

A fundamental way of addressing these design principles in the power distribution system is through use of a dual bus architecture. In this type of architecture, each bus has independent power generation, energy storage, and control components. In this way, the power system is inherently redundant, and loads can be divided between the two buses. Generally, with a dual power bus, each separate unit of redundant spacecraft components is connected to a different bus (i.e., each of the two transponders is connected to a separate bus). More redundancy can be added to the architecture by providing switches and fuses such that the failure of one bus causes a dependent component to switch its power source to the other bus.

The interferometer power system will adhere to these design principles, but the distribution network is complicated by the geometry of line of sight pointing and rotation. Sufficient power must be supplied to the system components at worst case orientations, and excess power must be dissipated at best case orientations. Each panel will have to be isolated by a blocking diode to prevent bus power drain when the panel is in shadow. These complications lead to the panel arrangement described in the previous section. For a dual bus system, the arrangement requires lengthy cabling to bring the power from all six panels on a bus to central control points for regulation and conversion. Complexity in the system from the shadowing variations can be minimized by using only a single bus design. Redundancy is maintained in a single bus by using two sets of power control electronics, with one set in stand-by mode, and by double-insulating the system against short failures. In addition, individual system components are isolated by diodes and fuses to protect overall system in the event of single component failure. The interferometer will use a single bus system in the interests of minimizing operational complexity.

As for power regulation and conversion, there is a choice between centralized and distributed conversion and between direct-energy-transfer (DET) and peak-power tracking regulation (PPT). Power conversion is necessary since not all components run at the standard bus voltage of 30 ± 2.5 V. Most logic components run at 5 volts, and sensor and amplifier components run at about 15 volts. With distributed power conversion, power is delivered to all components at the standard bus voltage and is then converted at the component level. The advantage of this is that components can be designed to operate at their own optimum voltage, but this flexibility comes at the cost of incorporating a power conversion unit into each piece of equipment. With centralized conversion, the power from the generator is immediately converted to three or four voltage levels (e.g., 30 V, 15 V, and 5 V), and then delivered to all components. Table 3-13 summarizes the interferometer components that fall into each voltage category. Note that the active optics components, which make heavy use of piezo-ceramics, require voltages of about 100 V. Since the vast majority of components in this system fall in the standard categories of 5, 15, and 30 volts, it makes sense to use a partially regulated, centrally converted bus. The power conversion unit regulates the array voltage to 30 ± 2.5 volts. From this, about 550 W of each bus are converted to 5 and 15 volts and forwarded to the logic and sensor units. The components that can accept power in the 25 - 35 V range are able to operate at the array regulated voltage, and thus do not require any conversion. Active optics components will have to incorporate individual converters and draw power from the array regulated supply.

Peak power tracking is a method that acts in series with the arrays to non-dissipatively extract the exact power required by the system up to the maximum power

Table 3-13 Interferometer Component Voltage Categories

5 Volts		15 Volts		25 - 35 Volts		Other (~100 V)	
Component	Pwr	Component	Pwr	Component	Pwr	Component	Pwr
Magntmtr	3	Star Trackers	21	Thrusters	10	Active Mirror	150
ACS Comp	20	Sun Sensors	2	RWAs	1764	PCDs	250
T & CU	30	Transponders	12	Mag Torquers	210		
MMU	15	Comm Amps	35	FGIs	90		
Thermal	260	Lasers	100	IMU	24		
Sci Comp	45			Siderostats	200		
Total	373		170		2298		400

point. It accomplishes this by dynamically controlling the operating point of the solar arrays, but it consumes from 5 -7 % of the total power. This method is most advantageous for missions of relatively short duration. The DET method passively regulates the system power by diverting excess power to a shunt resistive network that dissipates the energy. The shunt regulators are located near their solar panels and facing deep space to improve the efficiency of dissipation. This is a particularly reliable system for long lifetime missions which tend to require large power loads that vary significantly over the lifetime. The shunt regulators further aid system integration by preventing dissipation of excess

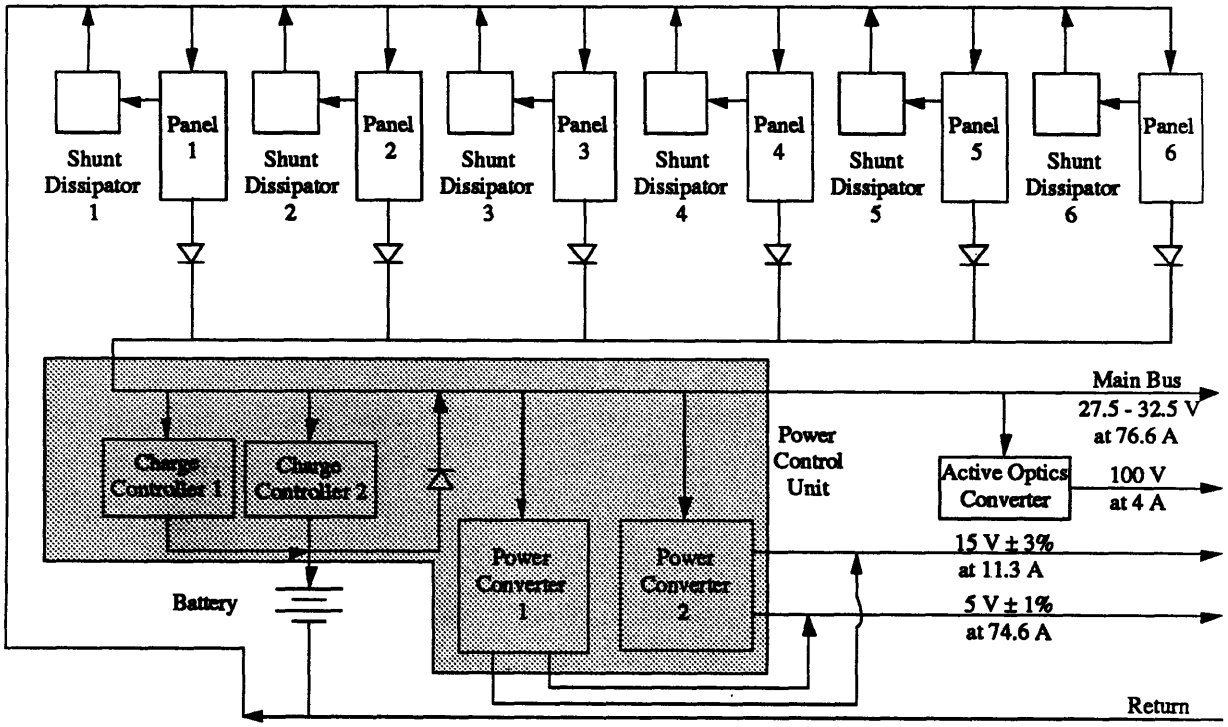

Figure 3-11 Power Control and Distribution Block Diagram

power within the spacecraft where the heat is harder to get rid of. The interferometer will use the DET method with a quasi-regulated system that allows the bus voltage to be controlled independently of the batteries. A charger is in series with the batteries, but fixed at a potential several volts above the batteries during charging. Throughout most of the mission, the batteries will be fully charged, and the drop across the charger is smaller, but still allows the bus to be regulated independently. In the event that battery discharge becomes necessary, bus voltage has dropped a diode voltage lower than the battery voltage, and the bus becomes unregulated at the potential of the batteries. Figure 3-11 shows a schematic of the power subsystem, with its generation, storage, distribution, and control elements.

3.5 Propulsion Subsystem

The design of the propulsion subsystem is a problem mainly of sizing. Since the system is not required to perform attitude control, there are not many trades that need to be considered on the system level. Instead, the system capabilities for launch and circularization, for orbital maintenance in the face of perturbations and decay, and finally, for controlled de-orbit need to be examined. The main object of this section is to determine the required levels of delta v for each phase of the mission, and to then determine whether the best choice for meeting these requirements is an all liquid system, or a mixed solid-liquid system. Only currently existing chemical propulsion hardware is considered in this section.

3.5.1 Delta V Calculations

Orbital Injection: The best place to start in determining the propulsion requirements is with the launch itself. As explained in Chapter 2, the interferometer uses a 700 km sun-synchronous orbit. This requires use of the Western Test Range (WTR) and a Titan IV booster. With a mass of approximately 12,500 kg, a Titan IV/NUS (no-upper-stage) launch from the WTR can place the spacecraft either in a 200 km circular orbit, or in a 125 x 700 km elliptical orbit [37]. The delta v requirements for these two options can be directly compared to determine the better choice.

With an initial 200 km circular orbit, a Hohmann transfer would be used to achieve the 700 km mission altitude. Using the standard equations:

$$v_{circ} = \sqrt{\frac{\mu}{r}} \qquad \text{Eq. 3-25}$$

$$\varepsilon = -\frac{\mu}{2a} \qquad \text{Eq. 3-26}$$

$$v = \sqrt{2\left(\varepsilon + \frac{\mu}{r}\right)} \qquad \text{Eq. 3-27}$$

the relevant velocities can be found,

$$v_{200} = 7784.4 \text{ m/s}$$
$$v_{Hp} = 7925.6 \text{ m/s}$$
$$v_{Ha} = 7365.7 \text{ m/s}$$
$$v_{700} = 7504.3 \text{ m/s}$$

yielding the following delta v requirements:

$$\Delta v_p = 141.2 \text{ m/s}$$
$$\Delta v_a = 138.6 \text{ m/s}$$
$$\Delta v_{tot} = 279.8 \text{ m/s}$$

In the second case, with a 125 x 700 km elliptical orbit, only a circularizing burn at apogee needs to be made. With a semi-major axis of 6790.5 km, and using equations 3-27 to 3-27, the relevant velocities are found to be:

$$v_a = 7343.8 \text{ m/s}$$
$$v_{700} = 7504.3 \text{ m/s}$$
$$\Delta v_{tot} = 160.5 \text{ m/s}$$

From these delta v calculations, it seems clear that the second case is the better choice. In addition to requiring less total delta v, it also permits the option of using a single-stage solid rocket for the circularizing burn. The first option needs either a two-stage solid or a liquid system which may introduce additional system complexity. The trade between these two options is examined in section 3.5.2.

Perturbation Corrections: Another set of factors to consider in determining delta v requirements are orbital perturbations due to launch vehicle injection errors, third-body influences, and orbital decay. The three-sigma injection accuracy of the Titan for this type of orbit is ±0.01° inclination, and ±15 km perigee altitude [36]. In addition, an error in delta v of approximately 2% can be expected from the circularization burn which will cause an orbital eccentricity. It is important to realize that for this mission, the altitude is not all that critical, provided it is above about 675 km. What *is* critical is the combination of altitude and inclination, since a sun-synchronous orbit is desired. Recall from Chapter 2

that the sun synchronous condition (with an additional term to account for eccentricity, e) is given by

$$\dot{\Omega} = -\frac{3J_2R_e^2}{2}\sqrt{\frac{\mu}{a^7}}\cos i\left(\frac{1}{1-e^2}\right) \qquad \text{Eq. 3-28}$$

for $\dot{\Omega} = 1.991 \times 10^{-7}$ rad/sec = 0.985609 deg/day. The required inclination for the 700 km circular orbit is 98.188°. Both injection errors in altitude and in inclination will cause errors in the rotation of the line of nodes. For a worst case three-sigma injection error of -0.01° inclination, +15 km altitude, and eccentricity of 0.000877, the total inclination error is 0.0449° and the rotation rate is only 0.9802 deg/day. Of the 0.00542 deg/day error in rotation rate, 22% is due to inclination injection error, 77.6% to altitude error, and 0.4% to injection burn eccentricity error. The total error in rotation rate causes an error in the line of nodes of 19.8° over the ten year mission.

The primary concern of an error in the line of nodes is that it may shift the orbit away from the twilight conditions that allow near continual sunlight. Figure 3-12, below, shows that a rotation of only 19.8° still leaves the spacecraft 220 km above the horizon with respect to the sun. On the other hand, this leaves a margin of less than five degrees for any

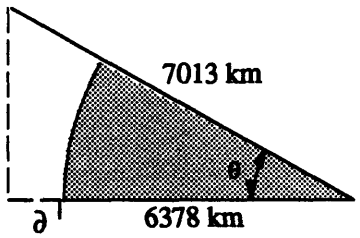

For:
$\theta = 19.8° \text{ — } \partial = 220$ km
$\partial = 0$ km — $\theta = 24.5°$

Figure 3-12 Sun Angle for Error in Line of Nodes from Twilight Condition

other perturbations. If this injection error were to be corrected, it could most easily be done by performing a plane change to the correct inclination for the actual altitude at the beginning of the mission. The maximum inclination change expected is 0.0449°, and the delta v required for this maneuver is computed from

$$\Delta v = 2000\sqrt{\frac{\mu}{a}}\sin\left(\frac{\theta}{2}\right) \qquad \text{Eq. 3-29}$$

which yields only 5.9 m/s.

Third-body perturbations may also have an impact on the proper rotation of the line of nodes. These perturbations are analogous to tidal forces and are caused by the

gravitational forces of the sun and the moon. Their impact on the line of nodes in degrees per day is described by:

$$\dot{\Omega}_{moon} = -0.00338\frac{\cos(i)}{n}$$

$$\dot{\Omega}_{sun} = -0.00154\frac{\cos(i)}{n} \qquad \text{Eq. 3-30}$$

For the nominal orbit, these effects amount to only 0.12 degrees and 0.05 degrees per 10 year mission, respectively. That means a combined effect of less than two tenths of a degree over the lifetime of the mission. Clearly, the impact of third-body perturbations is insignificant.

Orbital Decay: The last perturbation that must be considered in deriving the delta v requirements is orbital decay due to atmospheric drag. As already discussed in Chapter 2, the interferometer is expected to fall from 700 to 635 km altitude over 10 years with a nominal atmosphere and maximum cross-sectional area. As the orbit decays, the inclination does not change, so the orbit becomes no longer sun-synchronous. If the orbital altitude is updated every half-year, and then the change in the line of nodes is integrated over ten years, the total change is 3629.2°. This is an error of 29.2° from a sun-synchronous orbit, and is over the threshold for eclipse of 24.5° derived in Figure 3-12 on the previous page. This amount of error indicates that there must be some means of correcting the orbit in order to maintain a twilight orbit for ten years.

There are two obvious approaches to correcting the orbit: the altitude could be boosted, or its inclination could be adjusted. One possibility is to use some sort of continuous, low-thrust propulsion such as with an ion engine, but this would prove unfavorable due to both the cost of advanced development, and more importantly, to structural excitation. Instead, liquid propellant thrusters are considered. The options of altitude adjustment and inclination change can be compared by examining the ratio of their required delta v's. The inclination adjustment is accomplished with a plane change maneuver, while the altitude adjustment would be via a Hohmann transfer. The equation for the ratio is derived below and is plotted in Figure 3-13 over a range of initial altitudes from 635 to 699 km (r_1 from 7013 to 7077 km).

$$\frac{\text{plane change } \Delta v}{\text{Hohmann } \Delta v} = \frac{2v_{r_1}\sin\left(\frac{\theta}{2}\right)}{(v_{ap}-v_{r_1})+(v_{r_2}-v_{per})}$$

$$= \frac{2\sqrt{\frac{\mu}{r_1}}\sin\left(\frac{\theta}{2}\right)}{\left(\sqrt{2\mu\left(\frac{1}{r_1}-\frac{1}{r_1+r_2}\right)}-\sqrt{\frac{\mu}{r_1}}\right)+\left(\sqrt{\frac{\mu}{r_2}}-\sqrt{2\mu\left(\frac{1}{r_2}-\frac{1}{r_1+r_2}\right)}\right)}$$

$r_2 = 7078$ km

$$\theta = 98.1876^\circ - \text{acos}\left(\frac{\dot{\Omega}_{ss} r_1^2}{-1.5 n J_2 R_E^2}\right) \qquad \text{Eq. 3-31}$$

Figure 3-13 demonstrates that the delta v ratio is always less than one, so the plane change maneuver is more efficient at maintaining the sun synchronous orbit.

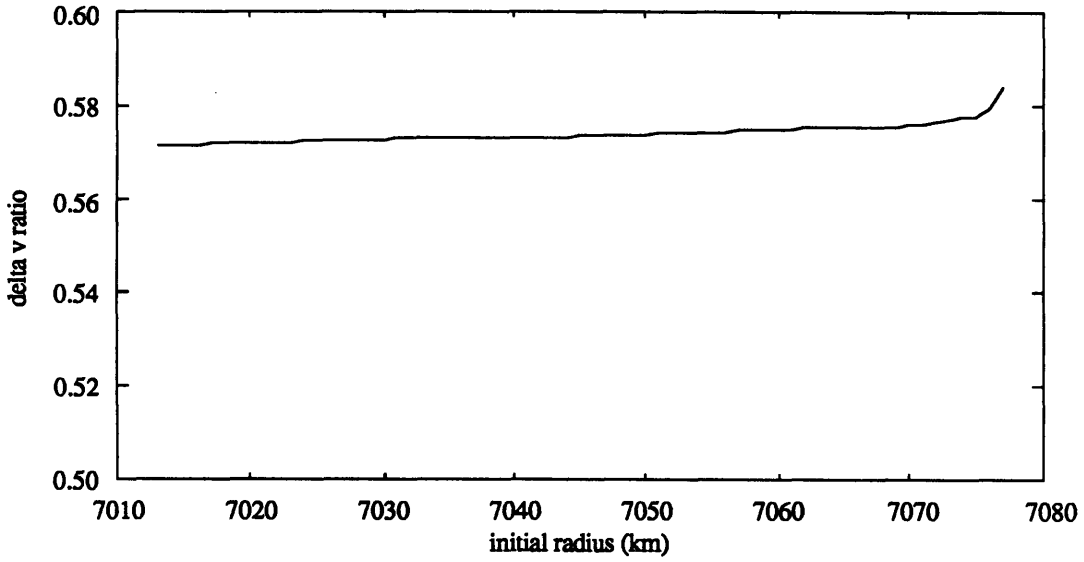

Figure 3-13 Ratio of Plane Change to Hohmann Transfer Delta V for Orbit Correction

The next factor to determine is how many plane change maneuvers to make. Two representative schemes considered are to correct once at the 5.5 year mark, or to correct every half-year. A clue to the outcome of this trade can be deduced by considering the frequency of the corrections as a measure of the error tolerance. By analogy to geosynchronous sub-satellite points, tighter position tolerances are known to require more frequent station-keeping and greater delta v. Indeed, if the delta v requirements are calculated for inclination corrections every half-year and for one at the 5.5 year mark, the results are 19.7 m/s and 9.0 m/s respectively. It can be concluded that the single correction is more efficient, provided, of course, that a greater error can be tolerated. The error in the

line of nodes for such a scheme comes to 15.5° over ten years. If it is assumed that the 5.9 m/s were used to correct for any injection errors at the beginning of the mission, then the error in the line of nodes is well within the twilight orbit requirement of 24.5°.

Controlled De-Boost: The last phase of the mission that will require delta v is a controlled re-entry, used in the interests of minimizing space debris. This is easily calculated as a Hohmann transfer from the final altitude to the surface. As a conservative estimate of orbital decay, a final altitude of 650 km is assumed, and the de-boost delta v is calculated from equation 3-32 which gives a delta v of 184.8 m/s for r = 7028 km.

$$\Delta v_{deorbit} \cong v_r \left(1 - \sqrt{\frac{2R_E}{R_E + r}} \right) \qquad \text{Eq. 3-32}$$

A summary of the mission delta v requirements is given in Table 3-14 and includes a 10% design margin. The circularization burn could be accomplished with either a solid or liquid system, but the remaining burns require a storable liquid system. The trade of which type of system is best is examined in the following section.

Table 3-14 Interferometer Delta V Requirements

Maneuver	Delta V Required (m/s)
Circularization Burn	160.5
Injection Error Correction	5.9
Drag Correction	9.0
Controlled De-Boost	184.8
Total	360.2
Total with 10% Margin	396.2

3.5.2 Engine Selection

Since delta v burns are required at widely spaced times during the mission, some sort of liquid propulsion is necessary, but as previously mentioned, there is a choice between a purely liquid and a mixed solid-liquid system, with a solid motor used for the circularization burn. Since they are common to both options, liquid thruster systems are considered first.

Important parameters including mass, I_{sp}, thrust, and type of propellant for a variety of liquid thruster systems are shown in Appendix D. For the sake of system

redundancy, two thrusters are chosen for the spacecraft. Propellant mass for each truster is derived using the rocket equation as shown below, and the total mass is derived assuming tankage and hardware mass equal to 20% of the propellant weight. The spacecraft dry mass (minus tankage) is assumed to be 11000 kg.

$$m_{prop} = m_{final}\left[\exp\left(\frac{\Delta v}{gI_{sp}}\right)-1\right] \qquad \text{Eq. 3-33}$$

Burn times are calculated for the different mission firings of injection error correction, decay correction, and controlled de-boost. For the all-liquid option, the time for the circularization burn is also calculated.

Monopropellant and a bipropellant thrusters are now selected for comparison. The Hamilton Standard monopropellant thruster with 689 N thrust is chosen, since it is the lowest mass monopropellant system that also has a reasonable thrust level/burn time. For the bipropellant thruster, the Marquardt 400 N model is selected. It is chosen over the lower massed TRW model because of the better stability and handling characteristics of mono-methyl hydrazine (MMH) as compared with regular hydrazine. The result of this analysis is that for the all liquid option, a monopropellant system of 2577 kg or a bipropellant system of 1905 kg could be used. For the mixed solid/liquid system, these values are 1351 kg and 1015 kg, respectively.

Also shown in Appendix D is a summary of current solid rocket motors that could be used in the mixed solid-liquid system. For each motor, delta v is calculated from the rocket equation, and the one that most closely matches the system requirement of 176.6 m/s is selected. This motor is the STAR 37F, which is a standard apogee kick motor that has flown with both FltSatCom and Intelsat V. The calculations for this motor assume a standard 10% propellant off-load. This motor provides an approximately 12% delta v margin for the circularization burn, and weighs 829 kg.

The four options for the propulsion system can now be compared: either all-liquid or mixed solid-liquid, and either monopropellant or bipropellant. The total system masses for each option are shown in Table 3-15. From this matrix, it is fairly obvious that the bipropellant system is significantly more efficient than the monopropellant system. A savings of at least 336 kg is enough to make up for the additional complexity inherent in a bipropellant system. The remaining choice is between the liquid and mixed systems. The mixed system provides a savings of 61 kg and, although it may not be intuitive, is more reliable and less complex. Solid motors are the preferred engines for orbital injections

Table 3-15 Mass Summaries of Propulsion System Options

	Mixed Solid-Liquid System	All Liquid System
Monopropellant Hydrazine	2180 kg	2577 kg
Bipropellant N_2O_4/MMH	1844 kg	1905 kg

because they have large thrust and simple operation with good historical reliability. If an all-liquid system is chosen, it must be positioned on the outside face of the fourth vertex for use during the injection burn. This is not, however, the most favorable location after deployment from the standpoint of dynamic stability. With the mixed system, the solid motor is placed at the fourth vertex, while the liquid thrusters are free to be positioned anywhere subject to dynamic and optical contamination concerns. For these reasons, and because of the slight mass savings, the hybrid solid-liquid system is selected.

3.5.3 Subsystem Summary

The propulsion system is responsible for inserting the interferometer into the proper orbit, and for maintaining the vital orbital properties throughout the mission lifetime. Orbital maintenance requires correcting for injection errors and for perturbations caused mainly by drag. These errors can cause the orbit to lose its twilight characteristics that are important to the system performance. Delta v is also required to provide a controlled re-entry for the spacecraft at the end of the mission. The delta v requirements are summarized in Table 3-16 along with the hardware characteristics. To meet the propulsion requirements, a mixed solid-liquid system is chosen based on system reliability and mass. A solid apogee kick motor is used to circularize the orbit at the proper altitude, and an N_2O_4/MMH thruster system handles the maintenance and de-boost tasks. Tankage and connectors are assumed to be 20% of the propellant weight.

Table 3-16 Propulsion System Delta V and Component Summary

Propulsion Requirements			
Maneuver		Delta V (m/s)	Delta V with 10%Margin (m/s)
Injection Burn		160.5	176.6
Injection Error Correction		5.9	6.5
Decay Correction		9.0	9.9
Controlled De-boost		184.8	203.3
Total: for Solid Motor		160.5	176.6
for Liquid Thrusters		199.7	219.7
Hardware Specifications			
System Component	Quantity	Mass (kg)	Power (W)
STAR 37F AKM	1	829.0	-
Marquardt 400 N Thruster	2	7.6	10.0
N_2O_4		458.2	-
MMH		381.8	-
Tankage & Connectors	2	168.0	-
Total		1844.6	10.0
Total w/ Margin		2029.1	10.1

Chapter 4

Thermal and Structural Control Analysis

The thermal and structural subsystems are treated separately from those discussed in Chapter 3 because they have two distinct characteristics in common. Both the thermal and structural design have a direct impact on the performance of the optical system, and both are strongly dependent on the actual spacecraft configuration. Each of the topics addressed in the first two chapters were strongly influenced by the desire to improve the performance of the payload, but none were specifically designed to meet the physical requirements of interferometry in terms of differential pathlength and tilt errors. This is the primary role of the thermal and structural designs. High levels of thermal control are necessary to ensure the surface qualities of the optical elements, and structural control is required to minimize the effect of vibrations on the optical performance. Both the thermal and structural analysis are dependent on a model of the configuration of the spacecraft. The thermal analysis requires a knowledge of the spacecraft's orientation with respect to the sun and of any shadowing effects on the important components. The structural analysis requires a fairly detailed model of the structure and its dynamics in order to assess the impact of vibrations on the payload.

This chapter begins with a description of the spacecraft model used in the following analyses. It describes the finite element model which provides a mathematical description of the spacecraft configuration and the eigenstructure of its dynamics, and it also discusses the modal model used in evaluating the dynamic performance of the system. This description is followed by a summary of the structural control system, including the requirements, disturbance models, and an estimation of the control tools needed to achieve performance. The chapter is concluded with the thermal design, including its requirements, a general design approach, and detailed analysis of optical element heat balance.

4.1 Spacecraft Model

4.1.1 Configuration and Finite Element Model

This section introduces the model used throughout the remainder of the chapter for dynamic and geometric analyses. The spacecraft is modelled as a tetrahedral truss structure using the ADINA finite element software. This model provides a quantitative description of the geometry and the eigenstructure information required by the following modal model. It includes 452 nodes connected by 1293 beam elements, as well as 294 plate elements representing solar arrays, radiators, antennas, and thermal shields. Optical elements are modelled as nodes connected to the main trusswork via beam elements, and other subsystem components are modelled as nodal point masses. Figure 4-1 shows the assembled model with plate elements shaded and struts marked by lines.

The struts themselves are modelled as 12 degree of freedom beam elements of two-inch diameter graphite/epoxy beams. The solar arrays are represented by silicon plates of 200 μm thickness, while radiators are modelled as 1 cm aluminum plates, and the thermal shields and phased array antennas are modelled as composite plates of 0.5 cm and 5 cm thickness, respectively. Each optical element is represented as a nodal point mass and inertia, and is connected to the surrounding truss with beam elements. The siderostat, primary, and secondary mirrors are each connected to the truss by three beam elements. Fast-steering mirrors and pathlength control device (PCD) elements are cantilevered from the truss nodes by a single beam element, while the combining optics are supported in the fourth vertex by three struts. Each siderostat/beam compressor assembly, PCD, and vertex is enclosed within thermal shield material to reduce the effects of varying illumination and provide a thermal control volume. The solar array plates are mounted on the inside faces of the science plane legs as described in the design of the power subsystem in section 3.4. The relatively large masses of the other subsystem components are represented by nodal point masses rigidly linked to the three outermost nodes at each vertex. The near legs, stretching from the fourth vertex to the science plane, include an overlap section centered lengthwise on the beam which is intended to approximate the extensional deployment joint used in these legs. This means the portion of these legs nearer to the fourth vertex has a slightly smaller cross-section than the portion adjoining the science plane.

With six degrees of freedom (3 translations and 3 rotations) at each of 452 nodes, the full model has a total of 2712 degrees of freedom. Using ADINA on MIT's Cray X-MP, a solution was generated for the frequencies and modeshapes of the first 60 flexible

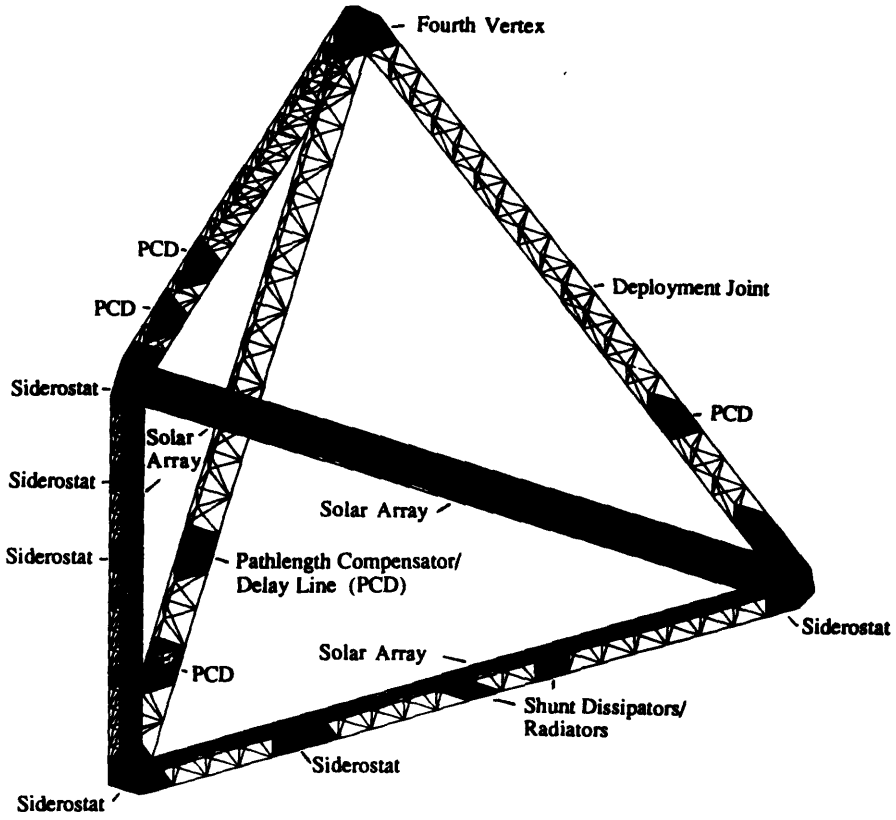

Figure 4-1 SERC Interferometer Spacecraft Configuration

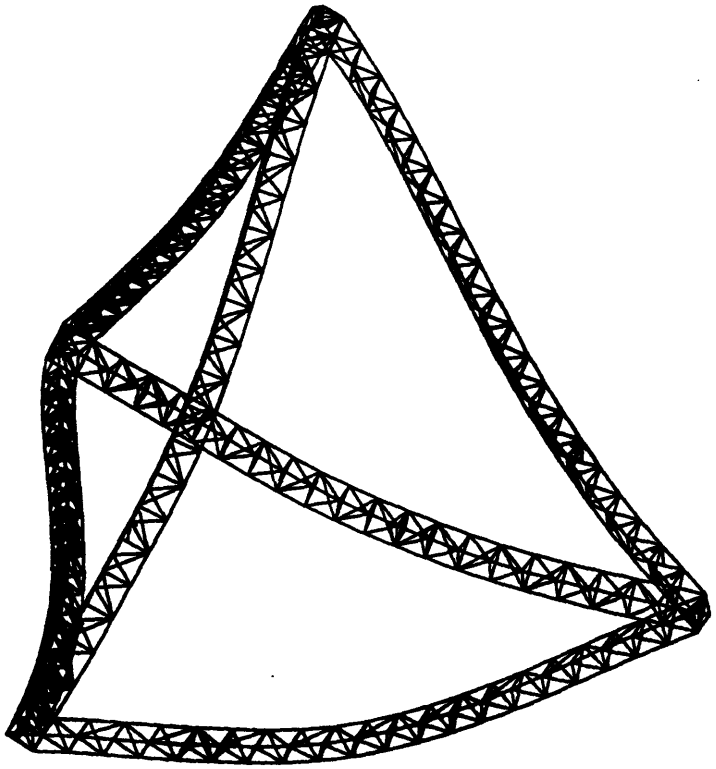

Figure 4-2 Sample Structural Modeshape (Mode 10, 3.655 Hz)

modes of the structure. A sample modeshape is shown in Figure 4-2, and can be compared with the undeformed state shown in Figure 4-1. One main side effect of the overall structural symmetry of the design is a high density of similar modes in the frequency domain. This is illustrated by the fact that all 60 modes occur between 2.99 and 15.11 Hz, resulting in an average frequency spacing of just 0.2 Hz. The number of modes was limited by the memory and efficiency of the remote terminal used. The model is adequate for an illustration of the principles of structural control design and for the estimation of the level of control that will be required to meet performance.

4.1.2 System Dynamic Model

The finite element analysis described above yields a matrix of eigenfrequencies, Λ, and a matrix of modeshapes, Φ. This information can be incorporated into a modal state-space model that provides the nodal response to an arbitrary input. Since the detailed derivation of the modal model from the eigenfrequencies and modeshapes can be found in any good text on structural dynamics [22], only the result is shown here. The model fits the general state-space form of:

$$\begin{aligned} \dot{x}(t) &= Ax(t) + Bu(t) \\ y(t) &= Cx(t) + Du(t) \end{aligned} \qquad \text{Eq. 4-1}$$

such that:

$$\begin{bmatrix} \dot{\eta}(t) \\ \ddot{\eta}(t) \end{bmatrix} = \begin{bmatrix} 0 & I \\ -\Lambda & -2\zeta_i\omega_n \end{bmatrix} \begin{bmatrix} \eta(t) \\ \dot{\eta}(t) \end{bmatrix} + \begin{bmatrix} 0 \\ \Phi^T \end{bmatrix} B\, Q(t)$$

$$y(t) = C \begin{bmatrix} \Phi & 0 \end{bmatrix} \begin{bmatrix} \eta(t) \\ \dot{\eta}(t) \end{bmatrix} \qquad \text{Eq. 4-2}$$

where y(t) are the outputs in physical coordinates as defined by C, η are the modal coordinates, ζ_i are the modal damping ratios, ω_n are the modal frequencies, and Q(t) are the arbitrary inputs through B. ζ_i are added after the evaluation of the finite element model, assuming that the damping does not significantly affect the modeshapes. This assumption is valid for ζ up to about 10%, after which the finite element model should be re-computed with the damping incorporated. In the following analysis, the nominal "undamped" structure is computed with a damping ratio of 0.1%.

In this case, the arbitrary input is some vibrational disturbance, and the desired outputs are the translations of the optical nodes. To compute the actual system performance, the variation from the nominal pathlength in each optical train is computed

and differenced with its pair to determine the differential pathlength (DPL) error. The optical paths travel from the siderostat, through the beam compressor elements, to the nearest vertex. Here, the light is reflected from a fast-steering (FST) mirror up the near leg to the PCD which also acts as a delay line. The PCD returns the light back to the same vertex where it is then reflected up the entire length of the near leg and into the combining optics at the fourth vertex. For simplicity of computation, only two of the eight optical paths are computed. One is for a siderostat located at approximately the center of a truss leg, and one for a siderostat located at a vertex location. Experience with the SERC interferometer testbed indicates this pair should provide the worst case performance for the system.

4.2 Structural Control Analysis

In analyzing the spacecraft structure, static considerations are ignored. It is accepted as given that the structure should be able to survive launch loads, and the static analysis provides no insight to the system performance on orbit. The structural dynamics, on the other hand, are tremendously important to the primary source of performance degradation: differential pathlength error. By applying the modal model just described, a estimate of this parameter can be derived for representative spacecraft disturbances. The extremely tight tolerances for DPL error generally require the application of controlled structures technology (CST) for the system to meet requirements. It should be pointed out that CST does not necessarily imply the use of active feedback controllers. Much of the technology, in fact that which tends to be applied first, involves passive elements. This section seeks to outline the CST approach to achieving performance objectives, and to demonstrate the application of CST technology and its effect.

The section first lays out the requirements for the subsystem in terms of DPL error and describes models for the main disturbance sources on the spacecraft. These disturbances are then applied to the performance model to determine the "open-loop" response. The general approach of CST design is then discussed with a survey of the CST "toolbox." Finally, CST design is applied to the system model to estimate the level of control that is necessary to achieve performance. This is, in effect, sizing the structural control system.

4.2.1 Requirements Specification

As described in Chapter 1, the allowable DPL error is determined by the desired quality of the intensity function as derived through the Fourier analysis, and is a function of the wavelength [6]. The measured intensity function for a sinusoidal DPL error, δl, is given by:

$$I_{max}=I_T+V(u)\left(1-\pi^2\frac{\delta\ell^2}{\lambda^2}\right) \qquad \text{Eq. 4-3}$$

For an image quality of 95% at the center of the visible spectrum (λ=500 nm), the allowable DPL error is just 36 nm RMS. This specification must hold for frequencies greater than the inverse of the data point sampling time, (82 sec)(n_{sid}-1), or about 0.002 Hz. If an upper limit on the measurable disturbance is placed at 1000 Hz, the structural modal model described abovecovers approximately 2% of this frequency interval (3 to 15 Hz). If the contributions of each frequency interval to the total RMS error are divided equally, then the allowable error for the system model is only 0.72 nm. This is specified as the performance requirement for the modelled structure.

4.2.2 Disturbance Environment and System Response

There are numerous sources of vibrational disturbances on board a spacecraft, and they can easily be broken down by subsystem. A fairly good summary of the sources and models for their force or torque signals can be found in [11]. Fortunately, vibrational sources typically found in most of the subsystems have already been eliminated by careful selection of components and configuration. The main contribution of the command and data handling system to the disturbance environment would be vibrations from data tape recorders, but this noise source has been eliminated by the selection of solid-state data recorders for the mission. The contributions of the communications subsystem are usually noise from gimbal drive motors and dynamic coupling of low frequency appendage modes, but these too have been eliminated by selecting phased array antennas. The power subsystem also contributes vibrations through drive motors and appendage modes, which have been eliminated by using body mounted solar arrays.

Probably the worst source of disturbance that does affect this interferometer design comes from the attitude control subsystem. The RWA's used with the interferometer tend to have both periodic and a broadband components. The periodic component is due mainly to rotor imbalances, and acts radially, axially, and about the drive axis at harmonics of the

wheel speed. This disturbance is proportional to the square of the rotor speed, and should scale approximately with the mass of the rotor. The broadband component is due mainly to bearing imperfections, and can be modelled as white noise with amplitude equal to a few percent of the peak periodic signal. For HST RWA's, the periodic components occurred at the 1, 2, 2.8, and 5.2 harmonics of the wheel speed [14]. The HST RWA periodic disturbance can be modelled as:

$$F_x = \omega_w^2\left\{4.17\text{x}10^{-8}\sin(\omega_w)+2.19\text{x}10^{-8}\sin(2\cdot\omega_w)+4.71\text{x}10^{-8}\sin(2.8\cdot\omega_w)+2.38\text{x}10^{-8}\sin(5.2\cdot\omega_w)\right\}$$
$$F_y = \omega_w^2\left\{4.17\text{x}10^{-8}\cos(\omega_w)+2.19\text{x}10^{-8}\cos(2\cdot\omega_w)+4.71\text{x}10^{-8}\cos(2.8\cdot\omega_w)+2.38\text{x}10^{-8}\cos(5.2\cdot\omega_w)\right\}$$
$$F_z = \omega_w^2\left\{1.7\text{x}10^{-8}\sin(\omega_w)+2.51\text{x}10^{-8}\sin(2\cdot\omega_w)+8.59\text{x}10^{-8}\sin(2.8\cdot\omega_w)+10.77\text{x}10^{-8}\sin(5.2\cdot\omega_w)\right\}$$
$$\tau_z = \omega_w^2\left\{5.34\text{x}10^{-9}\sin(\omega_w)+4.18\text{x}10^{-9}\sin(2\cdot\omega_w)+21.06\text{x}10^{-9}\sin(2.8\cdot\omega_w)+40.52\text{x}10^{-9}\sin(5.2\cdot\omega_w)\right\}$$

Eq. 4-4

The interferometer RWA disturbance spectrum is based on this model, but scaled up by a factor of three due to the need for larger actuators. The power spectrum of the periodic disturbance signal over the range of ω_w from 3 to 15 Hz is shown in Figure 4-3. The signal is implemented in the model by using the four discrete sinusiods with a wheel speed set at the frequency of the first structural mode, 2.99 Hz, to represent the worst case speed measurable by the modal model. A broadband component of 5% of the peak level is added as well.

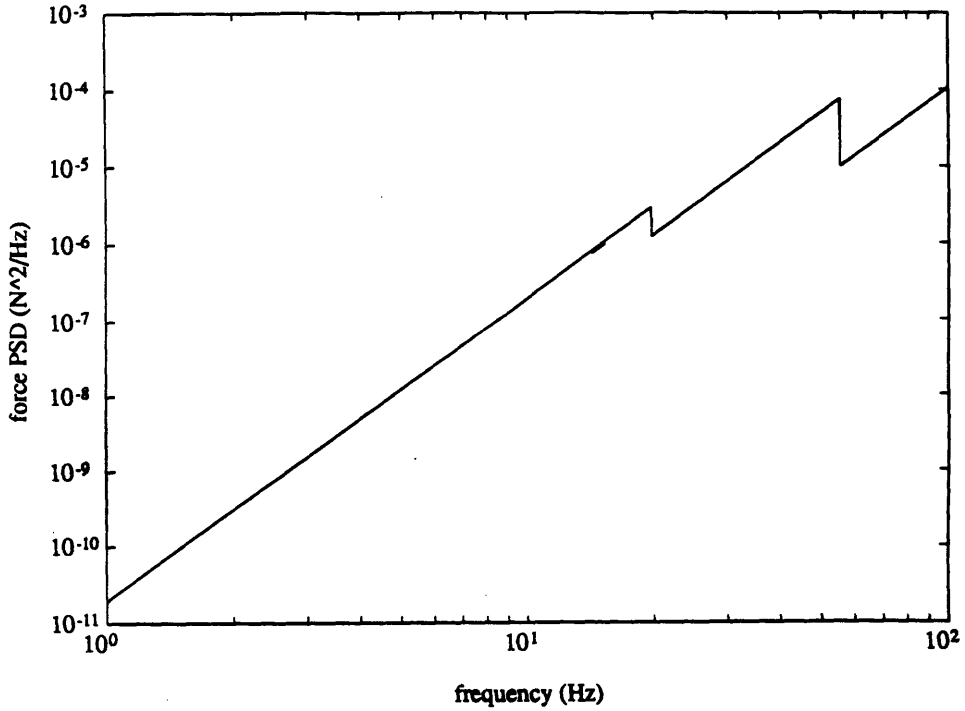

Figure 4-3 Interferometer Reaction Wheel Axial Disturbance Force Power Spectrum

The last source of disturbance considered for this model is from the payload itself. As described in section 3.1, the high frequency actuation of the pointing control is implemented by tip-tilt actuation of the siderostat mirrors. By assuming an actuation range of 2 arcsec and frequency of 10 Hz, the required torque for a siderostat with moment of inertia of about 5.6 kg·m^2 is 0.0011 Nm. The resulting total disturbance model is a 10 Hz sine torque about the tip and tilt axes at each siderostat node and four RWA disturbance spikes at nodes centered in each of the four vertices. The DPL error time signal and frequency response resulting from this disturbance are shown on the following page in Figures 4-4 and 4-5. The RMS of the signal is 11.07 nm, or about 15 times the specified limit for this frequency interval.

4.2.3 CST Design Approach

In order to effectively apply structural control techniques to meet performance objectives, it is helpful to summarized the CST "tools" that are available to the designer and the general scheme for utilizing them. A somewhat more thorough discussion of CST design techniques can be found in [11]. The first step in controlled structures design is something that has been operative throughout this thesis. It is the application of common sense and basic engineering intuition to achieve the objective. In this case, the goal is to minimize vibrational disturbances that affect the optical elements of the system. The first technique used for the interferometer was structural tailoring. The choice of the tetrahedral truss configuration was based on the inherent rigidity of its geometry. In addition, its symmetrical inertial properties minimized environmental disturbances, permitting smaller sized ACS actuators. Finally, as discussed in the previous section, a number of choices have been made in the design of the other subsystems that have eliminated some common sources of noise. These decisions can be viewed as the ultimate in attacking the problem at its source.

The second phase in controlled structures design is the application of passive damping. The desire for an inherently stiff structure usually results in one with relatively low damping. Damping is important both as a direct agent of disturbance rejection and as almost a prerequisite for the application of advanced structural control techniques. It reduces vibrations by providing a means of energy dissipation in the system. Damping can be applied in an optimal manner by targeting high strain energy locations of the most important modes. Damping is also extremely important for the application of higher authority active control loops because these controllers must roll-off in the frequency domain at some point. Damping can help ensure stability through the roll-off region. As a

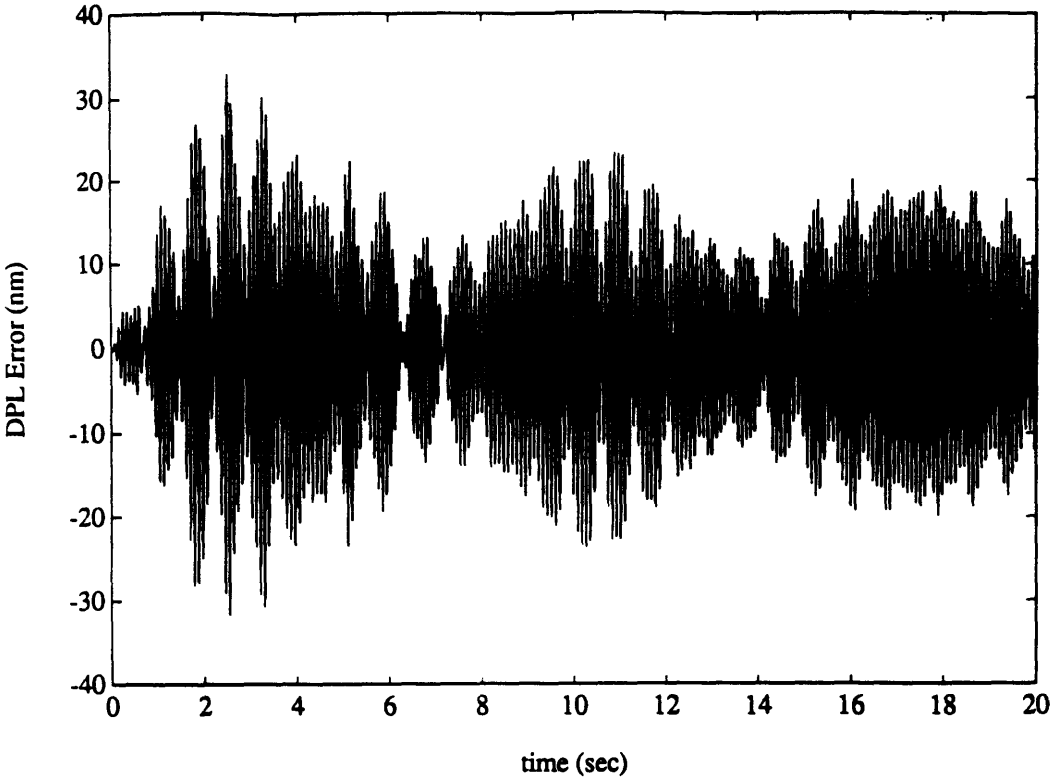

Figure 4-4 Time Signal of Differential Pathlength Error Response to RWA Spikes and Siderostat Actuation

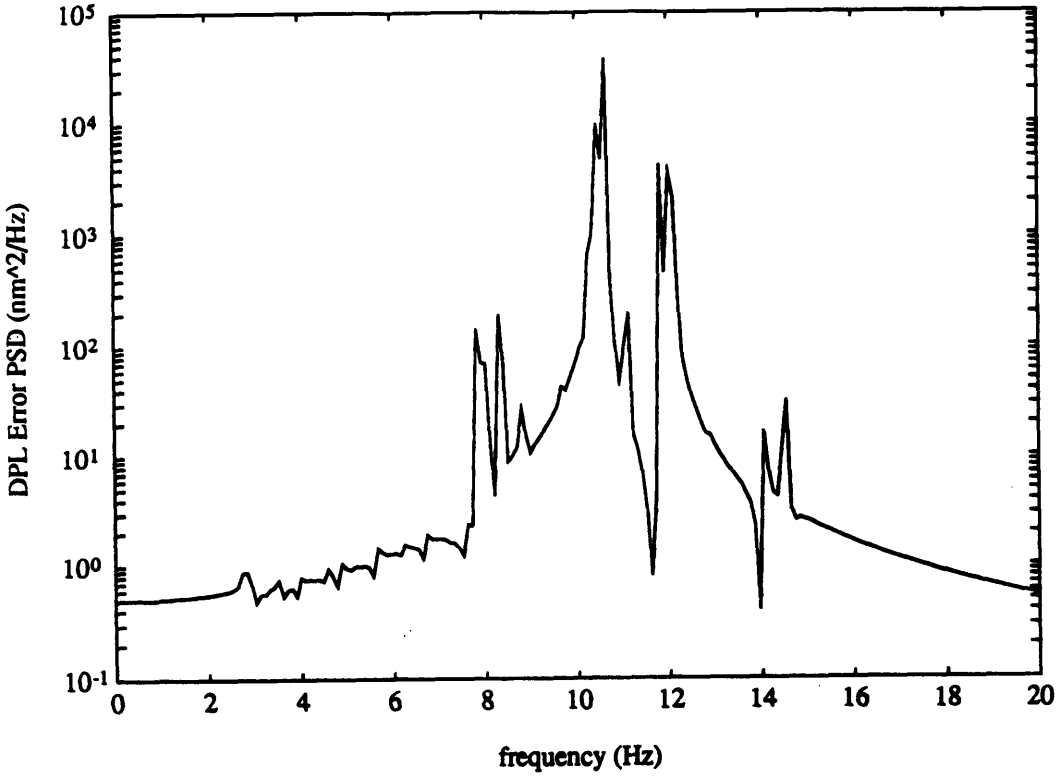

Figure 4-5 Power Spectrum of Differential Pathlength Error Response

general rule-of-thumb, somewhere 1 and 10% damping is required in order to achieve desired results [8]. Damping can be added to a structure in a number of ways. The most common approaches are to use viscoelastic materials, friction dampers, or viscous fluid dampers. Other options are resonant spring-mass-damper systems or shunted piezoelectrics. Rather than directly affecting the source or the receiver, damping techniques typically target the transmission path from the disturbance source to the performance element.

The third phase of structural control design is the use of vibration isolation. This works particularly well for systems with relatively few main source or receiver elements. The goal of isolation is to reduce the transmissibility between the noisy source and the structure or between the noisy structure and a performance element. Isolation mounts can be either soft, for attenuation above a certain corner frequency, or tuned, for strong attenuation at a certain target frequency. Isolation mounts can be either passive or active mechanisms.

The last phase of standard controlled structures design is active structural control. This implies the use of a variety of sensors and actuators to significantly affect the plant dynamics. The general objectives of this level of control are to either add targeted damping or even to control the shape of a structure through active feedback and actuation. Active structural control at a system-wide level typically requires large amounts of computer processing capacity and several high authority actuators such as piezoelectric active struts. Active structural control is usually used only as a last resort since it is the most complex and resource demanding of the techniques.

The interferometry mission adds one more specific technique to the general CST toolbox: pathlength compensation. The need for delay lines in an interferometer provides a natural method for compensation of pathlength error. By sensing the error at the detector, a feedback controller can actuate a small mirror mounted on a piezoelectric stack in the PCD, thus adjusting the pathlength over a stroke of about 6 μm. With an additional voice coil stage, the PCD can easily achieve high frequency actuation over a range of a few millimeters. Devices have currently been built that can achieve an attenuation of more than 20 dB up to about 80 Hz, and give some attenuation out to 500 Hz [33].

4.2.4 Estimation of Spacecraft Structural Control Needs

Figure 4-6 shows the power spectrums of the DPL error for a staged application of CST techniques. The lines in the plot mark the open loop (ζ=0.001) response, the response

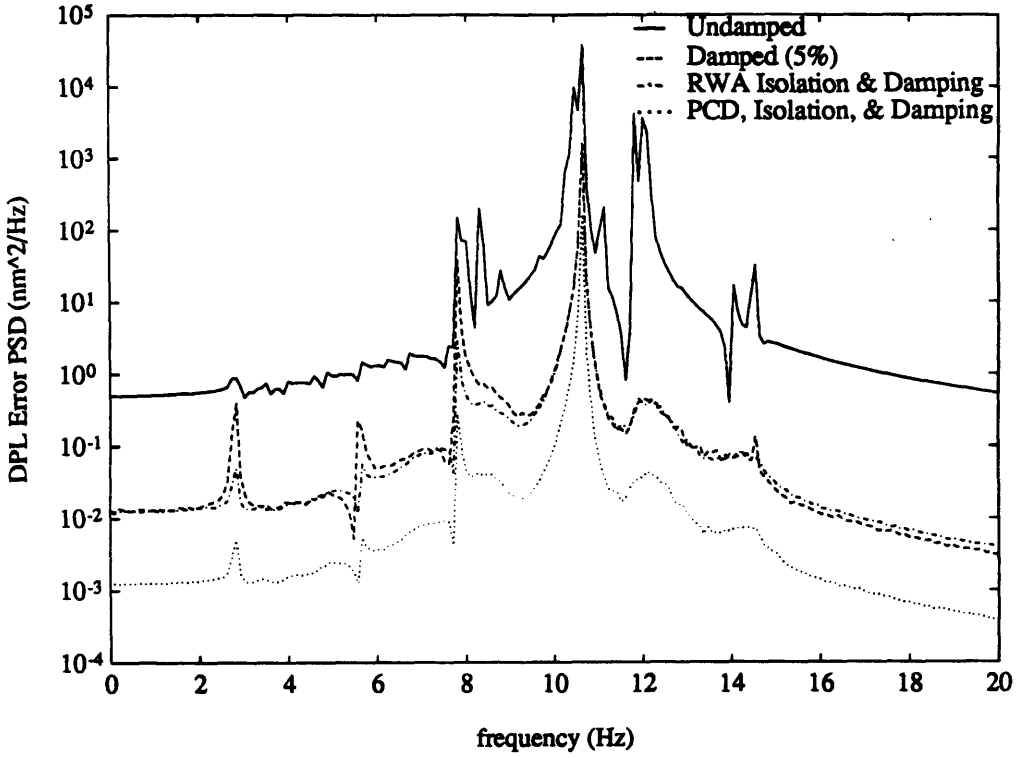

Figure 4-6 Differential Pathlength Error Power Spectrums for Staged Application of CST Techniques

with a damping ratio of 0.05, the addition of 10 dB isolation to the RWA disturbance, and the addition of the pathlength controller. The open-loop, undamped response yields an RMS error of 11.07 nm. To achieve specifications, a reduction of approximately 24 dB is required in the system. The response of the damped system (ζ=0.05), shown by the dashed line, yields an RMS error of just 1.88 nm, for a 15.4 dB reduction. Addition of isolation to the reaction wheel mounts only brings the RMS response down to 1.85 nm. The reason for the relatively small amount of reduction is that the isolation does not affect the dominant disturbance, the 10 Hz siderostat motion. Even though the RMS level does not drop by much, there is a noticeable effect on the remaining peaks in the response, which are driven by the RWA's. The remaining response is only 8.2 dB above the specification, well within the capability of the PCD compensator. The last line on the plot shows the response with ζ=0.05, 10 dB isolation at the reaction wheels, and 10 dB reduction with the PCD. The resulting RMS error is just 0.586 nm.

For the system response capable of being estimated by this model, the only control techniques required are a medium level of global damping and the PCD controller. For the actual interferometer, high levels of precision must be met out to about 1000 Hz. This is twice the bandwidth of the currently operating PCD's, so additional techniques are probably necessary. Damping is effective a high frequencies, but isolation should provide

the best attenuation for high frequency disturbances which can be expected to come mainly from the RWA's. These three treatments are probably the minimum necessary to achieve the performance goals, but to allow a design margin, it is assumed that 12 active components are available for use in the structure to add active damping or to provide shape control. Allowances are made for the needs of these control techniques in the sizing of the power subsystem and the computer processing system.

4.3 Thermal Control Analysis

The system thermal design is addressed in two stages. The first involves estimating the internal power dissipation and determining the amount of radiator area required to efficiently dispose of this heat. The required operating temperatures of a variety of components are specified, and the transient eclipse effects are examined. In the second stage, the detailed modelling of the thermal control for the optical elements is addressed. A general approach to achieve the required control limits is described and then applied to one of the elements as an example. The example takes into account shadowing effects at all allowable spacecraft orientations in assessing the thermal performance of the system. The section concludes with a brief discussion of the expected impact of thermal variations on the structural elements, with a focus on estimating what this implies for the optics in terms of control authority.

4.3.1 Requirements Specification

The allowable operating temperatures for various spacecraft components are listed in Table 4-1. Most of the estimates for general equipment are taken from [1], and the data for the optical elements are from [23,29]. The entries in the first part of the table are common to most spacecraft, and generally do not present much of a challenge for thermal design. The tightest requirements in this group are for the batteries which have a tolerance of about ±5 °C, and will probably require active heating elements. By far the most stringent requirements overall are for the payload optics and the metrology system. The specification for the payload optics is found by assuming a tolerance of 10 nm variation in the surface dimension which is on the order of tens of centimeters. Using ultra-low expansion (ULE) glass with a thermal coefficient of 3×10^{-8} m/m/K [29], the resulting control level is approximately 0.5 degrees. The metrology optics need to measure the variation of the structure to a fraction of the allowable pathlength error, but the elements are about a centimeter in size. Assuming a maximum variation of 0.1 nm, the allowable short term

term temperature variation is about 0.1 degree. Both of these specifications are unusually tight and will require a significant level of control. It should also be noted that to control temperature to 0.1° requires sensing temperature to a precision of about 0.01°

Table 4-1 Allowable Operating Temperatures for Spacecraft Components

Component	Temperature Range (°C)
General Electronics/Computers	+5 - +40
Antennas	-150 - +90
Solar Arrays	-160 - +70
Batteries	+5 - +20
ACS Sensors	-30 - +50
ACS Actuators	+1 - +50
Propellants	-10 - +20
Beam Combiner & Detectors	-23 ± 50
Primary Optics	+25 ± 0.5
Metrology Elements	+25 ± 0.1

4.3.2 Thermal Design Approach

The approach taken in spacecraft thermal design is largely a function of the level of control needed by the components and of the environmental characteristics of the spacecraft's orbit and orientation. Spacecraft with relatively constant attitude with respect to the sun and larger operating temperature tolerances require only simpler forms of thermal control. They usually can meet specifications with a combination of radiators, insulation, and tailoring of surface optical properties. Spacecraft with tight temperature tolerances or widely varying attitude must use more sophisticated techniques including active control and variation of optical properties. In general, the tendency is to apply techniques in stages, using passive methods first since they are simple, reliable, and do not consume resources such as power. Only if the passive techniques are insufficient to meet the control limits are more complicated means used. The interferometer design adheres to this standard in the application of thermal techniques, and in keeping with the minimization of vibrational disturbances, the emphasis is placed on methods that are not mechanically active.

The first step in thermal design is to separate the spacecraft into elements that can be modelled as essentially isothermal. These represent control volumes into which solar flux and earth flux flow, and from which heat is radiated. Due to the low thermal conductivity

of the graphite/epoxy struts, the group of components at each vertex and at each siderostat are modelled as isothermal nodes. For each node, the total net flux into the volume must be determined as a function of orientation. The equilibrium temperature can be determined, and if it is above the allowable limit, a radiator must be added to the node. To control the effects of solar and earth flux, absorptance to emittance ratio (α/ε) can be varied for each face of the volume. If this proves insufficient, multi-layer thermal insulation (MLI) can be added to reduce the variations in temperature by adding a very low conductivity barrier in the heat path. The last passive technique available is to use phase change materials. These act by absorbing or releasing heat through a (usually) solid-liquid phase change. The effect of this device is to add a large thermal inertia to the node. Beyond these methods, semi-passive techniques must be used. These include the use of louvers for varying surface optical properties and the use of heat pipes to create high conductivity paths for moving heat from points of very high heat flux. The most direct form of thermal control is the use of resistive heaters to add heat to the node as needed. Combined with active feedback control, this method provides the highest level of control possible. If sufficient power is available, heaters are often the first elements used because of their simplicity and accuracy. The techniques discussed here are usually used in the order described, with the exception of heaters as noted.

4.3.3 General Equipment Design

Solar Arrays: The thermal design of the solar arrays focuses on the operating temperature and on the area required for the shunt dissipators that dissipate excess power. Since the solar cell voltage is highly dependent on temperature, it is necessary to ensure that the arrays operate within acceptable bounds. The minimum temperature (usually occurring at the end of an eclipse) is important for the detailed design of the power control system, since large voltage spikes can result from the sudden illumination of cold cells. To determine the array operating temperature, the effective array absorptance must be determined. Since a fraction of the energy absorbed by the array is converted to electrical power, the effective absorptance is a function of the cell efficiency, η, and the fill-fraction, F, of the array:

$$\alpha_{se} = \alpha_s - F\eta \qquad \text{Eq. 4-5}$$

with a nominal absorptance of 0.8, a fill-fraction of 0.95, and an efficiency of 0.11, the effective absorptance is then 0.6955. The operating temperature can now be found from:

$$T_{op} = \left(\frac{\alpha_{se} A_f S \cos\theta}{(\varepsilon_f A_f + \varepsilon_b A_b)\sigma} \right)^{1/4} \qquad \text{Eq. 4-6}$$

where A_f and A_b are the array front and back areas, ε_f and ε_b are the front and back emittances, S is the solar constant of 1353 W/m^2, θ is the sun angle from the array normal, and σ is the Stefan-Boltzmann constant. Accounting for blockage from truss members, the array back area is 46.4 m^2. With an array front area of 53.6 m^2, a front emittance of 0.8, and a back emittance of 0.7, the maximum array operating temperature is 56.6 °C at a sun angle of 0°. This is well within specifications. The minimum normal operating temperature occurs at 70° sun angle, just as the cell is about to shut off. The equilibrium temperature at this angle is -20.9 °C. The array will get colder than this as it reaches 90° sun angle or during an eclipse, but the cells will not be functioning during those periods. The coldest the array will get occurs at the end of an eclipse period that begin with the array at 90° sun angle. The initial temperature for this eclipse would be about -158 °C. The equilibrium temperature during eclipse can be found from equation 4-6. Assuming 10 W are dissipated in the array during the eclipse, the equilibrium temperature, T_E, is -233 °C. The time constant of the response is found from:

$$\tau = \frac{mc_p}{4\sigma\varepsilon A T_E^3} \qquad \text{Eq. 4-7}$$

For an array mass of 33.6 kg and specific heat, c_p, of 700 J/kg·K, the time constant is 359 minutes. The time and temperature of a radiatively cooling body are then given by:

$$\frac{t}{\tau} + C = 2\left(\coth^{-1}\frac{T}{T_E} - \cot^{-1}\frac{T}{T_E} \right) \qquad \text{Eq. 4-8}$$

By inserting the initial conditions, the integration constant is found to be 0.0571. For the maximum eclipse period of 18.8 minutes, a minimum array temperature of -178 °C is found. This is 18 degrees below the allowable operating limit, but is probably acceptable for the worst case eclipse period.

The size of the shunt dissipator for each solar array panel is dependent on the maximum difference in power produced and power demanded and by the allowable temperature of the radiator. This occurs when the solar panel is at zero degrees sun angle where it produces 3759 W (BOL) and when only 990 W are demanded. The difference of 2769 W must be dissipated through a resistive network. The solar arrays are quite conveniently located for positioning the dissipators. Since the primary optics are prohibited

from facing the sun, the science plane face is the most efficient location for placing radiators. However, the radiators are constrained in location due to their possible impact on the payload optics. The radiators emit radiation in the infrared region, and the science mission requires collecting data up to 1 μm wavelength. In order to minimize the effect of the radiators on the payload, they are placed as far away as possible from the siderostat locations on each leg. The radiators are also sized at 2.44 m^2 (the equivalent of two triangular truss sections) each, resulting in a peak radiator temperature of 397 K and a flux intensity at 1 μm of 0.089 W/m^2.

Vertex Locations: The initial design issue for each vertex location is radiator sizing to account for waste heat. Table 4-2 summarizes the estimated values for heat dissipated by components in each vertex as well as the radiator area required. The sizing is made assuming a temperature of 290 K, slightly below room temperature. The more complex issue for these locations is how to deal with the widely varying solar fluxes associated with

Table 4-2 Estimated Power Dissipation By Spacecraft Components

Vertex 1 Component	(W)	Vertex 2 Component	(W)	Vertex 3 Component	(W)	Vertex 4 Component	(W)
RWA's	10	RWA's	10	RWA's	10	RWA's	10
Torquers	5	Torquers	5	Torquers	5	Torquers	5
Comm Elec	30	Comm Elec	30	Power Reg	400	C&DH	10
						Metrology	10
Area	0.14		0.14		1.29		0.11

the different spacecraft orientations. For the benefit of the sensitive optical components, each vertex is enclosed within a thermal shade made of composite material. In addition to limiting the transient effects of attitude changes, these plates also enhance the structural performance by stiffening the vertex locations. The effective area presented to the sun by the enclosed vertex varies from 2.12 m^2 to 4.9 m^2 depending on orientation. This means in a difference of about 2200 W in solar heat flux to the vertex. To maintain a heat balance, the α/ε ratio can be varied. By adjusting minimum and maximum surface temperature such that:

$$\frac{\sigma A_{tot} T_{max}^4}{A_{E_{max}} S} = \frac{\alpha}{\varepsilon} = \frac{\sigma A_{tot} T_{min}^4}{A_{E_{min}} S} \qquad \text{Eq. 4-9}$$

the required α/ε ratio is determined to be 1.7. This means, however, that the minimum and maximum surface temperatures are -8 °C and 53 °C which are outside the bounds specified for most of the relevant electronic equipment. These specifications are met by adding layers of MLI as determined by:

$$\Delta x = \frac{kA}{Q} \Delta T \qquad \text{Eq. 4-10}$$

where Δx is the required thickness and k is the effective thermal conductivity of MLI (≤ 0.001 W/m·K). For the vertices, five plys of 2 mil thickness MLI prove more than adequate to ensure the temperature remains within the specified bounds for electronic equipment. Components that require tighter temperature limits, such as batteries, can be enclosed within another volume inside the vertex, with additional thermal insulation and even heating elements if necessary.

Propellant Tanks: Propellants have a fairly stringent temperature limit, since N_2O_4 freezes at -11 °C and boils at 21 °C. Fortunately, the propellant tanks can be positioned in the near legs close to the fourth vertex in such a way that they are almost never eclipsed. With densities of 1440 kg/m^3 for N_2O_4 and 870 kg/m^3 for MMH, the required spherical tank radii are 0.42 m and 0.47 m respectively. For an illuminated sphere, equation 4-9 reduces to:

$$\frac{\alpha}{\varepsilon} = \frac{4\sigma T^4}{S} \qquad \text{Eq. 4-11}$$

For the median temperature of 5 °C, the desired α/ε is 1.0. With the addition of MLI and a heating element for use during eclipse periods, the propellant tanks can be maintained at the proper temperature.

4.3.4 Optical Element Control

The most challenging part of the thermal design is for the optical elements. The extreme levels of control specified (0.5 and 0.1 degrees) require the use of several different stages. The key to maintaining tight thermal control in general is to define a small control volume and tailor its properties such that it has a slight negative bias in heat flux into the volume. A resistive heating element is then added that can be switched on and off subject to feedback control. Design effort should be devoted to applying passive techniques to minimize the

amount of power required by the heating element to perform its job. Unfortunately, the interferometer is permitted such a variety of different orientations, and the siderostats require such a large volume, that the variations in heat flux are quite large. The following discussion illustrates a multi-staged approach to achieving the required level of control with one of the siderostat assemblies.

Each siderostat is enclosed within a thermal shield mounted on the truss structure. The inside face of the science plane truss legs are covered by the solar arrays, and the remainder of the shielding is graphite/epoxy plate. The only openings in the enclosure are a large hole in the science plane face for the incoming starlight, and a smaller hole for the light coming out of the beam compressor on its way to the FST mirrors and PCD. Since the temperature bounds are so tight, it is assumed that the interior of the enclosure is isothermal at 25 °C. Based on this assumption, the following analysis determines the net heat flux into the enclosure for all possible spacecraft orientations. The method taken in the analysis is to vary the sun vector in five degree increments through 90° of elevation and 360° of azimuth in the same way described in the power subsystem design in section 3.4.2. In low earth orbit, earth albedo and thermal flux amount to about 7% of the solar flux, so for each sun vector, the vector to the center of earth is also defined. Because of the nature of the orbit, the mean earth vector must be in a plane perpendicular to the sun vector. The earth vector is varied over 360°, and the values for minimum and maximum flux are recorded. The words minimum and maximum hereafter refer to the minimum and maximum over the variation of the earth vector. If the angle between the sun or earth vector and a face normal is greater then 90°, the corresponding flux is set to zero. For the face of the enclosure covered by the solar array, the array operating temperature for that orientation is used as the surface temperature. Shadowing effects of the solar arrays are included in the analysis. It does not really matter which siderostat is modelled because all orientations are possible due to the rotation about the line of sight. Since thermal time constants tend to be on the order of half of the LOS rotation duration, the steady state solutions for each position are significant To maintain the assumed 25 °C temperature, the net flux must be counteracted at every orientation.

The first step in the design process is to alter the α/ε ratio as was done for the vertices and the propellant tanks. The best performance with this tool is achieved with α/ε of 7.5, α equal to 0.3, and ε equal to 0.04. The minimum and maximum net fluxes averaged over azimuth and elevation are -27 W and 82 W respectively. These values seem quite reasonable, however the range between the peak maximum and peak minimum net fluxes is unacceptably large at over 1700 W. The next step is to vary the optical properties of each face in an effort to reduce the range of the fluxes. The best case for this step is

attained by setting the two end faces to an α/ε of 2.8, the solar array face to 0.23, the science plane face (which never faces the sun) to 7.5 and the remaining face to 1.17. This stage of thermal control succeed in reducing the range of heat fluxes to about 1100 W, and the mean values are -18 W minimum and 58 W maximum. The third step is to use MLI. To determine the heat flux into the enclosure through the insolation, the inside and outside temperatures must be found by numerically solving simultaneous fourth order equations. Figure 4-7 shows the effect of adding layers of MLI to the enclosure with tailored α/ε ratios. The peak minimum, peak maximum, and range of the fluxes are plotted against the number of layers of MLI. Obviously, there is a trend of diminishing returns for added

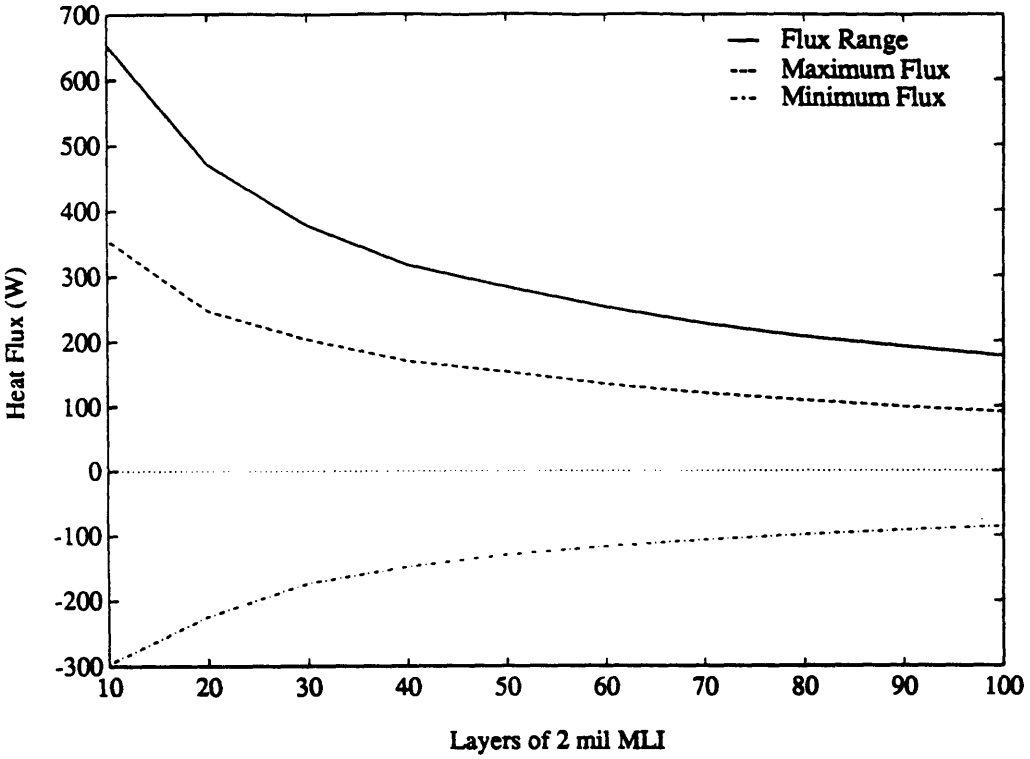

Figure 4-7 Change in Net Heat Flux into Siderostat Enclosure as Function of Layers of MLI

layers. Choosing 50 layers as the approximate breaking point, the range is reduced to 276 W with average fluxes of -34 W minimum and 0.1 W maximum, and peak fluxes of -130 W and 145 W. Figures 4-8(a-b) show the resulting contour and three-dimensional scale plots for the net flux using 50 layers MLI.

Although these numbers are much more reasonable, it still seems unacceptable to demand up to 130 W for each siderostat from the power system. Fortunately, there is still another entirely passive method available: phase change material. By adding a sufficiently

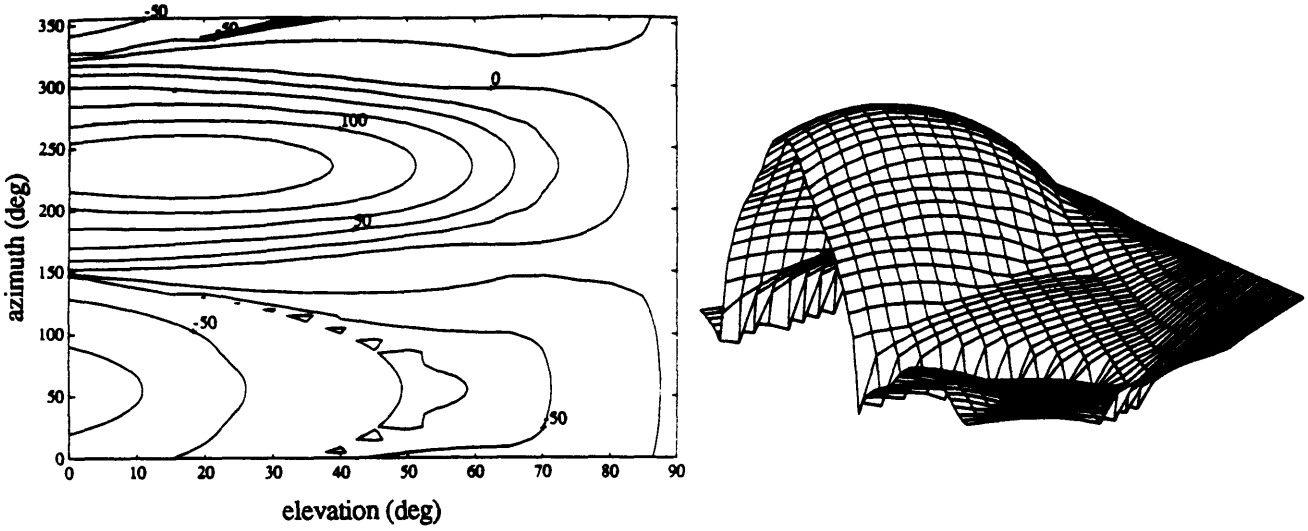

Figure 4-8 (a) Net Heat Flux Contours for Siderostat Enclosure with Tailored α/ε and 50 Layers MLI (b) 3-Dimensional Scale Plot of Net Heat Flux Contours

large thermal inertia, the large variations in flux are mostly absorbed in the solid-liquid transition of the material. The most common material used for phase change thermal control is paraffin because of its combination of useful melting point and large heat of fusion. With a heat of fusion of 1.5 kJ/kg, the amount of material needed to absorb a peak of 150 W over the nominal mission time of 13 hours is 46.8 kg per siderostat, for a total of 375 kg. This requires a high conductivity thermal path between the optical elements and the paraffin. Lastly, to maintain the temperature within a fraction of a degree, a heating element consuming up to 50 W peak is included.

Thus, the solution to the problem of very precise thermal control in the face of widely varying spacecraft attitude is to use a multi-staged approach including tailoring of surface α/ε, addition of insulation material , and the use of phase change materials. Note that the objective has been achieved without the use of any mechanical actuation as desired. The finest levels of control for the metrology can be attained by providing them with an additional enclosure to further reduce the effect of varying environmental factors.

The last point to address in analyzing the thermal control of the optical system is thermal effects of the structure. Due to eclipse effects and shadowing, there are periods when an entire leg of the truss may move from full illumination to compete shadow. The interesting question is how much this may affect the structural deformations. Applying equation 4-9 to the 1.68 m struts, the maximum equilibrium temperature is found to be 30 °C, meaning that the maximum temperature variation possible is 303 K. Using composites technology developed for HST, coefficients of thermal expansion as low as

1.4×10^{-8} m/m/ °C can be attained [21]. With the maximum possible change in temperature of 300 degrees, the change in strut length is just 7.1 μm, or less than 0.15 mm over the length of the entire truss leg. This indicates that a stroke capacity of several millimeters in the pathlength controllers is more than adequate to compensate for thermal deformations.

4.3.5 Subsystem Summary

The very stringent requirements for thermal control demanded by the sensitivity of precision optical components has been met without the use of any mechanical or fluid actuation. Passive techniques are capable of bringing the heat loads within reasonable levels so that active electrical heating elements can achieve the required accuracy of one tenth of a degree. Simpler passive techniques are sufficient for maintaining heat balances of other typical components such as electronics, batteries, and propellants. Assuming specific masses of 0.25 gm/in^2 for the thermal insulation, 3.4 kg/m^2 for the thermal shield material, and 5.4 kg/m^2 for the radiators, the mass of the system can be estimated. The total mass and power estimates for the subsystem are shown in Table 4-3.

Table 4-3 Mass and Power Estimates of the Thermal Subsystem

Component	Quantity	Mass (kg)	Power (W)
Multi-Layer Insulation	167 m^2	64.7	-
Radiators	16.3 m^2	88.3	-
Thermal Shields	167 m^2	567.8	-
Thermal Inertia	8	375	-
Heaters	14	28	420
Sensors		5	10
Total		1123.8	430

Chapter 5
Conclusions and Recommendations

The SERC Interferometer testbed project has provided an unusual opportunity to utilize spacecraft system design techniques in a research-oriented, academic environment. The experience gained in this exercise will prove valuable in future work in the "real" engineering world. While the primary purpose of this thesis has been the experience in systems design, it has also served as a vehicle for examining the impact of blending controlled structures objectives with traditional spacecraft design issues. Probably the most relevant lesson of this work for the researcher in CSI is an understanding of how his or her goals will strongly affect the basic assumptions that are typically involved in spacecraft design. While those assumptions have not actually changed, their priority or order of importance has been shuffled.

5.1 Impacts of Structural Control Objectives on System Design

The extremely difficult requirements prescribed by the interferometric mission for the structural control subsystem force sacrifices in other subsystems. The CSI design concerns significantly affected design decisions in almost every major subsystem presented in this thesis. The basic structural configuration itself was chosen primarily for its structural dynamic properties, rather than its ease of construction and deployment. In fact, deployment is probably the only area that actually forced a concession from the structural control objectives in requiring a smaller truss cross-section in order to fit within the available launch vehicle payload volume. Both the orbital design and the spacecraft payload configuration were tailored to suit the needs of vibration suppression. The orbit was selected as a sun synchronous, twilight orbit so as to minimize the occurrence of thermal transients in the system. The configuration of the payload was altered from three moving siderostats to eight stationary ones. This decision cost the total system in terms of mass and power, but saved the structural control system the trouble of counteracting large,

motion induced vibrations and of tracking the primary optics with the metrology system. The decision to use eight siderostats also eliminated the most complex attitude control maneuvers, but at the cost of limiting the maximum achievable performance of the system.

In the detailed subsystem design, two primary principles guided all trade decisions: 1) minimization of mechanical noise was the primary decision factor in component selection, and 2) the spacecraft was not seriously constrained either in mass or volume. This latter principle frequently permitted the exercise of the first with relatively small cost to the entire system. Of the subsystems discussed in Chapters 3 and 4, only the propulsion section was left unaffected by the vibration control objective. The attitude control system was forced to incorporate magnetic isolation mounts and smoothed torque commands in order to enhance mission performance. The command and data handling system was dominated by the structural control tasks. One third of the data storage requirements for each image were related to measuring the vibration errors, and over half of the processing speed was devoted to applying structural or pathlength control. Both the communications and power subsystems sacrificed small amounts of mass and cost for the benefit of eliminating antenna gimbal and solar array drive motors and their associated appendages. The thermal system as well was strongly influenced by the desire to eliminate noise sources. Thermal louvers could have been used with the thermal enclosures rather than phase change material, but louvers must be mechanically actuated. Consequently, about 300 kg additional mass was added to the system, rather than introduce a noise source.

System designers and CSI researchers alike should be aware that the second principle mentioned above is generally the exception rather than the rule for spacecraft design. More typically, the CSI engineer will have to demonstrate significant improvements in performance in order to justify some of the penalties assumed in this design.

5.2 Recommendations for Future Work

As with any study that attempts to address a large number of topics at a fairly high level, there numerous subjects that warrant more detailed study. Only a few of these are of real importance to the SERC Interferometer project, and are discussed here.

1. There are currently a broad range of concepts for space optical interferometry being designed, presented, and discussed in the aerospace community. These range from lunar based instruments, to small astrometric oriented spacecraft, to shuttle bay instruments, and even separate free-flying telescopes. Only recently, as a decision on an

actual NASA flight project approaches, has an effort been made to sort out competing designs in the field. A very interesting project for a systems engineer would be to examine the different design concepts in an attempt determine quantitatively the relative advantages and disadvantages of different approaches. An important contribution to the SERC project in particular would be to gain a definite understanding of the benefits of the closed topology structure.

2. A second area of research concentrates on the SERC design of the spacecraft and its operation, particularly deployment. It would be interesting to determine if some modified version of the tetrahedral structure could provide similar structural and scientific performance in a smaller package, with the ultimate objective of using a smaller launch vehicle. The deployment process described in Chapter 2 raises several interesting questions of its own. The process involves motion through a very complex set of rotations, and the meeting of two beams in space. The topics of deployment control, mechanism design, and reliability could be addressed in this context. The last area of concern operationally is with the initial capture of the guide star by the control system. SERC does not currently have a good understanding of this problem, and could benefit from research in this area.

3. Another topic of interest to a systems engineer is how to test such a large structure once it is built, but before it is launched. Problems with HST have demonstrated how valuable testing of the full system can be, but do facilities exist to reliably test lightweight truss structures on the order of tens to hundreds of meters in length? Should on orbit system identification be planned for updating the plant model and controllers? Will the structural pieces all fit if they have not been tested on the ground first? If the structure cannot be tested, is it reasonable to base structural control on mathematical models all the way out to 1000 Hz? All of these are important questions that have relevance to the design and deployment of Space Station Freedom.

4. A somewhat more specific topic that should definitely be pursued is a more detailed modeling of the thermal behavior of the structure, in particular, the effects of thermal transients on structural vibration. The solar panels of HST once again call attention to a problem that has not been adequately investigated for this design.

5. As for actual experimental work with the SERC testbed, there are a number of issues that could be addressed. Real time system identification is one that has just recently been introduced to the project, and could provide insight to the questions raised in point 3,

above. Another useful project would be to generate more realistic time-varying disturbance signals for multiple locations on the structure. A final set of projects that would generate useful information would be the experimental identification of add-on's to the structure such as radiator panels or solar arrays. An experimental determination of the damping effects of actual multi-layer insulation on strut members may prove to be a way of addressing both damping and thermal control with the same material.

References

[1] Agrawal, B. N., Design of Geosynchronous Spacecraft, Prentice-Hall, Inc.: Englewood Cliffs, NJ, 1986.

[2] Aguero, R., "Preliminary POI Radiation Environment," Jet Propulsion Laboratory, Interoffice Memorandum 5217-91-77, Apr. 9, 1991.

[3] Allen, T. S., et. al., "FEAMIS: A Magnetically Suspended Isolation System For Space-Based Materials Processing", AAS-86-017, *Proceedings of the Rocky Mountain Guidance and Control Conference*, 1986.

[4] Bahcall, J. N., et. al.,"The Decade of Discovery in Astronomy and Astrophysics," National Research Council, National Acedemy Press: Washington, DC, 1991.

[5] Billerbeck, W. J. and Baker, W. E., "The Design of Reliable Power Systems for Communications Satellites," AIAA 84-1134, *AIAA/NASA Space Systems Technology Conference*, Costa Mesa, CA, 1984.

[6] Blackwood, G. H., Jaques, R. N., and Miller, D. W., "The MIT multipoint alignment testbed: technology development for optical interferometry," SPIE 1542-34, *SPIE Conference on Active and Adaptive Optical Systems*, San Diego, CA, 1991.

[7] Chen, H. S., Space Remote Sensing Systems: An Introduction; Academic Press, Inc.: New York, 1985.

[8] Crawley, E. F., 16.93 class notes: *Dynamics of Controlled Structures*, MIT, 1991.

[9] Dougherty, H., et. al., "Magnetic Control Systems for Space Telescope", *The Journal of the Astronautical Sciences*, Vol. XXX, No. 3, Jul-Sep 1982.

[10] Dougherty, H., Rodoni, C., Rodden, J., and Tompetrini, K., "Space Telescope Pointing Control", AAS-83-365, *Proceedings of the AAS/AIAA Astrodynamics Conference*, Lake Placid, NY, 1983.

[11] Eyerman, C. E., *A Systems Engineering Approach to Disturbance Minimization for Spacecraft Utilizing Controlled Structures Technology*, SERC #2-90, SM Thesis, Department of Aeronautics and Astronautics, M.I.T., 1990.

[12] Gates Aerospace Batteries, Product Brochure for NiH_2 Cells, Gates Energy Products, Gainesville, FL, 1991.

[13] Griffin, M. D. and French, J. R., Space Vehicle Design, American Institute of Aeronautics and Astronautics, Inc.: Washington, DC, 1991.

[14] Hasha, M. D., "Passive Isolation/Damping System for the Hubble Space Telescope Reaction Wheels," N87-29873, *The 21st Aerospace Mechanisms Symposium*, 1987.

[15] Ionasescu, R. and Sonnabend, D., "Shadow Limits for Sun Synchronous Orbits," in *The POINTS Instrument for TOPS: 1991 Progress Report*, Jet Propulsion Laboratory, Nov. 12, 1991.

[16] Jennison, R. C., Introduction to Radio Astronomy, Philosophical Library: New York, 1966.

[17] Kendig, J. R. and Davis, P., "Space-Qualified 1000 Foot-Pound-Second Magnetically Suspended Reaction Wheel Assembly (MSRWA)", AAS-81-023, *Proceedings of the Rocky Mountain Guidance and Control Conference*, 1981.

[18] Kurland, Richard and Stella, Paul, "Advanced Photovoltaic Solar Array Design and Performance," AIAA 92-1058, *Proceedings of the AIAA Aerospace Design Conference*, Irvine, CA, 1992.

[19] Laskin, R., Breckenridge, W., Shao, M., and Redding, D, "Calibration and Operation of a Large Space-Based Optical Interferometer", AAS-90-040, *Proceedings of the Rocky Mountain Guidance and Control Conference*, 1990.

[20] Laskin, R. A., "Focus Mission Interferometer 'Business-As-Usual' Design Document," Jet Propulsion Laboratory, D-6916, Oct. 31, 1989.

[21] McMahan, L. L., "Space Telescope Assembly Structural Materials Characterization," AIAA 82-1858, 1982.

[22] Meirovitch, L., Elements of Vibration Analysis, McGraw-Hill: New York, 1986.

[23] National Aeronautics and Space Administration, *"Optical Space Interferometer Flight System Design Status Report,"* Jet Propulsion Laboratory, 1991.

[24] National Aeronautics and Space Administration, Space Network (SN) Users' Guide, NASA Goddard STDN No. 101.2, 1988.

[25] National Aeronautics and Space Administration, *NASA Space Systems Technology Model,* 6th ed., 1985.

[26] National Oceanic and Atmospheric Administration, U.S. Standard Atmosphere, 1976, Washington, DC, 1976.

[27] National Research Council, "Working Papers: Astronomy and Astrophysics Panel Reports," National Academy Press: Washigton, DC, 1991.

[28] Reasenberg, R. D., "Microarcsecond Astrometric Interferometry," Workshop on High Angular Resolution Optical Interferometry from Space, *Bulletin of the AAS*, Vol. 16, No. 3 (Part II), 1984.

[29] Satter, C. and Miyake, R., "POINTS Preliminary Thermal Design," in *The POINTS Instrument for TOPS: 1991 Progress Report*, Jet Propulsion Laboratory, Nov. 12, 1991.

[30] Scholese, C., personal communication, Goddard Spaceflight Center, NASA, Mar. 14, 1991.

[31] Schumaker, B. L. and Ulvestad, J. S., "Candidate Launch Vehicles for POINTS," in *The POINTS Instrument for TOPS: 1991 Progress Report*, Jet Propulsion Laboratory, Nov. 12, 1991.

[32] Shao, M., et. al.,"Optical Interferometry in Space: Presentation to the Science and Technology Advisory Group," Jet Peropulsion Laboratory, Apr. 16, 1991.

[33] Shao, M., "Fast Delay Lines," presentation, 1991

[34] Shao, M., personal communication, Jet Propulsion Laboratory, Jun. 17, 1991.

[35] "Texas Instruments Demonstrates Solid-State Data Recorder," *Aviation Week & Space Technology*, Feb. 24, 1992.

[36] Titan III Commercial Launch Services Customer Handbook, Issue No. 1, Martin Marietta Commercial Titan, Inc., December, 1987.

[37] Titan IV User's Handbook, Revision A, Martin Marietta Astronautics Group, Denver, CO, August, 1990.

[38] Traub, W. A. and Carleton, N.P., "COSMIC: A High Resolution, Large Collecting Area Telescope," Workshop on High Angular Resolution Optical Interferometry from Space, *Bulletin of the AAS*, Vol. 16, No. 3 (Part II), 1984.

[39] Wertz, J. R. and Larson, W.J. editors, Space Mission Analysis and Design, Kluwer Academic Publishers: Boston, MA, 1991.

Appendix A
Spacecraft Mass and Power Listing

Table A-1 shows a fairly detailed listing of the SERC Interferometer spacecraft components together with their estimated mass and power requirements. The list is broken down into subsystem groups including structure, propulsion, attitude control, power, C&DH, communications, thermal, and payload. For each component, the number of units is listed with the total mass and total power. The fifth column shows the design margin used for each element. The margins vary significantly depending on the confidence in the mass and power estimates. For component data taken from existing product brochures, margins of only 5 to 10 percent are used, whereas for parts that are minor extrapolations of existing hardware, margins of 15 to 20 percent are used. Margins of 20 to 25 percent are used for components that require advanced development or for which sizing is only approximate. The sixth and seventh columns show the mass and power requirement with margin included, and the seventh column shows estimated peak power loads, including design margin. The last column contains any explanatory comments for the component, usually about either performance estimates or data references. The total mass and power for the spacecraft and payload are shown at the bottom of the table. The instrument subtotal makes up 16.1% of the total mass, and includes the payload and optics, the metrology system, and the science electronics. Other significant mass fractions are: 31.1% for the structure, 15.5% for propulsion, 11.8% for attitude control, 11.3% for thermal, and 9.5% for cabling.

Table A-1 SERC Interferometer Spacecraft Mass and Power Listing

DESCRIPTION	#	EST. MASS (kg)	EST. POWER (W)	MARGIN	MASS W/ MARGIN (kg)	POWER /W MARGIN (W)	PEAK POWER (W)	COMMENTS
STRUCTURE		*3251.10*			*3901.32*			
1.681 m Struts	1068	2509.80	-	20	3011.76	-		Gr/Ep space station type tubes
2.38 m Struts	114	302.10	-	20	362.52	-		Includes end fittings
Nodes	366	439.20	-	20	527.04	-		Al ball nodes (LaRC)
PROPULSION		*1844.53*	*10.00*		*1945.16*	*10.50*	*10.50*	
Apogee Kick Motor	1	829.00	-	5	870.45	-		STAR-37F; 779 kg prop; Isp=290.5 s
Thrusters	2	7.60	10.00	5	7.98	10.50	10.50	Marquardt Trusters
Fuel		839.93	-	5	881.93	-		N2O4/MMH; Isp = 309 s
Tankage and Connectors	2	168.00	-	10	184.80	-		
ATTITUDE CONTROL		*1256.20*	*694.00*		*1485.22*	*822.00*	*2271.20*	
Reaction Wheels	8	924.00	492.00	20	1108.80	590.40	2022.00	Improved HST RWAs
Magnetic Torquers	12	180.00	64.00	10	198.00	70.40	70.40	Ithaco (3600 Am^2)
Magnetometers	3	2.40	3.00	5	2.52	3.15	3.15	Ithaco
Star Trackers	2	30.00	20.00	5	31.50	21.00	21.00	Astros II
Sun Sensors	2	3.00	2.00	5	3.15	2.10	2.10	Adcole 16764
Fine Guidance Interferometer	2	86.80	72.00	25	108.50	90.00	90.00	0.4 m sid./beam comp./PCD (JPL)
Inertial Reference Unit	1	17.00	23.00	5	17.85	24.15	24.15	DRIRU II
Flight Computer	2	7.00	8.00	10	7.70	8.80	26.40	
Interface Electronics	2	6.00	10.00	20	7.20	12.00	12.00	
POWER		*353.80*			*420.07*			
Solar Arrays	6	101.00		15	116.15			Body mounted APSA Si arrays
Batteries	2	120.80		15	138.92			NiH2 (200 Ahr, 100% DOD)
Battery Control	2	12.00		25	15.00			
Power Distribution Assembly	2	92.00		25	115.00			Solid state power switches
Power System Electronics	2	28.00		25	35.00			

COMMAND & DATA		*35.04*	*39.10*		*38.54*	*43.01*	*101.36*	
Telemetry & Command Unit	4	33.00	26.50	10	36.30	29.15	88.00	
Mass Memory Unit	1	2.04	12.60	10	2.24	13.86	13.36	TI SSR, 3D packaging
COMMUNICATIONS		*79.98*	*60.00*		*97.74*	*69.00*	*151.50*	
Low Gain Antennae	2	3.00	-	20	3.60	-	-	
Phased Array Antennae	2	51.83	20.00	25	64.79	25.00	25.00	
Transponder	2	10.30	10.00	10	11.33	11.00	11.00	TDRSS Ku-Band
Power Amplifiers	3	3.60	30.00	10	3.96	33.00	115.50	Solid state
Coax		11.25	-	25	14.06	-		
THERMAL		*1128.80*	*280.00*		*1411.00*	*350.00*	*350.00*	
Multi-Layer Insulation		64.70	-	25	80.88	-	-	estimate at 0.25 gm/in^2
Radiators		88.30	-	25	110.38	-	-	
Heaters/Thermostats		28.00	270.00	25	35.00	337.50	337.50	
Thermal Shields		567.80	-	25	709.75	-	-	
Thermal Inertia		375.00	-	25	468.75	-	-	
Sensors		5.00	10.00	25	6.25	12.50	12.50	
CABLING		*950.00*	-	*25*	*1187.50*	-	-	10% spacecraft mass
MECHANISMS		*29.50*	*0.00*		*36.88*	*0.00*	*0.00*	
Hinge Actuators	8	16.00	-	25	20.00	-	-	
Latches	9	13.50	-	25	16.88	-	-	
PAYLOAD & OPTICS		*1571.47*	*480.00*		*1964.34*	*600.00*	*600.00*	
Siderostats	8	633.35	160.00	25	791.69	200.00	200.00	120 kg/m^2 optics + 20% structure
Beam Compressor	8	443.34	50.00	25	554.18	62.50	62.50	79 cm dia primary + structure (20%)
Steering Mirrors	40	10.28	60.00	25	12.85	75.00	75.00	JPL
Active Delay Lines	8	169.50	200.00	25	211.88	250.00	250.00	JPL (includes processor)
Beam Combiners	30	315.00	10.00	25	393.75	12.50	12.50	

METROLOGY		*23.00*	*40.00*		*28.75*	*50.00*	*50.00*	
Laser Distribution	1	5.00	20.00	25	6.25	25.00	25.00	
Beam Launchers	66	16.50	20.00	25	20.63	25.00	25.00	
Corner Cubes	15	1.50	-	25	1.88	-	-	
SCIENCE ELECTRONICS		*20.00*	*40.00*	*10*	*22.00*	*44.00*	*44.00*	
SPACECRAFT SUBTOTAL		**8928.95**	**1083.10**		**10523.43**	**1294.51**	**2884.56**	
INSTRUMENT SUBTOTAL		**1614.47**	**560.00**		**2015.09**	**694.00**	**694.00**	
FLIGHT SYSTEM TOTAL		**10543.42**	**1643.10**		**12538.51**	**1988.51**	**3578.56**	

Appendix B

Estimation of Processing Requirements

The processing and storage requirements for C&DH subsystem are broken down into six categories as described in section 3.2. The requirements of the science data processor, which were described in detail in section 3.2, are not discussed here, rather the focus is this kept on the other subsystem processing needs. The procedures used for estimating these needs are largely taken from chapter 16 in reference [39] which provides good first order estimates for storage and processing for communications, attitude control, subsystem management, and operating system execution. Processing needs for global structural control and optical pathlength control are estimated based on state-space Kalman filtering techniques.

Table B-1 summarizes the memory and throughput estimates for attitude control, communications, and subsystem housekeeping as derived from [39]. The standard assumptions made here are a 1750A class, 16 bit target computer operating with high-level software such as Ada. The estimated throughput is directly proportional to the frequency of operation for the task. The final system estimate includes a 100% design margin to account for requirements uncertainty and on-orbit spare.

For structural control, the processing requirements can be determined in floating-point operations per second (flops) by assuming a Kalman filter process and estimating the number of states, controls, and measurements. By assuming sensor measurements of 16 various accelerometers, 8 pathlengths, and 33 laser legs, the total number of measurements, M, is 57. With 16 fast steering mirrors and an estimated 24 other actuators (isolation mounts or active struts), the number of controls, P, is 40. Finally, if 8 states per optical train are assumed, this gives a total of 64 states, N. The computations per iteration are derived as:

$$C = N(2N + 4M + 4P - 3) - P \qquad \text{Eq. B-1}$$

This equation yields 32792 operations per iteration. If the global control system is operating at an estimated 1000 Hz (half the optical pathlength controllers), the required processing speed is 32.8 Mflops. For sizing with the rest of the system, the structural control must be specified in KIPS. Using reference [39] again, ones finds that a Kalman filter running at 1000 Hz on a 1750A requires approximately 10 MIPS of throughput, 8 K of code memory, and 1 K of data memory. With a 100% design margin these values become 20 MIPS, 16 K, and 2 K respectively.

Table B-1 Estimates of General Spacecraft Processing Tasks

Component	Frequency (Hz)	Code Memory (K words)	Data Memory (K words)	Throughput (KIPS)
Attitude Control				
Rate Gyro	10.0	0.8	0.5	9.0
Sun Sensor	1.0	0.5	0.1	1.0
Star Tracker	0.01	2.0	15.0	2.0
Magnetometer	2.0	0.2	0.1	1.0
FGI	10.0	1.0	0.5	9.0
Kinematic Integration	10.0	2.0	0.2	15.0
Error Determination	10.0	1.0	0.1	12.0
Magnetic Control	2.0	1.0	0.2	1.0
RWA Control	10.0	1.0	0.3	25.0
Ephemeris Propagation	1.0	2.0	0.3	2.0
Orbit Propagation	1.0	13.0	4.0	20.0
ACS Subtotal		*25.5*	*21.8*	*98*
Communications				
Command Processing	10.0	1.0	4.0	7.0
Telemetry Processing	10.0	1.0	2.5	3.0
Data Processing	10.0	1.0	2.5	3.0
Antenna Control	2.0	1.0	0.2	1.0
Communications Subtotal		*4.0*	*9.2*	*14*
Subsystems				
Autonomous Functions	10.0	15.0	10.0	20.0
Fault Monitors	5.0	4.0	1.0	15.0
Fault Correction	5.0	2.0	10.0	5.0
Power Management	1.0	1.2	0.5	5.0
Thermal Control	0.1	0.8	1.5	3.0
Subsystems Subtotal		*23.0*	*23.0*	*48*
Design Margin		*52.5*	*54.0*	*160*
Computer Requirements		*105*	*108*	*320*

The C&DH system has two independent executive processors to control the distribution of the processing tasks among the parallel CPU's. Each of these requires an operating system capable of handling the full processing load for the system. To estimate the executive processing load, the total number of tasks per second and the amount of data per second must be estimated. The number of tasks per second is the total of each function's frequency in Table B-1 times an estimated 4 tasks per function, plus approximately 8000 tasks per second for the structural controller for a total of 8440. The PCD's are not included since they are independent units. The estimated throughput for the executive is 2.53 MIPS. To handle input/output tasks, the throughput is estimated at 0.05 times the number of words per second. The communications, attitude control, and subsystems tasks produce an estimated 8800 words per second, and the structural controller about 50,000, requiring a total of 2.94 MIPS to transfer the data. Each executive processor must then have about 6 MIPS of throughput capacity, along with about 16 K for code memory and about 8 K for data memory as estimated from reference [39].

The requirements for the pathlength controllers can be approximated in a similar way to those of the global structural controller. Each PCD has two controls (a piezo-actuator and a voice coil), one measurement (the pathlength error), and an estimated four states. Using equation B-1 yields 66 flops per iteration, and 132 Kflops at 2000 Hz. Scaling the throughput derived for the structural controller, the requirements for each controller are 80.5 KIPS, 8 K code memory, and 1 K data memory. In addition, a local executive is needed. To handle an estimated 2000 task per second, the executive requires 600 KIPS, and to handle about 4000 words per second requires and additional 200 KIPS. With executive memory requirements as described in the previous paragraph and a 100% design margin, the requirements scale to 1.76 MIPS, 48 K, and 18 K.

To summarize the estimated requirements, the total processing load is divided between the system executives, the PCD controllers, the science data processor, and the general purpose computers which handle the communications, attitude control, housekeeping, and global structural control. The system executives require approximately 6 MIPS throughput and 24 K memory each. Each PCD controller needs about 1.8 MIPS throughput and 66 K memory, and the general computers needs a total of 20.32 MIPS and 231 K memory. The science data processor tasks are described in detail in the main text.

Appendix C
Communications Link Calculations

Table C-1 shows the spreadsheet used to calculate both the phased-array and omni antenna communications links. The primary reference for these calculations is the TDRSS Users' Guide [24]. Shaded rows indicate parameters that are set as adjustable performance parameters from which the remaining cells are computed. The values shown are those for the system at nominal performance level. The frequency band and frequency are those given in [24]. The data volume and storage are taken from the command and data handling section. The maximum transmission time is the performance parameter that is adjusted in the design process, and is defined as that required with an antenna steering angle of 60°. The average and the minimum times are for the average and zero steering angles respectively. The bit error rate is held constant as per the requirement. Other analysis showed that transmitter power and transmission time were relatively insensitive to BER. The data rates are simply the data volume divided by the appropriate transmission time. The required bandwidth is computed from the Shannon limit below, with C/N set at 16 dB which is 3.5 dB over the E_b/N_0 required. The KSA service has up to 50 MHz bandwidth available.

$$B=R_{max}\left(\log_2\left(1+\frac{C}{N}\right)\right)^{-1} \qquad \text{Eq. C-1}$$

The antenna diameter and efficiency are specified parameters, as is the antenna loss (L_t). The beamwidth and antenna gain are computed from the standard equations.

$$\Theta_{3dB}=1.25\frac{\lambda}{d} \qquad \text{Eq. C-2}$$

$$G_t = \frac{4\pi A_e \eta}{\lambda^2} \qquad \text{Eq. C-3}$$

Table C-1 Communications Link Spreadsheet

Parameter	Units	Phased Array	Omni	Comments/Reference
Frequency Band		Ku	Ku	TDRSS Single Access Band
Frequency	GHz	15.0034	15.0034	TDRSS Guide
Data Volume	bits	4.50E+09	4.50E+09	specified
Data Storage		3-D SSR	3-D SSR	
Max. Transm. Time	min	20.00	20.00	Set for largest steering angle
Ave. Transm. Time	min	16.48	-	Set for average steering angle
Min. Transm. Time	min	10.00	-	Set for zero steering angle
Bit Error Rate		1.00E-06	1.00E-06	specified
Data Rates	bps			
- Minimum		3.750E+06	-	Data Vol. / Max. Transm. Time
- Average		4.551E+06	-	Data Vol. / Ave.Transm. Time
- Maximum		7.500E+06	1.000E+03	Data Vol. / Min. Transm. Time
Bandwidth	MHz	1.40	0.00	Shannon's Limit C/N = 16 dB
Antenna Diameter	m	0.971	0.971	specified
Antenna Efficiency		0.55	0.55	from W&L
Beamwidth (3 dB)	deg	1.47	1.47	1.25 lambda / diameter
Antenna Gain	dBw	41.08	0.00	equation
Antenna Loss	dBw	-1.00	-1.00	specified
Required Eb/No	dBw	12.5	12.5	(QPSK) + 2 dB
"K" Factor	dBw	240.00	240.00	from TDRSS Guide
Ideal Power Rcvd.	dBw	-171.25	-210.00	equation from TDRSS Guide
Ant. Pointing Error	deg	0.5	0	specified
Pointing Error Loss	dBw	-1.38	0.00	
Polarization Loss	dBw	-0.5	-0.5	specified (TDRSS Guide)
RFI Losses	dBw	-0.5	-0.5	specified (TDRSS Guide)
Non-Compl. Losses	dBw	-0.5	-0.5	specified (TDRSS Guide)
Pred. Power Rcvd.	dBw	-168.37	-208.50	equation from TDRSS Guide
Max. Range	km	44748	44748	
Min. Range	km	35086	35086	
Max. Space Loss	dBw	-208.99	-208.99	equation from TDRSS Guide
Min. Space Loss	dBw	-206.88	-206.88	
Max. Required EIRP	dBw	40.62	0.49	equation from TDRSS Guide
Min. Required EIRP	dBw	38.51	-1.62	
Link Margin	dBw	6.00	6.00	specified
Max. EIRP	dBw	46.62	6.49	Req. EIRP + Margin
Min. EIRP	dBw	44.51	4.38	

Max. Transm. Power	W	4.51	5.61	
Min. Transm. Power	W	2.77	3.45	
Solid State Amp				
Max. P Efficiency	Est.	0.25	0.25	
Min. P Efficiency	Est.	0.2	0.2	
Max. Input Power	W	27.66	31.75	
Min. Input Power	W	21.06	23.64	
S. S. Amp Mass	kg	1.20	1.20	No Margin
Antenna Mass	kg	11.78	11.78	2 x Intelsat V C-band 1.5 dia an
Transponder & Elec.	kg	10.30	10.30	2 transponders
Total Mass (SS Amp)	kg	36.26	36.27	2 Amps, 2 Ant, 2 elec/transp

The required E_b/N_0 is taken from reference [39] assuming QPSK modulation and adding a 2 dB margin. The "K" factor, a function of the E_b/N_0, is taken from the TDRSS manual, which also gives the equation for ideal power received.

$$P_{rec\ id} = 10\log_{10}(\text{Data Rate}) - \text{"K"} \qquad \text{Eq. C-4}$$

The antenna pointing error is specified which gives the corresponding losses from:

$$L_\theta = -12\left(\frac{\theta_{err}}{\theta_{3dB}}\right)^2 \qquad \text{Eq. C-5}$$

The polarization (L_p), radio frequency interference (L_I), and non-compliance (L_{nc}) losses are all specified according to recommended values from the TDRSS guide. The predicted power received is then:

$$P_{rec\ pred} = P_{rec\ id} - L_\theta - L_p - L_I - L_{nc} \qquad \text{Eq. C-6}$$

The minimum and maximum ranges are computed from geometry with the minimum simply being the difference of geosynchronous altitude and the interferometer altitude, and the maximum being the straight-line distance tangent to the earth. The space loss (L_s) and required EIRP are computed as specified in the TDRSS guide.

$$L_s = -[32.45 + 20\log_{10}(\text{Range}) + 20\log_{10}(f_{MHz})]$$
$$EIRP_{req} = P_{rec\ pred} - L_s \qquad \text{Eq. C-7,8}$$

The link margin is set at 6 dB and the EIRP is simply the required EIRP plus the margin. The transmitter power is then computed from:

$$P_{tr} = EIRP - G_t - L_t \qquad \text{Eq. C-9}$$

The efficiency, input power, and mass for the solid state amplifiers are taken from reference [39]. The antenna mass is computed by assuming the phased array has twice the specific mass (15.9 kg/m^2) of a similarly sized parabolic dish with feed array. The remaining transponder electronics are for a standard NASA Ku-band component. The total mass shown assumes two antennas, two amplifiers, and two transponders.

Appendix D
Rocket Engine Data

Tables D-1, D-2, and D-3 show the data used in deciding among rocket engine options. All data is taken from reference [39]. Table D-1 shows the specifications for a variety of solid rocket motors. Their designation, propellant weight, and I_{sp} are all given. The delta v provided by each engine is computed from equation 3-33 assuming a spacecraft mass of 12,000 kg. Sine a circularization delta v with 10% margin of 176 m/s is desired, the STAR 37F appears to be the best choice.

Table D-1 Solid Rocket Motor Specifications

SRM Designation	Loaded Weight (kg)	Prop. Fract.	Prop. Weight (kg)	Isp (sec)	Delta V (m/s)
IUS SRM-1	10374	0.94	9751.56	295.5	1668.94
LEASAT PKM	3658	0.91	3328.78	285.4	673.79
STAR 48A	2559	0.95	2431.05	283.9	512.49
STAR 48B(S)	2135	0.95	2028.25	286.2	438.06
STAR 48B(L)	2141	0.95	2033.95	292.2	448.40
STAR 75	8066	0.93	7501.38	288.0	1330.67
IUS SRM-2	2995	0.91	2725.45	303.8	602.06
STAR 13B	47	0.88	41.36	285.7	9.72
STAR 30BP	543	0.94	510.42	292.0	119.93
STAR 30C	626	0.95	594.7	284.6	135.75
STAR 30E	667	0.94	626.98	290.1	145.59
STAR 37F	829	0.94	778.9	290.5	179.88
STAR 37FM	1149	0.94	1080.06	291.0	246.54

Tables D-2 and D-3 show data on liquid rocket thrusters. The propellant, thrust, I_{sp}, and engine mass are all given in [39]. the propellant mass is computed from the rocket equation for an 12,00 kg spacecraft, and the total mass assumes a tank mass equal to 20% of the propellant. Table D-2 gives data for the all-liquid option, where the liquid rocket engines are required to provide the circularization burn, while Table D-3 shows the data for the hybrid solid/liquid option, in which the liquid rocket engines must only provide orbit correction and de-boost. The burn times are simply computed from the required delta v and the thrust. The Marquardt 400 N thruster is chosen as the best option.

Table D-3 Liquid Rocket Engine Specifications for Hybrid Option

Developer	Propellants	Thrust (N)	Isp (sec)	Number	Emass (kg)	Prop Mass (kg)	Total Mass (kg)	Inj. Error Burn Time (min)	Delta i Burn Time (min)	De-Boost Burn Time (min)
TRW	Mono H	0.22	210	2	0.4	1266.27	1519.92	2735.76	4153.76	81434.75
TRW	N2H4 Thermal	0.67	303	2	1.8	857.05	1030.26	868.98	1321.25	26272.69
OLIN/RCC	Mono H	2.22	222.5	2	0.4	1189.91	1428.29	269.45	409.22	8043.62
TRW	Mono H	4.45	220	2	0.4	1204.45	1445.74	134.58	204.38	4015.29
TRW	Mono H	18	225	2	0.6	1175.72	1411.47	33.20	50.42	991.46
TRW	Mono H	36	227.5	2	0.6	1161.85	1394.82	16.58	25.18	495.43
HAM STD	Mono H	67	227.5	2	1	1161.89	1395.27	8.91	13.53	266.21
OLIN/RCC	Mono H	111	227.5	2	3.2	1162.12	1397.74	5.38	8.17	160.72
HAM STD	Mono H	133	233.5	2	2.8	1130.16	1358.99	4.48	6.80	133.94
OLIN/RCC	Mono H	222	232.5	2	3.6	1135.44	1366.13	2.68	4.08	80.27
HAM STD	Mono H	689	235	2	4.6	1122.57	1351.69	0.86	1.31	25.85
Walter Kidde	Mono H	1335	235	2	22.6	1124.47	1371.97	0.45	0.68	13.36
OLIN/RCC	Mono H	2669	232.5	2	16.4	1136.73	1380.48	0.22	0.34	6.68
MBB	N2O4/MMH	11	285	2	1	914.17	1098.00	53.18	80.83	1604.13
Marquardt	N2O4/MMH	22	290	2	1.4	897.50	1078.40	26.55	40.37	801.51
Aerojet	N2O4/MMH	67	295	2	2	881.52	1059.82	8.71	13.24	263.01
Marquardt	N2O4/MMH	111	300	2	2.8	866.10	1042.12	5.25	7.98	158.66
ARC/LPG	N2O4/MMH	489	308	2	8.2	842.81	1019.57	1.19	1.81	36.00
MBB	N2O4/MMH	400	305	2	9	851.62	1030.94	1.46	2.21	44.02
TRW	N2O4/MMH	445	301	2	9	863.59	1045.31	1.31	1.99	39.59
Marquardt	N2O4/MMH	400	309	2	7.6	839.93	1015.52	1.45	2.21	44.00
TRW	N2O4/N4H4	445	314	2	9	825.96	1000.15	1.31	1.99	39.53

Table D-2 Liquid Rocket Engine Specifications for All-Liquid Option

Developer	Propellants	Thrust (N)	Isp (sec)	Number	Emass (kg)	Prop Mass (kg)	Total Mass (kg)	Circularize Burn Time (min)	Inj. Error Burn Time (min)	Delta i Burn Time (min)	De-Boost Burn Time (min)
TRW	Mono H	0.22	210	2	0.4	2436.01	2923.61	75763.33	2774.18	4215.19	81777.38
TRW	N2H4 Thermal	0.67	303	2	1.8	1614.73	1939.47	23896.60	876.07	1332.77	26326.93
OLIN/RCC	Mono H	2.22	222.5	2	0.4	2280.21	2736.66	7451.76	272.92	414.77	8073.80
TRW	Mono H	4.45	220	2	0.4	2309.79	2772.14	3722.84	136.34	207.20	4030.70
TRW	Mono H	18	225	2	0.6	2251.40	2702.28	917.78	33.61	51.09	995.10
TRW	Mono H	36	227.5	2	0.6	2223.42	2668.71	458.27	16.79	25.51	497.21
HAM STD	Mono H	67	227.5	2	1	2223.50	2669.20	246.24	9.02	13.71	267.17
OLIN/RCC	Mono H	111	227.5	2	3.2	2223.93	2671.91	148.66	5.45	8.28	161.30
HAM STD	Mono H	133	233.5	2	2.8	2159.17	2593.81	123.68	4.53	6.89	134.40
OLIN/RCC	Mono H	222	232.5	2	3.6	2169.82	2607.38	74.14	2.72	4.13	80.55
HAM STD	Mono H	689	235	2	4.6	2143.95	2577.34	23.86	0.87	1.33	25.94
Walter Kidde	Mono H	1335	235	2	22.6	2147.32	2599.39	12.33	0.45	0.69	13.41
OLIN/RCC	Mono H	2669	232.5	2	16.4	2172.25	2623.10	6.17	0.23	0.34	6.71
MBB	N2O4/MMH	11	285	2	1	1727.34	2073.81	1463.64	53.65	81.60	1607.85
Marquardt	N2O4/MMH	22	290	2	1.4	1694.60	2034.92	730.65	26.78	40.74	803.31
Aerojet	N2O4/MMH	67	295	2	2	1663.08	1997.69	239.55	8.78	13.36	263.59
Marquardt	N2O4/MMH	111	300	2	2.8	1632.56	1961.87	144.38	5.29	8.05	158.99
ARC/LPG	N2O4/MMH	489	308	2	8.2	1586.81	1912.38	32.71	1.20	1.82	36.07
MBB	N2O4/MMH	400	305	2	9	1604.16	1933.99	40.03	1.47	2.23	44.11
TRW	N2O4/MMH	445	301	2	9	1627.51	1962.01	36.02	1.32	2.01	39.68
Marquardt	N2O4/MMH	400	309	2	7.6	1581.11	1904.93	39.98	1.47	2.23	44.08
TRW	N2O4/N4H4	445	314	2	9	1553.79	1873.54	35.89	1.32	2.00	39.60